Electronic and Optical Properties of Novel Carbon Structures

by

Manyalibo Joseph Matthews

B.S., University of California at Davis (1993)

Submitted to the Department of Physics
in partial fulfillment of the requirements for the degree of

Doctor of Philosophy in Physics

at the

MASSACHUSETTS INSTITUTE OF TECHNOLOGY

May 1998

Author .....
Department of Physics
May 1, 1998

Certified by .....
Mildred S. Dresselhaus
Institute Professor
Thesis Supervisor

Accepted by .....
Thomas J. Greytak
Associate Department Head for Education

Electronic and Optical Properties of Novel Carbon Structures

by

Manyalibo Joseph Matthews

Submitted to the Department of Physics
on May 1, 1998, in partial fulfillment of the
requirements for the degree of
Doctor of Philosophy in Physics

Abstract

Novel carbon structures in the form of fullerenes and disordered carbon clusters offer a wide variety of physical systems, possessing both long or short range order, which can generally be tuned through non-combustive heat-treatment at various elevated temperatures, T_{HT}. Due to the sheer complexity and diversity of the possible nanoscale arrangements, the optical and electronic properties of carbon structures with finite dimensions and crystallinity are still not fully understood. In this study, we focus mainly on the structures produced from carbonization of the hydrocarbon polymer polyparaphenylene (PPP), but we also present experimental results from carbons based on other precursors (e.g. mesophase pitch) which yield quite different structures with both comparable and contrasting physical properties.

In terms of electronic properties, we show that in the low-T_{HT} PPP-based structures, which exemplify extreme disorder, the electronic states are strongly localized, giving rise to a Mott $T^{1/4}$ hopping conductivity and self-trapped spin defects as evidenced by low-temperature transport and electron spin resonance experiments. Electronic transitions which give rise to ~2-3 eV photoluminescent emissions in PPP-based structures are found to be influenced most strongly by residual semi-localized polymeric states which weakly couple to low-frequency PPP phonon modes. However, at intermediate heat-treatment temperatures (T_{HT} ~1500-2500°C), all sp^2-bonded carbon compounds in this study exhibit a characteristic phonon spectrum (as evidenced by Raman spectroscopy) in which disorder may be characterized by non-zone-center phonon scattering arising from finite crystallite sizes. Because of its intimate connection to carrier confinement and structural disorder, the anomalous "disorder-induced" graphite D-band is thoroughly investigated by use of Raman spectroscopy, showing that strong dispersion effects are due to a photon-phonon coupling mediated by electronic transitions. Raman spectroscopy is also used with magnetic susceptibility measurements to show that the large diamagnetism of graphitic crystallites in the higher T_{HT} systems is strongly influenced by the confinement of quasi-two dimensional π-electrons within crystallites. For higher amounts of disorder *within* carbon crystallites, magnetoresistance measurements show that in-plane elastic scattering

centers give rise to quantum coherent backscattering (i.e. "weak localization") in certain intermediate T_{HT} carbon fibers. Along with presenting the optical and electronic properties of these carbon structures, we also discuss, for comparison, analogous low-dimensional structures based on metal (W, Mo) dichalcogenides and silicon clathrates (Si_{46}).

Thesis Supervisor: Mildred S. Dresselhaus
Title: Institute Professor

Acknowledgments

I will start by deeply thanking my thesis supervisor, Professor Mildred S. Dresselhaus. Words can not fully describe the respect and admiration I have for Millie, but I think most of the people who know me understand how I feel. I must also thank my co-supervisor, Dr. Gene Dresselhaus, for lively discussions about solid state theory (and superior command of LaTex!). I am sincerely thankful to the other members of my thesis committee, Professors Tomas Arias and Toyoichi Tanaka, as well as my academic advisor Professor Daniel Kleppner.

Among the graduate students in the Dresselhaus group (MGM), I've shared many friendships, which I hope continue to grow. Among the old crew, I thank Drs. Alex W. P. Fung and Gillian A. M. Reynolds for their early guidance in my research projects. Drs. James Chen and Jordina Vidal were both a pleasure to know. My wits were always sharpened through my interactions with Dr. Lyndon Hicks (as well as my knowledge of the latest MGM gossip). Dr. Siegfried Fleischer and Boris Pevzner always kept my MIT cynicism healthy and alive, and are both very talented engineers. Dr. Nathan Belk was also great to know as an extremely skilled experimentalist.

Of my contemporaries, I would like to sincerely thank my "carbon-coworker" Ms. Sandra D. M. Brown for, well, everything. I consider myself both lucky and proud to have been befriended by her. Another student in the group who I have considered a good friend is Mr. Xiangzhong Sun. His wittiness and cool demeanor has always impressed me, along with his sharp physics and computer skills. Mr. Joe Habib and I fought through the struggles of the General Examinations together, and share many similar tastes outside of physics. Of the newer members of MGM, Dr. Alessandra Marucci has been a delightful collaborator. Professor Marcos Pimenta, who shares the same flare for jazz music that I do, has been a wonderful person to work with. To all the other MGMers (Steve, Taka, Huiming, Hao, Herb, Zhibo and Marcie), it has been great to know you all.

Our administrative secretary, Mrs. Laura Doughty, has always helped to keep everybody sane through her hard work and organizational skills. Mrs. Peggy Berkovitz

(who I can not thank enough) has been, and will continue to be, the friend of the MIT physics graduate student through her kind consoling and influential position within the department. I would also like to thank all those in the physics department and physics headquarters (Professors Koster, Moniz and Friedman, Pat Solakoff and Liz Cooper) who helped or supported me personally, and were also essential to the success of the 1997 National Conference of Black Physics Students.

During my graduate career, I have had the fortunate opportunity to visit many other labs and collaborate with many talented researchers. Professor Morinobu Endo (Shinshu University) has been a long-standing colleague and collaborator of MGM, and I am honored to know him. Professors Toshiaki Enoki (Tokyo Inst. of Tech.), Seiichi Tanuma (Iwaki Meisei University) and Reshef Tenne (The Weizmann Institute) have all been an asset to know and work with on various projects. It has been especially fulfilling to collaborate with Mrs. Gitti Frey (The Weizmann Institute) both in person and through many emails and faxes. At MIT, my optical experiments would have never gotten off the ground were it not for the concerned collaboration of Dr. Don Heiman of the Francis Bitter Magnet Laboratory.

As a Black Physicist, I have greatly appreciated having graduate students of similar backgrounds here in the department. Marta, Jermane, Kimani, Grum, Tica, Victor, Tehani, Alison, Isaac, and Lyndie have all been great comrades. I have been so very fortunate to have formed lasting friendships outside MIT as well, and I am forever thankful to Ms. Jennell Mimms for her unconditional support. Dr. Danielle Elliott has been a dear companion who has stood by me throughout the battle of the thesis. To the BENT brotherhood (you know who you are) and the other brothers of AΦA around Boston: Phil, Mayo, Rasheed, Mike, Marcus W., Gerard, Pascal, Donald, Marcus M., Mark and Harold... much love. To my sands (and best friend) Bro. Wayne P. Sylvester, my special Bro. Jason E. Walker, my Yay Area partner Bro. Kenneth E. Lundy, Jr. and all of ΘH: I couldn't have done it without y'all.

Most of all, I thank God everyday for my family and their support: Mom, Pops, Susanna, Demitrius Hans del Montico, Tana, The Manloves, The Matthews' and The Kizarts. This degree and the work performed therein is, and has been, for you.

Contents

List of Figures

List of Tables

Chapter 1

Introduction

The physics and chemistry of carbon materials has been a area of science well-endowed with countless books[36, 38, 133], review articles[150, 171] and such, describing the physical properties of most carbon-based compounds. Graphite, as a single crystal, has provided physicists with an ample playground to study topics from quasi-two dimensional transport mechanisms in semi-metals[62, 126, 183], to phase transitions of intercalated species in graphite intercalation compounds (GICs)[35, 142]. Furthermore, the unique electronic band structure of two[117] and three[118] dimensional graphite near the intrinsic Fermi level gives rise to interesting electronic and magnetic properties[62, 159] such as an unusually large Landau diamagnetic moment[117]. The large anisotropy observed in graphite[60, 89] is ultimately due to the quantum hybridization of s and p orbitals into planar sp^2 σ-bonds, leaving the remaining p_z orbital delocalized out-of-plane in the form of π bonds[140].

However, since the discovery of C_{60} Buckyballs in 1985[90], and the subsequent discovery of carbon nanotubes in 1991[73], the electronic structure of graphitic structures has been revisited with the emphasis on nanostructures and quantum confinement. Indeed, much has been learned in recent years regarding the novel electronic and optical properties of these carbon nanostructures, which in many ways contrast that of the bulk due to modifications of symmetry and dimensionality. Nonetheless, the local bonding arrangement in all these structures, including graphite, is still that of π- and σ-bonds with a basic sp^2 configuration which results in similarities in the phonon and

electron dispersion relations among many of these carbon-based materials.

Interestingly, little is known about how these exciting new structures are formed in the first place. Various models have been proposed on this subject, most of which describe the aggregation of small carbon clusters at high temperatures. The problem of carbon nanostructure formation essentially boils down to the complex physics and chemistry of molecular arrangement and rearrangement at elevated temperatures. The arrangement of carbon clusters to form sp^2 semi-extended structures is also a main problem in the understanding of the carbonization of various hydrocarbon precursors used to form disordered or (with higher heat treatment temperature T_{HT}) ordered sp^2 structures. The physics of carbonization is not well understood in general, primarily due to the complexity of non-equilibrium ion and electron dynamics. When the heat-treatment temperature (T_{HT}) is low ($\leq$ 1000° C), small graphene clusters form, whose dimensions are on the order of C_{60} and carbon nanotube dimensions ($\sim$ 10-50 Å in diameter). At higher T_{HT} (1000-2300° C), larger graphene ribbons tend to loosely stack to form a "turbostratic" structure such that the orientation of a given graphene layer is uncorrelated with that of its neighbor, giving rise to 2D electron dynamics. At the highest T_{HT} ($\geq$ 2300° C), the 3D "ABAB" ordering of graphene layers yields the $P6_3/mmc$ graphite structure (or in some cases, a rhombohedral structure is formed with $R\bar{3}m$ symmetry[188]). Thus, heat-treatment allows one to study the confined and disordered graphite lattice at various stages of its development.

It is the goal of this work to study in some detail the properties of disordered or "pregraphitic" carbons produced from a variety of sources. Since the creation and structural rearrangement of σ and π bonds in the initial carbonization stage is essentially the starting point of the formation of carbon nanostructures, I will pay special attention to the carbonization of a model polymer precursor, polyparaphenylene (PPP). An ulterior motive of this focus is to understand the chemistry and physics of PPP heat-treated at the specific temperature of 700° C, since this material has been shown to have the ability to electrochemically accept more lithium per carbon than conventional graphite intercalation compounds (GICs). Hence, this material is an attractive candidate for hosting lithium ions in novel Li-ion or "Rock-

ing chair" secondary battery cells. It will be shown that the structures formed from PPP near T_{HT}=700°C exhibit polymeric structures that resemble the polymer precursor; therefore, a reasonable treatment of the electronic and optical properties of polyparaphenylene will be in order. We thus include study of the dynamics of defect centers in PPP (i.e., polarons) in order to understand the optical and electronic properties of these low-T_{HT} materials in which polymeric and carbonized domains are restricted to nano- and meso- length scales. At higher T_{HT}, where carbonization (i.e. complete thermal removal of non-carbon species) has thoroughly occurred, PPP-based carbon exhibits physical properties similar to most carbons, and thus I will extend discussion to include other materials, namely mesophase pitch-based carbon fibers (MPCFs) and activated pitch-based carbon fibers (ACFs). It will be shown that these materials possess moderate-range order ($\sim$ 100 Å size crystallites) which is reflected in the magnetic properties of the delocalized π electrons. The LUMO levels of these small aromatic-like clusters form localization centers for 3D hopping transport, which evolves to 2D hopping as carriers are confined within graphite layers at higher T_{HT}. Furthermore, we find it convenient to characterize the amount of in-plane disorder by the relative strength of the disorder-induced, or "D" Raman band, as has traditionally been done in carbon/graphite systems[80].

Along with the aforementioned carbon samples, I will also present, for comparison, the optical spectra of inorganic fullerene-like MoS_2/WS_2 nanostructures, as well as the novel silicon clathrate compound, Si_{46}. It will be shown that, for the case of the metal dichalcogenides, disorder brings about modifications in the Raman spectra that can be related to similar effects in graphite.

I thus present this work as follows. Chapter 2 details the synthesis procedure and elementary characterization for all materials studied. Chapter 3 then describes light scattering in disordered carbon and metallic clathrate compounds, as studied by Raman and photoluminescence (PL) spectroscopies. PL turns out to be a powerful tool in understanding the electronic and vibronic structure of the defective polymer samples, while Raman scattering is used to study samples at various heat-treatment-temperatures, since this technique is particularly sensitive to the local order. Another

technique sensitive to local environment is electron spin resonance (ESR) and the results of ESR studies are presented in Chapter 4. The results of ESR can then be compared with Raman scattering and electronic transport measurements of PPP-based carbons, which is presented in Chapter 5. Chapter 6 gives a thorough investigation of both localized and extended state electrons which produce Curie and Landau magnetism, respectively, in carbon-based systems. In particular, I will connect magnetic susceptibility data to both ESR and Raman measurements in order to more fully detail the effect of disorder at the various T_{HT} values studied. The electronic structure of PPP-based carbons was investigated using state-of-the-art *ab initio* pseudopotential calculations based on conjugate gradient techniques, which allowed me to model defects in disordered PPP. Since most of the carbons used in this study originated from samples used in actual Li-ion rechargeable cells, I dedicate chapter 8 to the physics and chemistry of Li-doped carbon anodes, and in this chapter I attempt to connect the findings of my optical and electronic experiments (on undoped and doped disordered carbons) to the performance of these cells. Finally, I give the conclusion of my work in Chapter 9, where I summarize the effects of disorder, in the form of confinement and in-plane defects, on sp^2-bonded carbon structures. Fundamentally, this study offers the opportunity to study the interaction of localized states brought about by disorder and extended states formed through progressive heat-treatments.

Because of the wide variety of samples studied and techniques used, I worked with many collaborators who were also interested in the effect of disorder in layered systems. Namely, Professor Morinobu Endo of Shinshu University in Japan contributed the entirety of carbon samples used in this study. Another colleague in Japan, Professor Toshiaki Enoki of the Tokyo Institute of Technology, collaborated with the ESR measurements and provided useful advice regarding this delicate technique. Professor Reshef Tenne and Mrs. Gitti Frey provided the samples of metal dichalcogenides, which were used in the optical studies. At the Francis Bitter Magnet Laboratory at MIT, Dr. Don Heimann provided the invaluable service of his optical setup, while Drs. Gene Dresselhaus and Joey Wang provided very useful discussions. The *ab initio* calculations were performed in collaboration with Professor Tomas Arias of the MIT

Condensed Matter Theory group. These collaborators essentially made possible the completion of this work through their very meaningful collaboration.

Chapter 2

Materials Synthesis and Characterization

2.1 Polyparaphenylene (PPP)

2.1.1 Preparation and Chemistry of PPP-based Carbons

The PPP used in the present experiments was provided by Prof. M. Endo of Shinshu University and was synthesized by the Kovacic method[85] (see Fig. 2-1) using a reaction vessel maintained at 30°C, yielding PPP in granular form. Samples of this material were subsequently heat treated to various temperatures T_{HT} between 600 and 3000°C in high purity argon gas, using a conventional resistance furnace for T_{HT} values $<$ 1000°C and a graphite resistance furnace for $T_{HT} >$ 1000°C. Samples are hereafter referred to by their acronym "PPP-" followed by the heat-treatment temperature to which they were subjected. For example, PPP-1000 refers to PPP heat-treated to 1000°C. A residence time of 1 hour was used for the heat treatment. Subsequent to preparation and heat treatment, the samples were characterized by X-ray diffraction (XRD) as shown in Fig. 2-4. A summary of the characterization is given in [115].

As a function of T_{HT}, PPP changes more gradually to a graphitic material than is common for so-called graphitizing materials[171], as is shown in Fig. 2-2, where

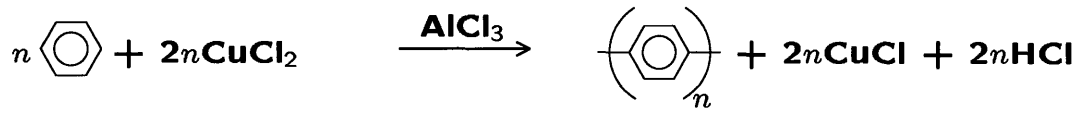

Figure 2-1: Chemical reaction for the formation of PPP (Polyparaphenylene) by the Kovacic method[85].

the carbon yield for PPP vs. T_{HT} is plotted. In this work, carbon yield is defined as the ratio of the weight of carbon produced through heat-treatment to the weight of the starting material (PPP). The results show a gradual decrease in the carbon yield with increasing T_{HT} as more hydrogen and hydrocarbon volatiles are vaporized from the sample over the range 600°C $< T_{HT} <$ 2000°C. This loss of hydrogen is also shown in Fig. 2-3 where the H/C atomic ratio is plotted as a function of T_{HT}. The H, C, and N content of the heat-treated PPP samples was evaluated by the combustive elemental analysis of Oneida Research Services, Inc. Note the drastic decrease in H/C which occurs above 700°C. For T_{HT} above 700°C, the data show the superior carbon yield behavior of PPP in contrast to a furfurol alcohol-based carbon, a typical non-graphitizing (glassy) carbon, which shows a very rapid decrease in carbon yield with increasing T_{HT} as well as a lower value of the carbon yield at stabilization. As T_{HT} increases above 2400°C, the carbon yield for PPP stabilizes at ~70%. For characterization purposes, PPP with a T_{HT} of 600°C has a dark bronze color, which changes to black for $T_{HT} \geq$ 700°C. Figure 2-2 shows that PPP-based carbon can thus be characterized as one of the high yield carbons[36].

2.1.2 Structural Characterization

Figure 2-4 shows the (002) X-ray diffraction (XRD) peaks for PPP-based samples heat treated at various temperatures. A silicon powder sample is used as an internal standard for calibration of the interlayer separation d_{002} and to determine the crystallite thickness L_c. The PPP-700 material shows a very broad (002) peak as seen in Fig. 2-4, indicating a highly disordered carbonaceous material, while PPP-2900 shows a sharp graphitic structure. Little change in the X-ray spectra is seen between the PPP-700, PPP-800 and PPP-1000 samples. However, major changes in

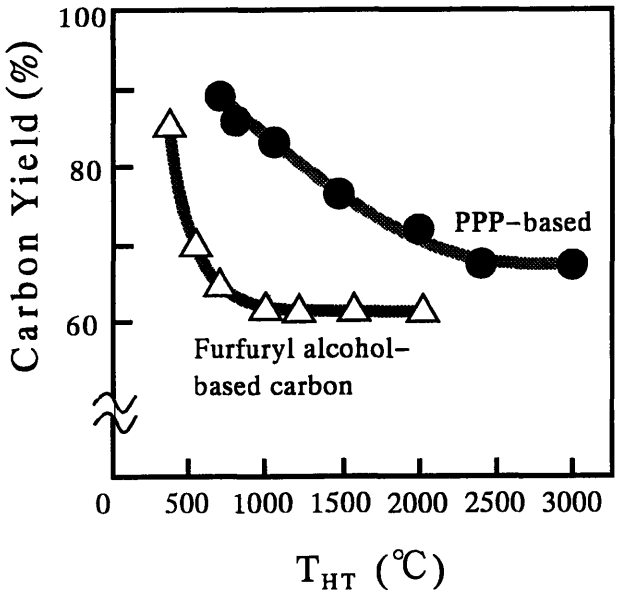

Figure 2-2: Carbon yield of PPP-based carbon in an argon atmosphere as a function of T_{HT}. Included for comparison is the carbon yield of furfuryl alcohol based carbon[115].

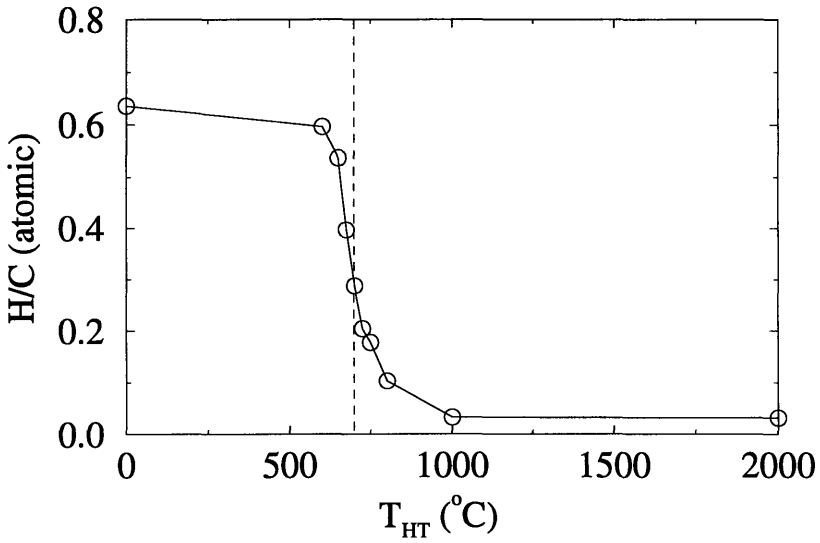

Figure 2-3: Ratio of atomic hydrogen (H) to atomic carbon (C) as determined by elemental analysis. The dashed line corresponds to $T_{HT} = 700°\mathrm{C}$.

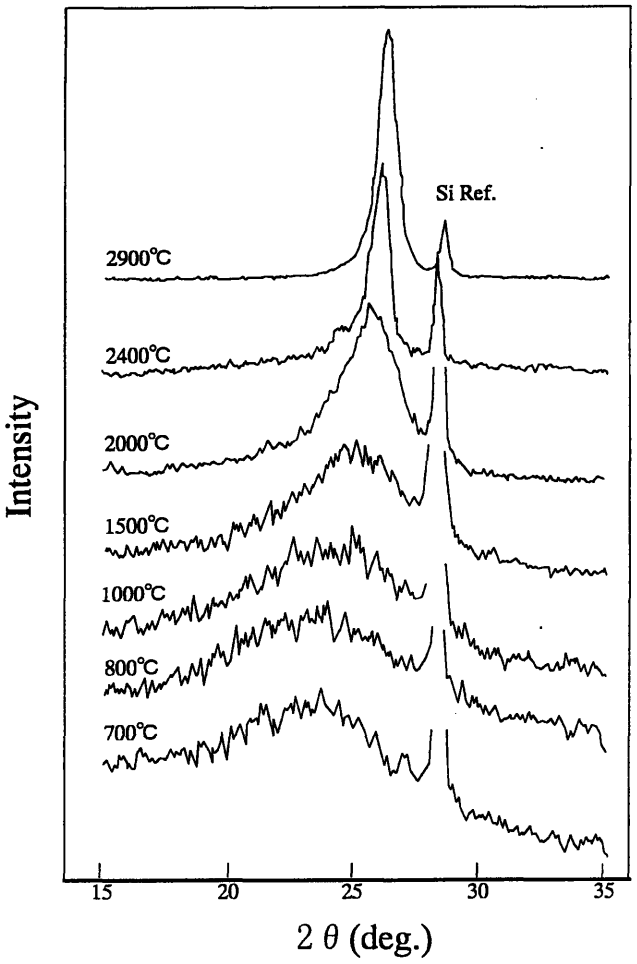

Figure 2-4: (002) X-ray diffraction profiles for PPP-based carbons heat treated at 700–2900°C. The Si (111) peak is used as an internal standard[115].

the peak resolution and line width are observed between the PPP-1000, PPP-1500, and PPP-2000 traces in Fig. 2-4. Finally, a sharp (002) feature appears for the PPP-2400 trace, and an even sharper (002) feature for the PPP-2900 trace. The intensity of the (112) peak, which appears at 83.6° in well-graphitized materials, is a measure of the 3D-stacking interlayer correlation length. Note that no (112) diffraction peak was observed for PPP-2900, which is an indication of the turbostratic nature of the material.

Figures 2-5(a) and (b), respectively, show the T_{HT} dependence of the interlayer separation distance d_{002} and the apparent c-axis crystallite size L_c, as determined by XRD measurements, indicating graphitizing behavior of PPP at high heat treatment

Table 2.1: Summary of PPP-based carbon structural properties.[a]

Sample	L_c (Å)	d_{002} (Å)	$\mathcal{G}$	I_D/I_G[b]	L_a (Å)
PPP-700	11	3.8	-.–	-.-	–
PPP-800	15	3.8	-.–	1.7	26
PPP-1000	20	3.65	-.–	1.7	26
PPP-1500	23	3.56	-.–	1.0	44
PPP-2000	42	3.44	0	0.65	68
PPP-2400	65	3.38	0.70	0.48	92
PPP-2900	90	3.37	0.81	0.36	122
VGCF-1050	46	3.44	0	0.90	49
VGCF-1900	300	3.36	0.93	0.35	126

[a] The Raman data were taken at a laser excitation energy of 2.54 eV.
[b] The ratio of Raman intensities of the D line to that for the G line is a measure of the degree of graphitization.

temperatures. The L_c values in Fig. 2-5 were determined from the half-width of the (002) diffraction line, taking into account Lorentz-polarization and the atomic scattering factor, and using the Si (111) peak as an internal standard. In Fig. 2-5, a comparison is also made between the graphitization of PPP-based carbon and vapor grown carbon fibers (VGCF's), which represent one of the typical graphitizing carbons. The interlayer d_{002} spacing of PPP-700 is estimated to be ~3.8 Å, which is a rather large value even for a turbostratic carbon, but d_{002} decreases progressively with increasing T_{HT}, reaching a value of 3.37 Å at T_{HT} = 2900°C, close to the graphite value of 3.35 Å for d_{002}.

It is clearly seen from the large change in d_{002} as a function of T_{HT} that PPP-based carbons are transformed from a highly disordered material at $T_{HT} \sim$ 700°C to a relatively well-graphitized carbon form for PPP-2900. On the other hand, the crystallite thickness L_c in Fig. 2-5(b) does not show such a large increase with T_{HT} as is normally found in graphitizing carbons. Rather, Fig. 2-5(b) shows increases in L_c from $\sim$ 10 Å at T_{HT} = 700°C to $\sim$ 90 Å at T_{HT} = 2900°C. Figure 2-5 further shows that L_c for vapor grown carbon fibers increases from ~50 Å for T_{HT} = 1050°C (as-prepared sample) to about 300 Å for T_{HT} = 1900°C, and to over 1000 Å for T_{HT} = 3000°C (not shown). The properties of PPP-based carbon samples are summarized in Table 2.1

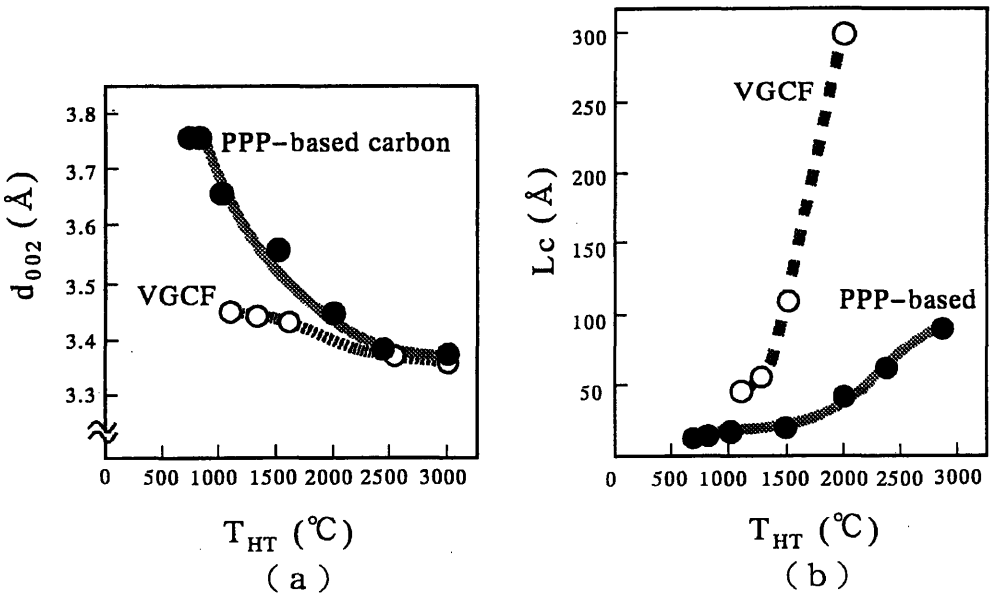

Figure 2-5: The interlayer separation distance d_{002} (a) and crystallite thickness L_c (b) vs. heat treatment temperature T_{HT}. The data for PPP are compared with corresponding data for vapor-grown carbon fibers (VGCFs)[115].

with the degree of graphitization $\mathcal{G}$ for $T_{HT} \geq 2000$°C given by

$$\mathcal{G} = \frac{3.44 - d_{002}}{3.44 - 3.354} \tag{2.1}$$

where $\mathcal{G} = 0$ corresponds to the turbostratic limit ($d_{002} = 3.44$ Å) and $\mathcal{G} = 1$ corresponds to a completely graphitized material ($d_{002} = 3.354$ Å). Thus, in PPP-based carbon, graphitization starts at a relatively high temperature, such as T_{HT}=2000°C, which is about 600°C higher than that for typical graphitizing carbons such as VGCF[36].

From a structural standpoint, the PPP-based carbon shows graphitizing behavior in some ways, but not in others. When the PPP-based carbon is characterized by the interlayer separation, it appears to be a graphitizing carbon, but with a crystallite thickness L_c that is restricted to small values characteristic of non-graphitizing carbons. The restriction to the growth of L_c arises from the molecular structure of the precursor PPP, which has a chain molecular configuration. As the crystallite develops, the chains stack several layers deep, but remain entangled with each other. Thus

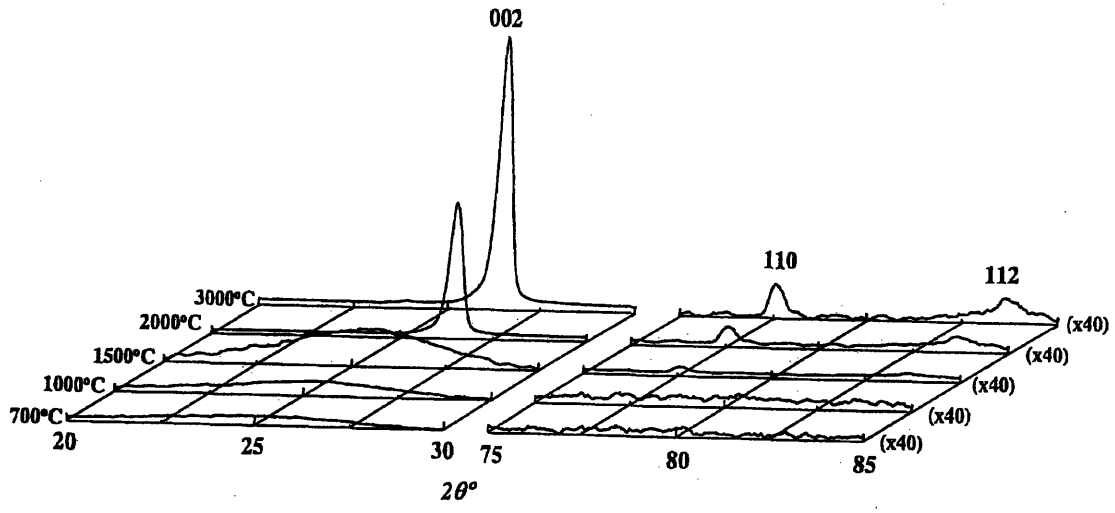

Figure 2-6: X-ray diffraction profiles for MPCF-based carbons heat treated at 700–3000°C[40].

the interlayer spacing of PPP develops as a graphitizing carbon, but the increase in L_c develops slowly, in a manner of non-graphitizing carbons.

2.2 Mesophase Pitch-based Carbon Fibers (MPCFs)

2.2.1 Sample Preparation

The MPCFs used in this study were milled in order to facilitate electrochemical experiments, since unmilled fibers do not easily form pressed pellets. The milled MPCFs were prepared using a melt-blow method for fiber synthesis[36]. Oxidation of the pitch precursor was performed in air at 300°C, following which the fibers were milled, and then weakly carbonized at 700°C. Graphitization was achieved through heat-treatment at 3000°C in an Ar atmosphere for 1 hr. Substitutionally boron-doped samples were also prepared by adding B_4C to the carbonized sample prior to the graphitization stage.[174]

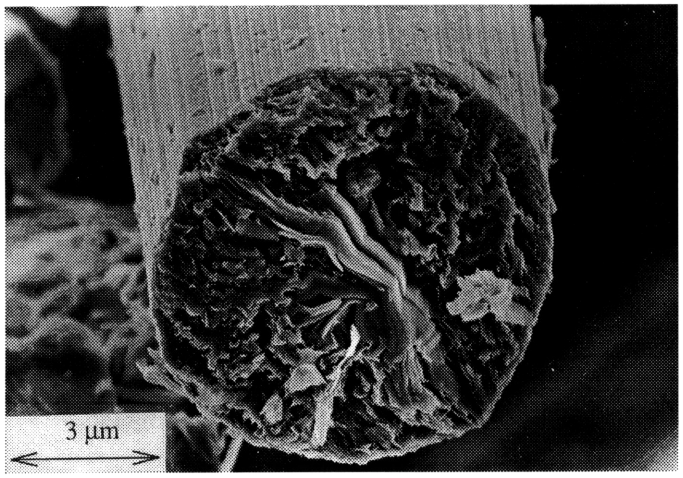

Figure 2-7: SEM micrograph of the cross section of a typical mesophase pitch-based carbon fiber (MPCF) heat-treated to 3000°C[40].

2.2.2 Structural Characterization

Characterization of MPCFs was performed by way of XRD and Scanning Electron Microscopy (SEM). XRD data for MPCFs are shown in Fig. 2-6 for T_{HT} at and above the carbonization temperature ($\sim$ 700°C), showing a well-defined (002) peak for samples heat treated above 2000°C. Also plotted in Fig. 2-6 are the weaker (110) and (112) reflections, showing an increase in in-plane ordering and ABAB stacking registry with increasing T_{HT}. In contrast to the PPP-based samples, the MPCF samples showed a graphitizing behavior with regard to d_{002}, crystallite size development, and 3D ordering with increasing T_{HT}. Figure 2-7 shows the SEM micrograph of the cross section of a typical milled fiber, showing a diameter on the order of 8 μm with lengths ranging from 50 to 100 μm. As shown in Fig. 2-7, a highly convoluted structure is observed, with a roughly layered ordering along the fiber axis.

2.3 Phenol-based Activated Carbon Fibers (ACFs)

2.3.1 Sample Preparation

Carbon fibers can also be made from other precursors such as isotropic pitch (ACP), phenol (FRL), polyacetate or polyacrylonitrile (PAN). The precursor used to produce

the activated carbon fibers (ACFs) in our studies was FRL. Through activation, a higher amount of disorder can be introduced in higher T_{HT} carbon samples. The first step in producing fibers is to spin the precursor materials to make fine whiskers. The pre-activated fibers are then heated in a reducing environment between 200 and 400° C. The fibers are then activated by introducing an activating agent such as carbon dioxide or water vapor in the temperature range of 1100 to 1400° C. This activation process helps both to remove impurities and greatly increases the porosity. Because of their specific application to filtration, the ACFs have also been characterized by their specific surface area (SSA), which is typically 1000-3000m^2/g and is measured using Brunauer-Emmett-Teller (BET) analysis of the adsorption isotherms of N_2 at 78K and CO_2 at 195K[58]. The samples are then heat treated at various temperatures, depending on the amount of graphitization desired. The two sets of samples (denoted by ACF-2000 and ACF-2500) studied here were heat treated at 2000 and 2500° C, respectively.

2.4 Fullerene-like Metal Dichalcogenides

2.4.1 General Properties

The novel synthesis of inorganic fullerene-like (IF) materials was performed by our collaborators at the Weizmann Institute, led by Professor R. Tenne and his graduate students G. Frey and M. Homyonfer, and has recently been described in the literature[47]. A starting precursor of MoO_3 powder is heated to temperatures above 800°C and reduced to MoO_{3-x} in a reducing atmosphere (N_2/H_2 5%). The suboxide sublimes and reacts with H_2S gas which converts the suboxide particle into the respective inorganic fullerene IF particle. The reaction product is collected in powder form on a quartz substrate. The IFs of metal dichalcogenides exhibit a variety of sizes and shapes and have been investigated by X-Ray powder diffraction (XRD)[48], scanning tunneling microscopy (STM)[68], high resolution transmission electron microscopy (TEM)[71] and optical absorption spectroscopy[53]. A typical TEM image of a 200 Å

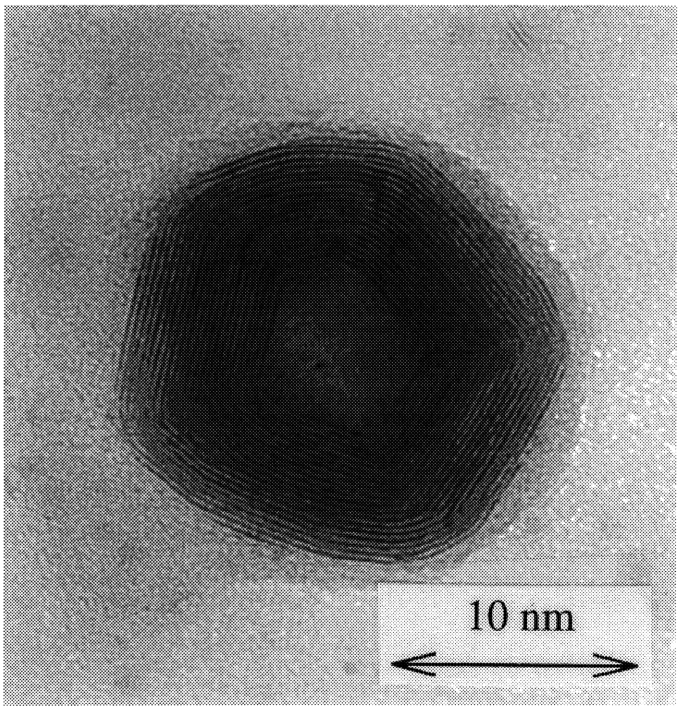

Figure 2-8: TEM micrograph of a typical IF nanoparticle roughly 200 Å in diameter[71].

IF nanoparticle is shown in Fig. 2-8. The XRD analysis revealed that the 2H structure of the unit cell is locally preserved within an IF particle. Nonetheless, a shift of the XRD (0002) peak of the IF phase indicates a lattice expansion of ca. 2% between two adjacent MoS_2 slabs along the c-axis compared to the bulk 2H polytype[47]. A systematic study of the optical properties[53] shows that the semiconductivity of the layered material is preserved in the IF structures. However, a decrease (red shift) in the band gap[68] and position of the excitons[53] of the IF compared to the 2H bulk is found. For IF-MoS_2 (value for 2H in parentheses) at room temperature, the A and B exciton energy values are 1.82 (1.88) eV and 1.95 (2.06) eV, respectively.

2.5 Silicon Clathrates

Silicon clathrate compounds (Na_xSi_{46}, Na_xSi_{136}) were synthesized at NEC laboratories (Tsukuba, Japan) under the direction of Dr. K. Tanigaki through a multistep process,

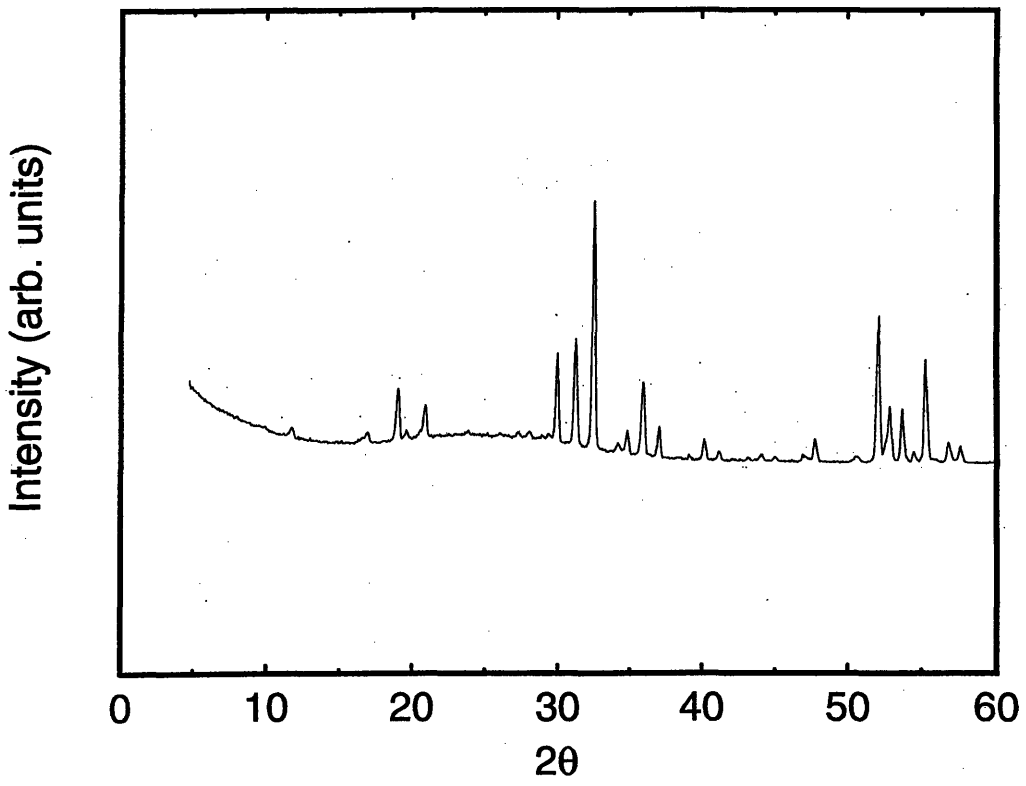

Figure 2-9: XRD plot of sodium silicon clathrate (Na_xSi_{46}).

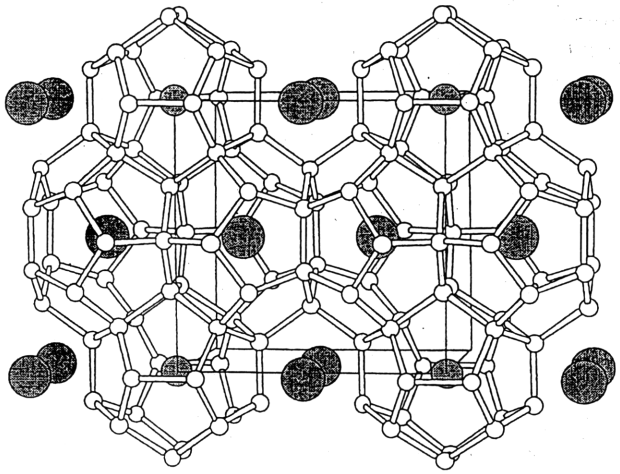

Figure 2-10: Schematic diagram of the silicon clathrate (Na_xSi_{46}) structure. The small white atoms shown are the Si atoms, while the larger dark atoms represent the two inequivalent sites that the Na occupy in the x=8 stoichiometry.

as shown in the reaction equations below:

$$Na + Si(powder) \xrightarrow{T_{HT,1},\, Ar} NaSi \tag{2.2}$$

$$NaSi \xrightarrow{T_{HT,2},\, vacuum} Na_xSi_{46}, Na_xSi_{136} \tag{2.3}$$

In general, both phases of silicon clathrate are formed from such a process, since the ratio of Si_{46}:Si_{136} is very sensitive to the heat-treatment temperature ($T_{HT,2}$) of the second synthesis step. However, careful control of $T_{HT,2}$ can produce samples almost completely composed of one phase or the other. First, sodium silicide was prepared by direct reaction of equal molar amounts of Na solid and Si powder in tantalum vessels which were placed in stainless steel tubes and sealed under Ar atmosphere at 650° C for 24 hours. The sodium silicide (NaSi) was then slowly heat treated at ~400°C for ~50 hours. The resulting Na_xSi_{46} crystal was then transferred to a capillary tube and sealed under Ar flow. The XRD spectrum is shown in Fig. 2-9. Note the absence of the Si single crystal peak at ~28°, indicating a pure clathrate sample. The interesting structure of the resulting Na_xSi_{46} (x=8) structure is shown in Fig. 2-10.

Chapter 3

Light Scattering and Electronic Transitions in Layered Compounds

3.1 Introduction

In this chapter the interaction of laser light with layered disordered materials is described. The effect of disorder can be carefully studied through the relaxation of the symmetry selection rules involved in light scattering. Moreover, a detailed analysis of the homogeneous broadening of Raman and photoluminescence spectra can give information on phonon and electronic lifetimes involved in the light scattering process. We begin by summarizing the theory of light scattering in section 3.2 under the usual assumption that the electronic and ionic motions can be decoupled under the so-called *Born – Oppenheimer Approximation*. This then leads to several simplifications to the theory of Raman and photoluminescent emission lineshapes which allow us to quantitatively study the effect of disorder in both the carbon and MoS_2 layered systems.

Following the theoretical background of section 3.2, experimental details are given in section 3.3. The results of Raman experiments on carbon-based (PPP, MPCF) and MoS_2-based samples are presented in section 3.4, while the PL results for PPP-based carbons are presented in section 3.5 and connected to the Raman spectra found in the previous section.

3.2 Theory of Light Scattering in Electron-Lattice Coupled Systems

3.2.1 The Born-Oppenheimer Approximation

We start by considering the Hamiltonian which describes the spin-independent electron-lattice system, which can be given by[106]

$$H = H_{el} + H_{ion} + H_{el-ion} \tag{3.1}$$

where

$$H_{el} = -\sum_{k} \frac{\hbar^2}{2m}\nabla_k^2 + \frac{1}{2}\sum_{k,k'}{}' \frac{e^2}{|\mathbf{r_k} - \mathbf{r'_k}|} \tag{3.2}$$

$$H_{ion} = -\sum_{i} \frac{\hbar^2}{2M_i}\nabla_i^2 + \frac{1}{2}\sum_{i,i'}{}' V_{ion}(\mathbf{R_i} - \mathbf{R'_i}) \tag{3.3}$$

$$H_{el-ion} = \sum_{k,i} V_{el-ion}(\mathbf{r_k} - \mathbf{R_i}). \tag{3.4}$$

In the above equations, e is the electronic charge, m is the electron mass, M_i are the masses of the ions, and the no-double counting-restricted($'$) sums are over electron (i) and ion (k) indices; $\mathbf{r_k}$ and $\mathbf{R_i}$ are then the electronic and ionic spatial coordinates. In a dynamic lattice, the difficulty in solving Schroedinger's equation, $H\Psi = E\Psi$, lies primarily in the crystal field term, H_{el-ion}. Born and Oppenheimer developed a method to deal with this problem in which the dynamics of the electronic and ionic subsystems could be decoupled (the so-called *Adiabatic* approximation). As a first approximation, however, we first consider the motion of the electrons in the static lattice:

$$(H_{el} + H_{el-ion})\psi(\{\mathbf{r_k}, \mathbf{R_i}\}) = E_{el}(\{\mathbf{R_i}\})\psi(\{\mathbf{r_k}, \mathbf{R_i}\}). \tag{3.5}$$

In the above Schroedinger equation, $\psi(\{\mathbf{r_k}, \mathbf{R_i}\})$ and $E_{el}(\{\mathbf{R_i}\})$ are the eigenfunction and eigenenergy of the electronic Hamiltonian as a function of all electronic and ionic positions. It is then assumed that the total solution of the combined electron-lattice problem can be written as $\Psi(\{\mathbf{r_k}, \mathbf{R_i}\}) = \psi(\{\mathbf{r_k}, \mathbf{R_i}\})\phi(\{\mathbf{R_i}\})$ which then gives for

the complete Schroedinger equation

$$H\Psi = (H_{el} + H_{ion} + H_{el-ion})\psi\phi \tag{3.6}$$

$$= \psi(H_{ion} + E_{el})\phi - \sum_i \frac{\hbar^2}{2M_i}(\phi\nabla_i^2\psi + 2\nabla_i\phi \cdot \nabla_i\psi). \tag{3.7}$$

The key insight into approximating the above electron-lattice coupled equation is to note that the motions of the electrons are much faster than that of the ions, so that the last two terms involving ionic spatial derivatives end up being quite small. Omission of these terms essentially amounts to decoupling the electron and ion motion so that the total energy of the system, E, can be given by

$$(H_{ion} + E_{el})\phi(\{\mathbf{R_i}\}) = E\phi(\{\mathbf{R_i}\}). \tag{3.8}$$

The above equation describes the *ionic* eigenfunctions, and can be explicitly written as

$$\left[\sum_i \frac{\hbar^2}{2M_i}\nabla_i^2 + \frac{1}{2}\sum_{ii'}{}' V_{ion}(\mathbf{q_i} - \mathbf{q_i'})\right]\phi(\{\mathbf{q_i}\}) = (E - E_{el})\phi(\{\mathbf{q_i}\}) \tag{3.9}$$

where $\mathbf{q_i} = \mathbf{R_i} - \mathbf{R_i^0}$ are the ionic displacements from the equilibrium positions. A crude approximation to the eigenstates of the electrons could be found by using some mean value of $\mathbf{R_i}$ in the H_{el-ion} term in Eq. 3.5 (this is the so-called Condon approximation). The solution to the above coupled dynamic lattice equation is easily solved using a harmonic oscillator approximation and describing the motion of the ions in terms of normal modes, Q_j, where the ionic eigenstates are now products of harmonic oscillator functions:

$$|\phi\{(Q_j)\}\rangle = \prod_j^{3N-6} |n_j\rangle \tag{3.10}$$

with average eigenenergies given by

$$E - E_{el} = \sum_j \hbar\omega_j(\langle n_j\rangle + \frac{1}{2}), \tag{3.11}$$

where ω_j is the angular frequency of the jth (phonon) mode which has an average occupation number, $\langle n_j \rangle$ given by Bose-Einstein statistics.

In order to examine the dynamical changes to the Born-Oppenheimer states, $\psi(\{\mathbf{r_k}, \mathbf{R_i}\})\phi(\{\mathbf{R_i}\})$, in the presence of a radiation field, we must first deal with the problem of how to consider all normal modes of the system. Furthermore, the ω_j's do not have to be constant, but could depend on the electronic state as well as the mode under consideration. We deal with these issues in the next section.

3.2.2 The Configurational Coordinate Model

Following the work of Krushinskii and Shorygin[91, 92], we assume that the harmonic potential describes the inter-ionic potential energy sufficiently well, and we further assume that one mode, of the total number of possible modes, can adequately represent the vibronic levels of our system. This is a reasonable assumption for the case of PPP, since the modes which are expected to be strongly coupled to electronic transitions are less than 100 cm^{-1} apart (see section 3.6), while typical features in the PL spectra of PPP are much broader (1000-2000 cm^{-1})[97]. Figure 3-1 shows the configurational coordinate diagram for an electronic transition involving one representative phonon mode. When the electron-lattice system absorbs a photon, the electronic energy is raised. However, the equilibrium position of the harmonic potential need not (and typically is not) the same in both ground and excited states. Using a one-dimensional approximation[67], we denote this difference in equilibrium normal coordinate positions between the ground and excited states as:

$$\Delta Q_{eg} = Q_0^{(ex)} - Q_0^{(g)} \tag{3.12}$$

where the superscripts refer to the excited (ex) and ground (g) electronic states. For the time being, we will assume that the representative vibrational frequencies of the ground and excited states are equal and are simply given by ω, but this restriction can be lifted with minor modifications.

In terms of normal modes, the ground and excited state energies, $E^{(g)}$ and $E^{(ex)}$

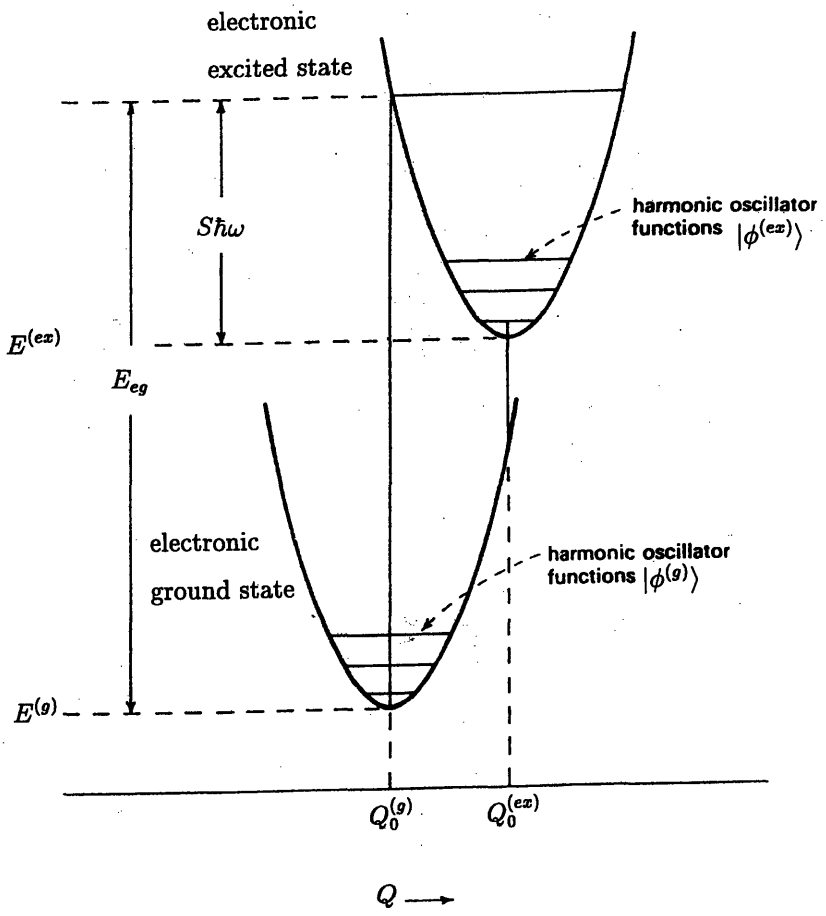

Figure 3-1: Configurational coordinate model for electron-lattice coupled transitions. The Huang-Rhys parameter, S, is a measure of the normal coordinate equilibrium position shift upon electronic excitation from the ground state $E^{(g)}$ to an excited state $E^{(ex)}$. The electronic states are separated by an energy gap, E_0, while the energy separation of a typical vibronic level in the conduction band and the zero phonon level in the valence band is E_{eg}.

respectively, are given by (see diagram in Fig. 3.1):

$$E^{(g)} = \frac{1}{2}\mu\omega^2(Q - Q_0^{(g)})^2 \tag{3.13}$$

$$E^{(ex)} = E_{eg} + \frac{1}{2}\mu\omega^2(Q - Q_0^{(g)})^2 - (\Delta Q_{eg})(Q - Q_0^{(g)}) \tag{3.14}$$

where μ is some effective mass of the ionic system, and E_{eg} is defined in Fig. 3.1. We explicitly assume here that the ground and excited state normal coordinate basis sets are identical, although generally, a rotation or some sort of mixing of normal coordinates[66, 185] can occur (the Duschinsky effect) complicating the analysis considerably. In order to retain physical insight to the problem, we will ignore the Duschinsky effect in this work. The equation for $E^{(ex)}$ has been expressed in terms of the ground state coordinates and the energy E_{eg}. By writing the excited state energy as in Eq. 3.14, we can easily see that the difference in energies is *linear* in normal coordinate displacement, modulated by the factor ΔQ_{eg}. Hence ΔQ_{eg} describes the relative amount by which the electron-lattice (or electron-phonon) coupling changes as the system goes from the ground state to excited states. It is usual, however, to describe this change in electron-phonon coupling by the dimensionless factor,

$$S = \frac{\mu\omega^2}{2\hbar\omega}\Delta Q_{eg}^2 \tag{3.15}$$

known as the Huang-Rhys parameter, where S essentially characterizes the relative magnitude of the electron-phonon coupling constants for the ground state and excited state. For example, if the ground and excited state harmonic potential curves (or surfaces in higher dimension d>1) were not shifted relative to one another, it would mean that the phonon states were unperturbed by a *change* in the electron states, resulting in a small electron-phonon coupling for that transition. Generally, however, the equilibrium lattice configuration is a function of electronic eigenstates (see Eq. 3.9), and likewise, the electronic states are functions of the lattice configuration (see Eq. 3.5). Thus, by determining the shift in normal mode equilibrium position for a given electronic transition, one can infer the relative strength of the

electron-phonon coupling.

3.2.3 Scattering Cross Sections

We now briefly describe the theoretical foundation for electronic transitions, but we will incorporate the effect of the lattice using the configurational coordinate model. In the case of the photoluminescence experiments, we only consider emission transitions, whereas in the resonance Raman experiments, consideration of absorption transitions is more relevant. As is shown below, the absorption and emission processes are almost identical, except that we may make the simplifying assumption that the initial states of the emission transitions are all in the lowest vibronic level.

Kramers and Heisenberg[86] first treated the problem of light scattering involving the summation-over-states, which was later extended by Dirac[34] using radiation field theory. The total scattered power from an electron-lattice transition can be written as[172]

$$P_{I\to F} = I_0 \sigma_{I\to F}(E_L) \tag{3.16}$$

where the I and F refer to transitions from an initial state $|I\rangle = |\psi^{(g)}\phi^{(g)}\rangle$ to a final state $|F\rangle = |\psi^{(ex)}\phi^{(ex)}\rangle$ caused by an incident photon flux I_0 (given in photons $\mathrm{cm}^{-2}\mathrm{sec}^{-1}$) and $\sigma_{I\to F}(E_L)$ is the scattering cross section for a photon with energy E_L. In both experiments, all samples were considered to be homogeneous, based on the synthesis procedure (see Chapter 2), so that in this case, we can easily integrate over all directions and polarizabilities (isotropic homogeneous approximation). We can then write the Raman scattering cross section as

$$\sigma_{I\to F}(E_L) = \frac{8\pi e^4 E_s^3 E_L}{9\hbar^4 c^4} \sum_{\rho,\lambda} |(\alpha_{\rho\lambda})_{I\to F}|^2 \tag{3.17}$$

where the Raman polarizability tensor is given by

$$(\alpha_{\rho\lambda})_{I\to F} = \sum_V \frac{\langle F|m_\rho|V\rangle\langle V|m_\lambda|I\rangle}{E_V - E_I - E_L - i\Gamma} + \frac{\langle F|m_\lambda|V\rangle\langle V|m_\rho|I\rangle}{E_V - E_F + E_L - i\Gamma}. \tag{3.18}$$

Here E_L and E_s are the incident and scattered photon energies, while E_I, E_V and

E_F (not to be confused with the Fermi energy) are the initial (I), intermediate (V), and final (F) electronic-vibronic energies; m_ρ is the ρth component of the transition dipole vector; and Γ represents the homogeneous broadening linewidth. Note that the usual $E^4 \propto \omega^4$ dependence has been modified in order to be consistent with the incident flux measured in photons instead of energy. We further simplify the above expression for the Raman polarizability by considering only the (first) on-resonance term while neglecting the (second) off-resonance term. Using the arguments given in the preceding section regarding the decoupling of electronic and vibrational states, we rewrite the matrix elements as

$$\langle F|m_\rho|V\rangle = \langle \phi^{(g)}|\langle \psi^{(g)}|m_\rho|\psi^{(v)}\rangle|\phi^{(v)}\rangle = \langle \phi^{(g)}|M_\rho(Q)|\phi^{(v)}\rangle \tag{3.19}$$

where the superscript "v" now refers to the intermediate (excited) levels of the electronic system. Note that the pure electronic matrix element $M_\rho(Q)$ is still coupled (parametrically) to the ionic normal coordinates by way of the Adiabatic approximation.

Applying these simplifications to the expression for the polarizability, and then inserting this expression into Eq. 3.17, we can finally write for the resonance Raman scattering cross section as:

$$\sigma_{I\to F} = 3.81 \times 10^{-11} M^4 E_s^3 E_L |\sum_v \frac{|\langle \phi^{(v)}|\phi^{(g)}\rangle|^2}{\varepsilon_v - \varepsilon_g + E_0 - E_L - i\Gamma}|^2. \tag{3.20}$$

E_0 is the energy separation of the lowest vibronic level of the excited electronic state and that of the ground electronic state given by (see Fig. 3-1)

$$E_0 = E_{eg} - S\hbar\omega \tag{3.21}$$

while the energy difference of the vibrational states $|\phi^{(v)}\rangle$ and $|\phi^{(g)}\rangle$ can be given by

$$\varepsilon_v - \varepsilon_g = A\hbar\omega \tag{3.22}$$

where A is some integer. In the above expression Eq. 3.20 for the scattering cross section (which is given in Å^2/molecule), all energies (and linewidths) are given in eV; M is given in Å.

3.2.4 Raman Lineshapes

For the case of on-resonance Raman scattering, the Raman lineshape is found by inserting Eq. 3.20 into Eq. 3.16, where the CCD (charged coupled device) detection of photons will directly yield the scattered power flux (in terms of number of photons counted). For example, Eq. 3.20 is the expression we must consider for the case of MoS_2 samples excited with E_L=1.96 eV laser light, since this energy is very close to the excitonic gap of $E_{\text{exciton}} = 1.95$ eV (see sect. 3.5). For PPP, the benzenoid band gap is $\sim$3 eV, while the quinoid band gap is $\leq$1 eV, so that for laser energies in the visible, resonance is not expected to contribute to the Raman spectra for benzenoid PPP, but the resonant Raman effect does influence the relative line intensities of the quinoid Raman modes slightly, as we will see. Therefore, an approximate form for the resonance line intensity can be derived from Eq. 3.18 as follows (see Appendix A):

$$I \approx M^4(Q)|\langle 1|0\rangle|^2|\langle 0|0\rangle|^2 \left(\frac{(2E_0 - \hbar\omega_{ph})^2 + 3\Gamma^2}{[(E_0 - E_L)^2 + \Gamma^2][(E_0 + E_L - \hbar\omega_{ph})^2 + \Gamma^2]} \right) \tag{3.23}$$

where ω_{ph} is the phonon frequency, and the matrix elements, $\langle m|n\rangle \equiv \langle \phi^{(ex)}(m)|\phi^{(g)}(n)\rangle$, couple the 0 and 1 phonon vibronic states.

For graphite and well-carbonized samples, the resonance enhancement is sufficiently weak so that one can consider only non-resonant Raman scattering processes. Placzek[144] first showed that, in such a case, the Raman scattering cross section could be determined by considering only the ground state polarizability, greatly simplifying our formalism. The polarizability, α, is then due to the oscillation of electronic charge at normal mode frequencies in the ground state,[18]

$$\alpha^{(j)} = \frac{e^2/\mu_j}{\omega_j^2 - \omega_L^2 - i\omega_j\gamma_j}, \tag{3.24}$$

where μ_j, ω_j and γ_j are the effective mass, normal mode frequency and damping constant for the jth phonon mode. This then leads to the dependence of the line intensity on ω_L:

$$I_j(\omega_L) = I_{0,j}\frac{\omega_L^4}{(\omega_j^2 - \omega_L^2)^2 + \omega_L^2\gamma_j^2} \tag{3.25}$$

where $I_{0,j} = 4\pi e^4/3\mu_j^2c^4$. The total Raman spectrum is found by modulating this line intensity by the usual Lorentzian phonon lineshape which takes into account the phonon lifetime (or decay). In this work, the Lorentzian lineshape adequately describes the majority of the experimental data, although in some cases, an asymmetric lineshape is observed, which can be interpreted in terms of either overlapping lineshapes (e.g., Davydov splitting), or by using a Breit-Wigner-Fano analysis[17, 58].

3.2.5 Absorption and Emission Lineshapes

For emission lines, we neglect the consideration of virtual states, since we will generally expect intermediate (excited) states to be quickly depopulated, thereby non-radiatively filling some initial excited state prior to a radiative transition to the ground state. Using the Condon approximation, we can rewrite the matrix elements in Eq. 3.19 as

$$\langle\phi^{(g)}(m)|M_\rho(Q)|\phi^{(v)}(n)\rangle \approx M_\rho(Q_0^{(g)})\langle\phi^{(g)}(m)|\phi^{(v)}(n)\rangle \tag{3.26}$$

where we have implicitly used the harmonic approximation by writing the excited and ground state vibronic wavefunctions as functions of the harmonic oscillator quantum numbers, m and n, respectively. Using Fermi's Golden rule, the transition probability will be proportional to the square of these matrix elements, so that the intensity of the absorption band takes the form

$$I_{i\to f}(E_L) = I_0\sum_m |\langle\phi^{(g)}(m)|\phi^{(v)}(n)\rangle|^2\delta(E_0 + [m-n]\hbar\omega - E_L) \tag{3.27}$$

where the factor I_0 incorporates the purely electronic transition probability across an energy gap E_0 by absorbing a photon of energy E_L. The above expression must be

thermally averaged in order to be meaningful. Keil derived a method for explicitly writing the vibronic matrix elements as[77]

$$\langle \phi^{(g)}(m)|\phi^{(v)}(n)\rangle = e^{-S/2}\left(\frac{n!}{m!}\right)^{\frac{1}{2}}(-\sqrt{S})^{m-n}L_n^{m-n}(S) \tag{3.28}$$

where $L_n^{m-n}(S)$ are the associated Laguerre polynomials written as a function of the Huang-Rhys parameter S. The form for the emission bands takes on a much simpler form after considering the thermal averaging of the sums in Eq. 3.27. That is, as mentioned earlier, we expect only the lowest vibrational level of the excited electronic state to be populated at the time of emission, since non-radiative decay processes are expected to produce this state efficiently. Emission then takes place by transitions from this lowest vibrational level to $n \neq 0$ vibrational levels of the ground electronic state. This gives for the final form of the emission band shape,

$$I_{I\to F} = I_0 \sum_m \frac{e^{-S}S^m}{m!}\delta(E_0 - m\hbar\omega - E_L) \tag{3.29}$$

where the summation is over *final* electronic ground state vibrational levels. The result of Eq. 3.29 implies that the emission spectra will consist of a series of peaks separated by phonon energies of $\hbar\omega$ and will form a profile that strongly depends on the value of S. Namely, for small S, the envelope of the delta functions of Eq. 3.29 will be Poisson-like, while for larger S the envelope will look roughly Gaussian.

3.3 Experimental Details

Raman scattering experiments were performed under ambient conditions using a back-scattering geometry with laser excitation wavelengths (energies) 4880 Å (2.54 eV), 5145 Å (2.41 eV) and 6328 Å (1.96 eV). Laser intensity for the 4880 and 5145 Å lines was supplied by an air-cooled Ar ion laser, while the 6328 Å line was produced by a He-Ne laser. In order to prevent damage to the samples, an optical filter was used to reduce the incident power to 0.6 mW. Several locations on the sample surface were probed for each sample to ensure the reproducibility of each scan. Scattered light was

focused into a double grating monochromator fitted with a 200-400 μm slit. Scattered intensities were measured using a high-resolution liquid nitrogen cooled CCD camera.

A SPEX FluoroLog Model FL212 Spectrofluorimeter was used to measure the photoluminescence spectra of heat-treated PPP samples exposed to 350 nm light, selected by way of a double monochromator from a 450 Watt Xenon arc lamp source. The PL emission spectrum could then be measured using a CCD array.

3.4 Raman Spectra of Carbon Materials

3.4.1 PPP-based Carbons

Figure 3-2 shows Raman spectra taken for PPP-based samples heat treated over the broad range 700°C $\leq T_{\rm HT} \leq$ 2700°C. Although not shown in Fig. 3-2, additional spectra were taken for samples heat treated to 2400°C and 2900°C, so as to compare with the XRD data presented in section 2.1.2 and displayed in Table 2.1. In this T_{HT} regime (except for PPP-700), each spectrum exhibits two distinct features, one near 1600 cm^{-1} and the other around 1350 cm^{-1}. An additional third feature around 1260 cm^{-1} is observed for PPP-700, but this feature is quenched through heat treatment at higher temperatures. For $T_{\rm HT}$ >1000°C, we may identify these two features in the Raman spectra as the familiar Raman-allowed E_{2g_2} mode of graphite ($\sim$ 1580 cm^{-1}) and a disorder-induced mode arising from a breakdown in k-selection rules for graphite ($\sim$ 1360 cm^{-1}), as indicated by the dashed lines in Fig. 3-2. We see that the E_{2g_2} peak for lower $T_{\rm HT}$ is slightly upshifted, with respect to pure graphite, due to the scattering by disorder-induced non-zone center modes of slightly higher frequency (and probably some residual PPP A_g modes as well), but the peak frequency decreases with increasing $T_{\rm HT}$ to a value of 1585 cm^{-1} at 2700°C, nearly equal to the single crystal graphite value[179] of $\sim$1580 cm^{-1}. Figure 3-3 shows the shift of the high frequency $\sim$ 1600 cm^{-1} feature with T_{HT}, along with the corresponding full-width at half-maximum linewidth (FWHM). Although a smooth continuous shift of the peak frequency is observed, the linewidth first broadens by $\sim$55 cm^{-1} from 650 to 800°C

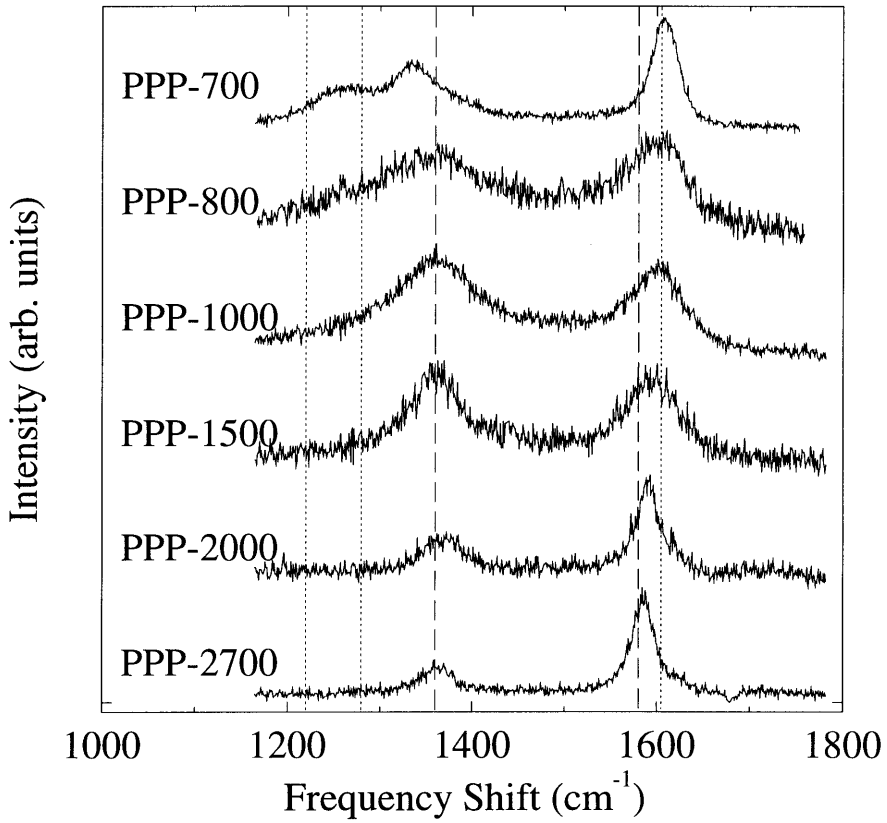

Figure 3-2: Raman spectra for several heat treated PPP samples. The PPP-700 sample exhibits an interesting 3-peak structure due to PPP mode remnants, whereas at higher T_{HT}, the usual 'disorder' and 'graphite' peaks are observed. For comparison, previously reported experimental Raman frequencies for graphite[132, 179] and PPP[88] are shown as dashed lines (1360, 1580 cm^{-1}) and dotted lines (1220, 1280, 1605 cm^{-1}), respectively.

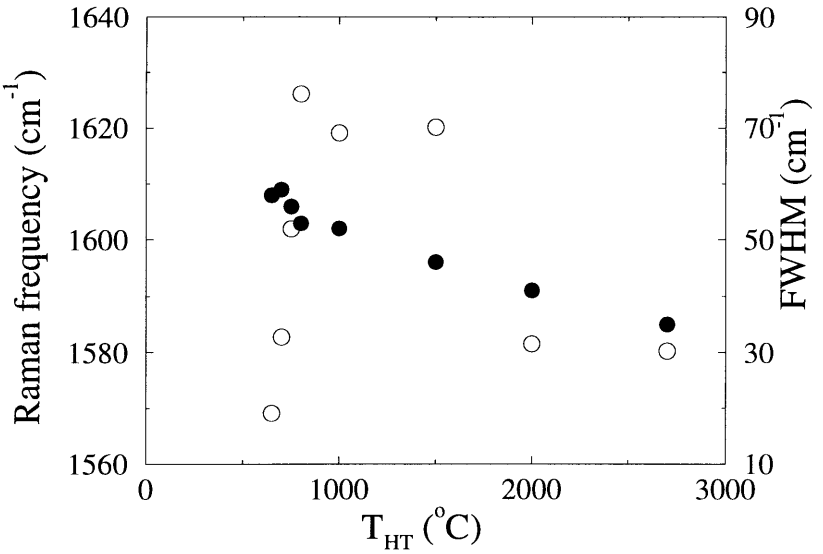

Figure 3-3: Observed shift in the high frequency C-C stretch mode (•) as a function of heat treatment temperature (left scale) and the corresponding full-width at half-maximum linewidth(○, right scale).

and then narrows by ~45 cm^{-1} from ~1000°C to 2700°C. An enhancement of phonon scattering, brought about by disorder, leads to a decrease in phonon lifetimes and an increase in the homogeneous linewidth. Hence, the Raman spectra shown in Fig. 3-2 reflects the ordered states of the PPP molecules and graphitic crystallites which are abundant at low-T_{HT} and high-T_{HT}, respectively. The most disordered state of the PPP-based systems appears to be produced between $800 < T_{HT} < 1500$°C when the PPP skeleton has been totally dismantled but while the graphene layers are not yet developed. Correspondingly, as the amount of graphitic order is increased through heat treatment, the intensity of the graphite E_{2g_2} peak (I_G) increases and the intensity of the disorder-induced peak (I_D) decreases[80, 179]. The ratio of these two peaks can be used as a measure of the degree of order within the 2D graphene sheets, whereas the a-axis microcrystallite size is proportional to the ratio I_G/I_D (see below). We note further that the ~ 1350 cm^{-1} peak frequency also shifts as a function of heat treatment temperature from roughly 1340 cm^{-1} for PPP-700 to 1360 cm^{-1} for PPP-2900. This effect is due to a quenching of PPP-derived peaks near 1330 cm^{-1} as T_{HT} is increased, as discussed below.

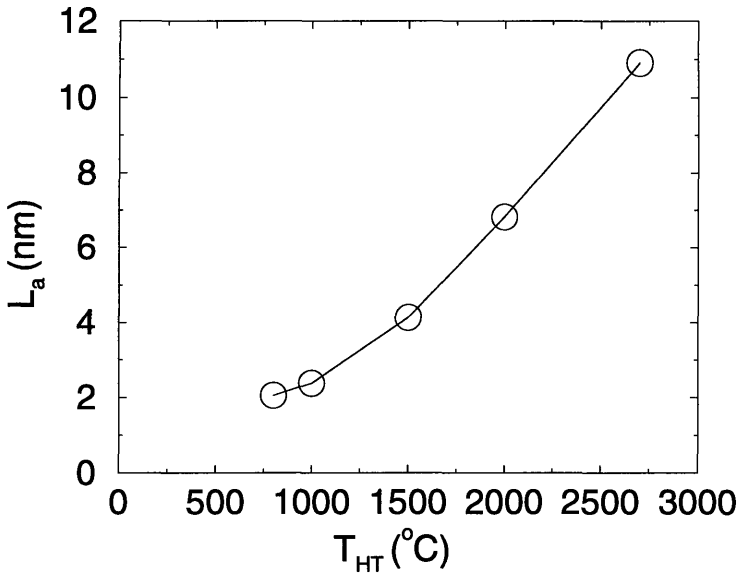

Figure 3-4: Dependence of the in-plane crystallite size, as approximated by L_a = 44Å (I_G/I_D), on T_{HT} for PPP-based samples heat-treated at various T_{HT} values.

It has been found that, for various graphitic carbons such as coke, glassy carbons and highly oriented pyrolytic graphite (HOPG), a simple relation between L_a and the I_G/I_D ratio is observed, yielding the empirical formula[80] for $\lambda_L \approx 5145$Å:

$$L_a = 44\text{Å}\ \frac{I_G}{I_D}. \tag{3.30}$$

This so-called Knight formula must be modified for $\lambda_L \neq 5145$ Å, although reasonably good fits are obtained for λ_L=4880 Å (see Appendix B). Figure 3-4 plots the values of L_a found using Eq. 3.30 for samples heat treated above 800°C. For T_{HT} below 1000°C, L_a is on the order of 20-30 Å but reaches a maximum value of 120 Å for T_{HT} near 3000°C. We note that evaluation of the in-plane crystallite size by way of the Raman lineshape analysis is typically not so accurate at smaller L_a, so that the values 20-30 Å are actually very rough approximations. This analysis was not applied to PPP-700, since the peaks observed in the Raman spectrum for this sample are influenced by the characteristics of the precursor more than by those of a typical graphitic material. In fact, a more careful study reveals that much of the peak intensity observed for PPP-700 arises from several A_g modes of a highly disordered PPP molecular crystal.

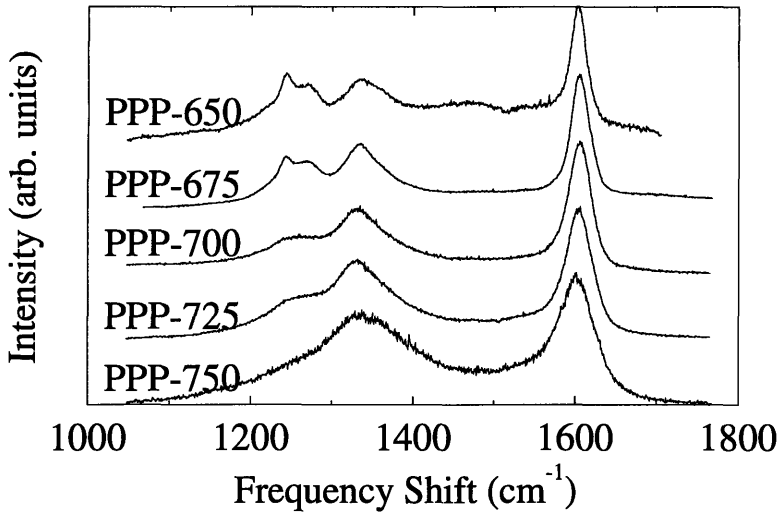

Figure 3-5: Raman spectra for PPP heat treated to various temperatures between 650°C and 750°C showing several PPP-derived A_g modes.

In order to study these modes more carefully in the $T_{\rm HT}$ regime about 700°C, Raman spectra were taken for samples heat treated from 650°C to 750°C in increments of $\Delta T_{\rm HT} = 25$°C. Figure 3-5 displays the results of these scans, revealing a detailed peak profile which quickly evolves over the given temperature range. Scans on lower $T_{\rm HT}$ samples proved difficult, since a strong luminescence background obscured the Raman peaks. This luminescence effect has been observed in non-heat treated Kovacic PPP, as well as in other pure polymer samples, and tends to prevent the use of laser excitations in the visible for Raman spectroscopy[87, 88].

Figures 3-6, 3-7, 3-8 and 3-9 show the results of a detailed least-squares fit to data collected at $\lambda_L = 4880$ Å(2.54 eV), showing several peaks that contribute to the Raman line shape of samples PPP-650, PPP-675, PPP-700 and PPP-725 (respectively) in the frequency range 1200–1400 $\rm cm^{-1}$. In Figs. 3-6 through 3-9, the dashed line corresponds to benzenoid-derived peaks while the dot-dashed line refers to quinoid-derived peaks. The dotted curves appearing in the aforementioned plots near 1360 $\rm cm^{-1}$ represent fits to an anomalous peak that is a mixture of a Raman activated IR PPP mode and the graphite disorder-induced peak. All peaks are well described by Lorentzian lineshapes, with a linear background term subtracted from the signal in

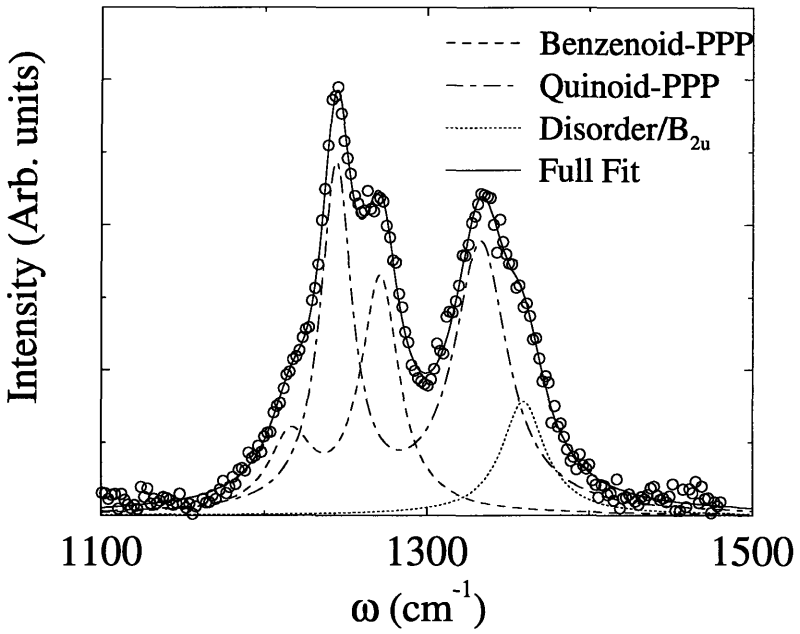

Figure 3-6: Low-frequency Raman spectra for PPP heat treated at 650°C. The solid line represents the whole fit while the dashed and dot-dashed lines are fits to benzenoid and quinoid Raman frequencies, respectively (see text).

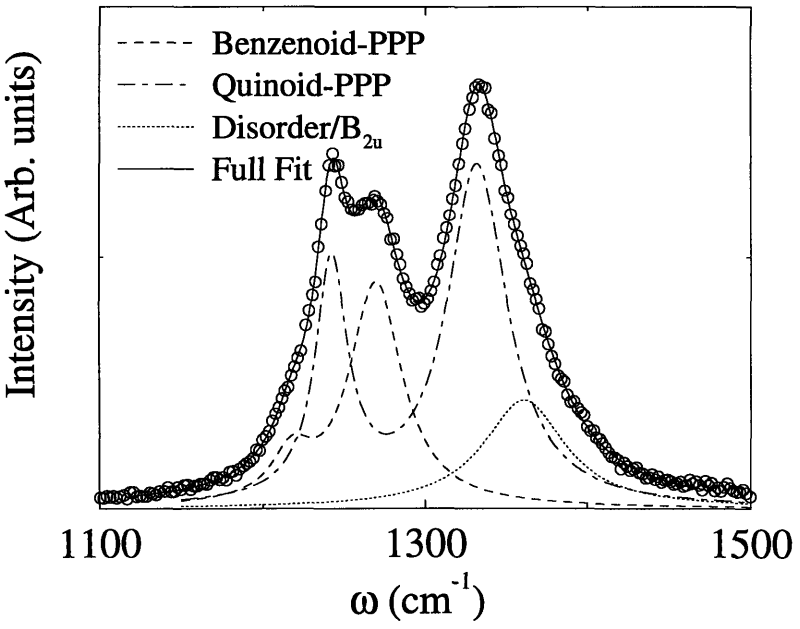

Figure 3-7: Low-frequency Raman spectra for PPP heat treated at 675°C.

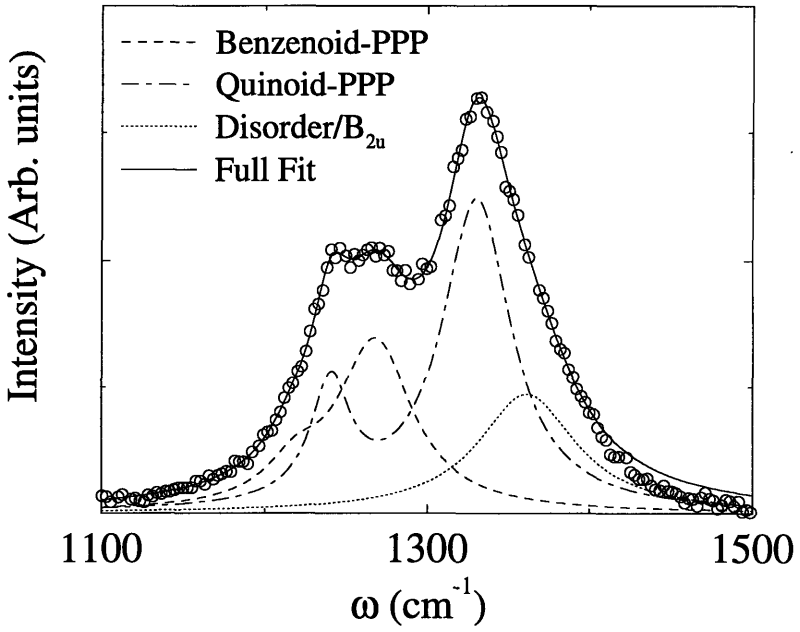

Figure 3-8: Low-frequency Raman spectra for PPP heat treated at 700°C.

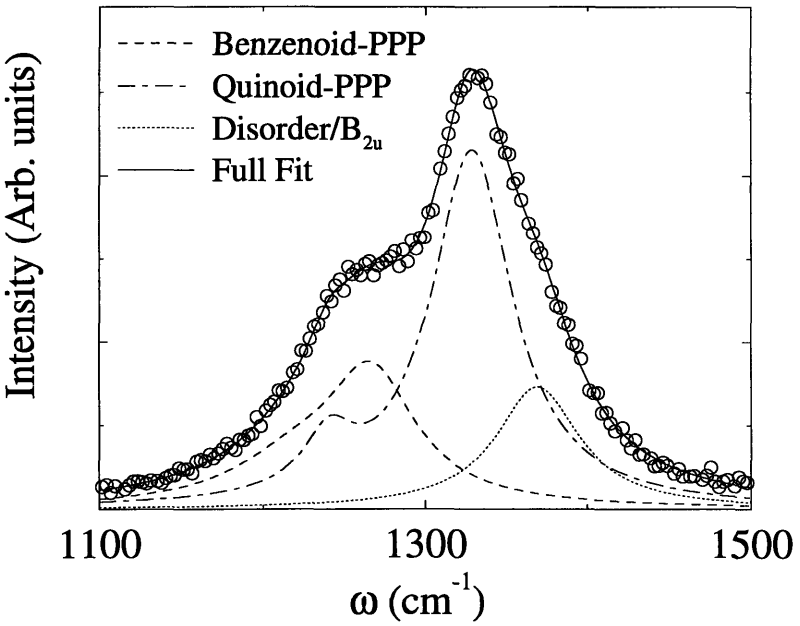

Figure 3-9: Low-frequency Raman spectra for PPP heat treated at 725°C.

Table 3.1: Fitted values (except for numbers in brackets, which were held fixed during the fitting procedure) for the peak positions and linewidths of the Raman spectra ($\lambda_L = 488.0$ nm) presented in Figs.3-6-3-9. All values are in cm^{-1}.

Sample	ω_1	ω_2	ω_3	ω_4	ω_5	γ_1	γ_2	γ_3	γ_4	γ_5
PPP-650	1216	1244	1271	1333	1360	32	23	28	40	32
PPP-675	1218	1242	1270	1332	1361	29	24	39	44	61
PPP-700	1219	1241	1268	1330	1362	44	29	56	52	73
PPP-725	(1220)	1241	(1267)	1329	1369	95	38	65	61	63

the fitting procedure. The aforementioned bands (at ~1240, ~1270 and ~1330 cm^{-1}) are well accounted for by the fit, but a better fit is obtained if small Lorentzians centered at 1216 and 1360 cm^{-1} are also used to fit the spectra. Therefore, a total of five primary peaks centered at ω_i (i=1–5) with corresponding linewidths, γ_i could be used to fit the low-T_{HT} PPP data and these peaks are shown as three separate fitting curves in Figs. 3-6 through 3-9. Values for ω_i and γ_i obtained from the least-square fits are tabulated in Table 3.1. These peaks also appeared (at slightly different frequencies) in scans performed at $\lambda_L = 514.5$ nm and $\lambda_L = 632.8$ nm, but as will be seen, the Raman features observed near 1300 cm^{-1} are not independent of λ_L. In Fig. 3-9, for example, we see that in the 1200–1400 cm^{-1} frequency range only the ω_4 band (~1330 cm^{-1}) remains prominent and consistently well-defined as T_{HT} is increased up to T_{HT}=700°C.

For samples with $T_{HT} \leq 725$°C, the ratios of various low-frequency peaks were evaluated and the results are tabulated in Table 3.2. Specifically, we evaluated I_{1220}/I_{1270}, I_{1240}/I_{1330} and I_{1270}/I_{1330}, where I_s is the integrated intensity of a peak centered at s cm^{-1}. The first two ratios have been experimentally found to be proportional to the average *conjugation length* of the PPP chains, but since the energy gap of the polymer, E_0, is (roughly) inversely proportional to the conjugation length, Eq. 3.23 can be used to derive the same result theoretically (see Appendix B). The ratio I_{1270}/I_{1330} essentially compares the scattered intensities from the breathing mode of each of the two possible conformations, benzenoid and quinoid, respectively, and could be monitored as an indication of the relative concentrations of the benzenoid

Table 3.2: Ratios of integrated intensities of PPP A_g peaks for samples PPP-650, PPP-675, PPP-700 and PPP-725, taken at $\lambda_L = 488.0$ nm.

Sample	I_{1220}/I_{1270}	I_{1240}/I_{1330}	I_{1270}/I_{1330}
PPP-650	0.35	0.74	0.62
PPP-675	0.15	0.38	0.58
PPP-700	0.05	0.30	0.58
PPP-725	—	0.09	0.38

to quinoid conformations. The information provided by the Raman intensity ratios I_{1220}/I_{1270} and I_{1240}/I_{1330} will be discussed in detail later, along with further discussion of the I_{1270}/I_{1330} intensity ratio.

The Raman spectra for PPP-based samples were also studied as a function of laser excitation wavelength λ_L, showing changes in both peak intensity and peak position, resulting from changes in λ_L. Figure 3-10 shows the Raman spectra for PPP-700 obtained at $\lambda_L = 4880$, 5145 and 6328 Å. The high frequency peak position is essentially independent of λ_L resulting in fitted values of 1605±1 cm^{-1}, with no observable frequency-dependent broadening. On the other hand, a significant change in the lower frequency spectrum is observed as λ_L is varied, particularly through the emergence of the structure centered around ω_2=1241 cm^{-1} with increasing λ_L. Furthermore, a shift of the ω_4 band is observed, going from 1333 cm^{-1} at $\lambda_L = 4880$ Å to 1323 cm^{-1} at $\lambda_L = 6328$ Å. In fact, the Raman intensity of all bands appearing between 1200–1400 cm^{-1} were more pronounced at longer excitation wavelengths with respect to the high frequency peak, but particularly modes ω_2 and ω_4. For example, the ratio of the integrated intensity of the ~1330 cm^{-1} and 1605 cm^{-1} bands, I_{1330}/I_{1605} increased from roughly 1.2 to 1.6 as λ_L increased from 4880 to 6328 Å.

The results of the Raman spectra of PPP-based carbons can explained as follows. A planarized PPP molecule in its ground state possesses D_{2h} symmetry, yielding the following in-plane modes at k=0:[168, 194]

$$5A_g + 5B_{1g} + 4B_{2u} + 4B_{3u}.$$

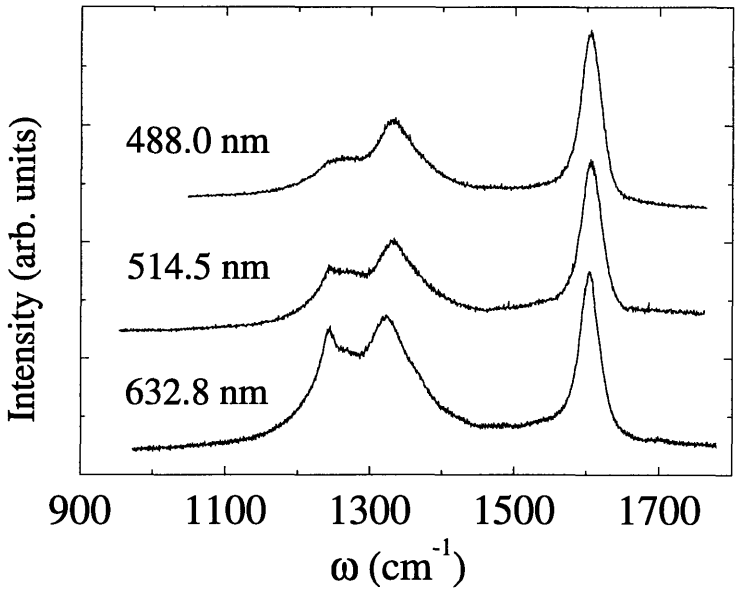

Figure 3-10: Raman spectra of PPP-700 excited at 488.0 nm, 514.5 nm, and 632.8 nm, showing a significant change in the lower frequency peaks with increasing λ_L.

Of these, 3 A_g modes produce strong Raman lines in the range 1100 cm^{-1} to 1800 cm^{-1}, namely at ~1220 cm^{-1} (inter-ring C-C stretch mode), ~1280 cm^{-1} (phenyl ring 'breathing' mode) and ~1600 cm^{-1} (intra-ring C-C stretch mode) for a benzenoid configuration (see Figs. 3-11 and 3-12). In the 488.0 nm Raman spectrum for PPP-650, PPP-675 and PPP-700, two peaks near 1220 and 1280 cm^{-1} can be observed, namely at $\omega_1 = 1216$ cm^{-1} and $\omega_3 = 1271$ cm^{-1}, along with several other peaks.

Although the benzenoid (non-degenerate) ground state of PPP produces lines around 1220 cm^{-1} and 1280 cm^{-1}, it is well known that a (higher energy) quinoid state exists for the molecule (Fig. 3-11), giving rise to Raman lines near 1240 cm^{-1} and 1330 cm^{-1}, slightly higher in frequency from those for the benzenoid system, due to a redistribution of C-C double-bonds. The quinoid structure has been theoretically shown to become stabilized in the presence of defects[14, 15] (such as charged dopants) due to its smaller band gap (E_g ~1 eV) and higher electron affinity, as compared to the benzenoid structure. Experimentally, Raman studies on doped PPP[87] and on charged PPP oligomer anions[59] have shown the existence of a quinoid structure through the emergence of the ~1240 and ~1330 cm^{-1} Raman bands. Since such a defect is usually well localized, a given benzenoid chain could deform into a quinoid

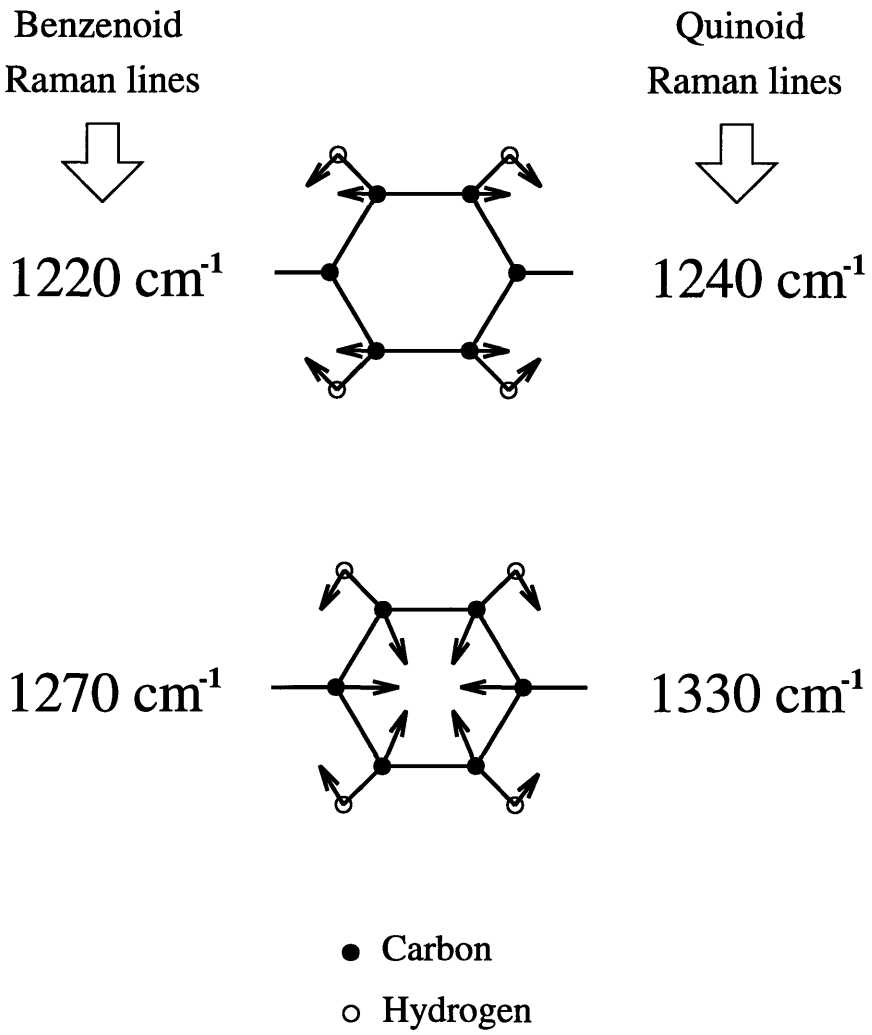

Figure 3-11: Atomic displacements for Raman modes in the frequency range 1200-1400 cm^{-1} along with experimental Raman frequencies for both benzenoid and quinoid bond arrangements.

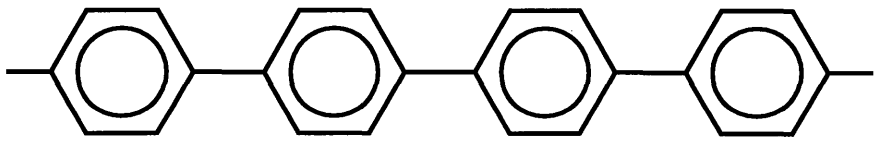

Benzenoid

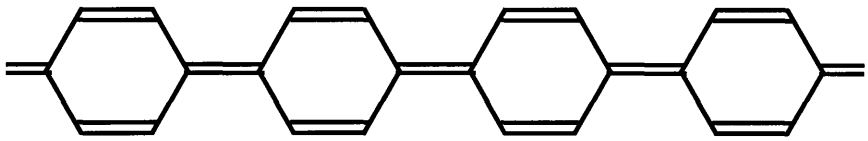

Quinoid

Figure 3-12: Schematic of ground state (benzenoid) and excited state (quinoid) conformations of pristine PPP chains. Due to the double bond bridging phenyl groups, the quinoid form is planar, while in the single-bonded benzenoid case, steric repulsion of the hydrogen species causes a $\sim 25°$ rotation of adjacent phenyl groups relative to one another.

conformation only near the defect, producing a polaron (for a single defect) or a bipolaron (for a double defect). Hence, for moderately defective PPP, both benzenoid and quinoid Raman lines are expected, while for the highly defective case, the quinoid spectrum is expected to dominate.

The Raman spectra for heat-treated PPP can then be easily explained by a defect-induced-polaron model. As a result of partial pyrolysis, many defects in the form of dangling sp^2 bonds are produced. These may be in the form of missing hydrogen atoms along the PPP chain, or edge sites of small condensed ring structures (see Fig. 3-13). In the presence of such a polarized defect, a neighboring PPP chain, initially in its ground state, will deform locally into a quinoid conformation, as shown in Fig. 3-13, thereby producing the Raman lines observed in the frequency range 1200-1400 cm^{-1}.

Moreover, from Figs. 3-6 through 3-9 we see that the quinoid modes appear relatively robust, while the benzenoid modes are mildly quenched in the Raman spectrum with increasing T_{HT}. The quenching of the benzenoid modes is monitored by the

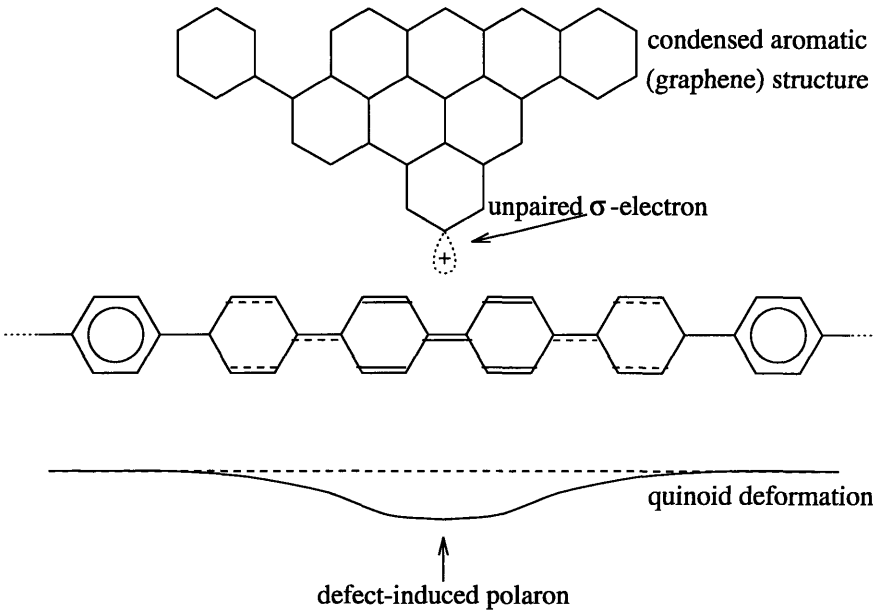

Figure 3-13: Defect-induced polaron model showing a polarized defect in the form of a dangling sp^2 bond (unpaired σ-electron) in the vicinity of a PPP chain.

decrease in the ratio of the ~1270 and ~1330 cm^{-1} mode intensities (I_{1270}/I_{1330}), especially as we go from PPP-700 to PPP-725, where a dramatic decrease in I_{1270}/I_{1330} is observed (see Table II). The inverse of this ratio may be used as a rough measure of the quinoid content in low-T_{HT} samples, and this result is plotted vs. T_{HT} in Fig. 3-14 for two values of λ_L. Thus, above T_{HT}=700°C a quinoid bond conformation is favored due to a high density of defects, leading to an enhancement of the intensity of the ω_4 mode. Ultimately, a planar configuration of phenyl groups is energetically favored as the heat-treated solid loses more hydrogen and eventually forms small graphene-like segments. In other words, planarized defective quinoid PPP segments are intermediate structures between non-planar benzenoid PPP and planar graphite. On the other hand, the C-C stretch mode, ω_{C-C}, producing the Raman peak near 1600 cm^{-1} remains unshifted as a result of heat-treatment in this T_{HT} range, which may imply that phenyl units are not being completely dismantled through carbonization over this T_{HT} range.

Figures 3-6 through 3-9 also show a shifting of the relative line intensities of the low-frequency (1200–1400 cm^{-1}) bands as a function of T_{HT}, which is related to the extent of π-electron delocalization over various lengths of linear PPP segments. It has

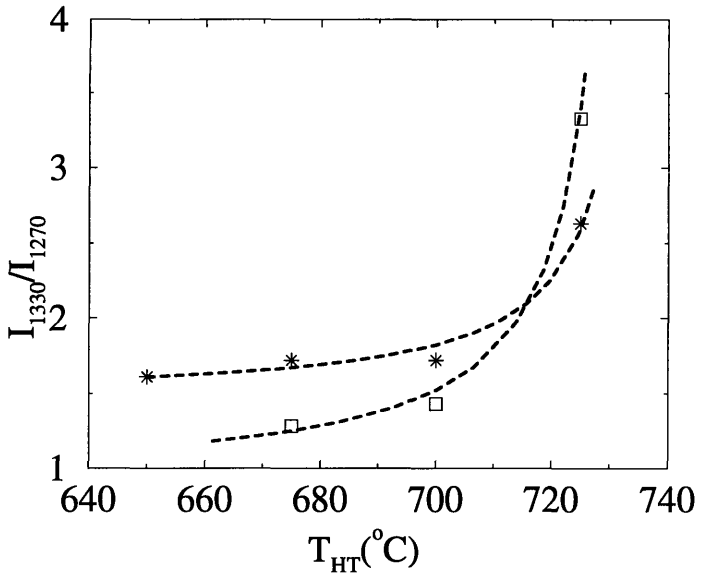

Figure 3-14: Plot of I_{1330}/I_{1270} vs. T_{HT} for λ_L=488.0 nm (*) and 514.5 nm (□), indicating an increase in quinoid content with increasing T_{HT}. Dashed lines are drawn as a guide to the eye.

previously been reported[88] that the ratio of the integrated intensities of the 1220 and 1270 cm^{-1} bands (I_{1220}/I_{1270}) in the benzenoid PPP Raman spectra increases with increasing number of phenyl units along a PPP chain. Physically, this is reasonable since the ω_1=1220 cm^{-1} mode involves an inter-ring coupling (see Fig. 3-11) which is strongly influenced by the effective conjugation length of the polymer. Conversely, the $\omega_3 = 1270$ cm^{-1} mode, which involves a phenyl ring breathing motion, is relatively insensitive to inter-ring coupling. In terms of the formalism of section 3.2, we would then expect the Huang-Rhys parameter S corresponding to the inter-phenyl mode to have a stronger dependence on conjugation length than the breathing mode. In Appendix B, I derive an approximate form for the ratio of intensities I_1/I_2 of Raman modes 1 and 2 belonging to the same electronic system:

$$\frac{I_1}{I_2} = \left(\frac{S_1}{S_2}\right) e^{-2(S_1-S_2)} \left(1 + \frac{(\varepsilon_1 - \varepsilon_2)}{E_0}\left[\frac{E_0 - E_L}{E_0 + E_L}\right]\right), \tag{3.31}$$

where S_1, S_2 are the Huang-Rhys parameters for each phonon mode defined such that the displacement of the multidimensional normal mode equilibrium positions can be decomposed into the various vibrational modes of the system. In fact, for laser

energies E_L less than the band gap E_0, the above expression gives the result that I_1/I_2 increases with E_0^{-1} for $S_1 \approx S_2$ which is consistent with previous experimental results[88]. Analysis of the integrated intensities of these bands (see Table II) for $650 \leq T_{HT} \leq 725$°C yields I_{1220}/I_{1270} ratios that decrease from 0.35 for PPP-650 to 0.03 for PPP-725 ($\lambda_L = 488.0$ nm), implying that the average number of linear benzenoid phenyl units on the polymer chains is decreasing rapidly over this range of T_{HT}. One possible mechanism to explain this decrease in intensity could be the complete scission of benzenoid PPP segments, producing a high number of short chain lengths and dangling bonds. However, such a high number of unpaired bonds is unfavorable since at ambient conditions two nearby dangling bonds along a PPP chain are expected to recombine to form a cross-linked chain. The more likely possibility is that the polymer cross-links at *meta*– and *ortho*– positions with increasing T_{HT}, thereby creating scattering centers for phonons involved in inter-ring processes. Although a similar trend is observed for the I_{1240}/I_{1330} ratio corresponding to quinoid peaks, no empirical relation between this intensity ratio and quinoid segment length has been reported in the literature. Nonetheless, we can infer the same dependence on conjugation length and note that the quinoid chain length is probably changing due to heat treatment.

It should be noted that, at these low heat treatment temperatures ($T_{\mathrm{HT}} \leq 700$°C), the PPP samples have lost much (though not all) of their hydrogen (see Fig. 2-3), and many molecular defects due to hydrogen vacancies will be present. Indeed, previous work on PPP thin films indicates that at temperatures near 675°C (for 1 hour residence time), H_2 and CH_4 gases only begin to evolve from the polymer[189]. Therefore, an interpretation of the Raman spectra for low-T_{HT} samples in terms of a disordered PPP, rather than a disordered graphitic carbon, seems more appropriate. The special electrochemical properties of PPP-700 might then be attributed to the presence of both a PPP-like short range structure and an immaturely formed disordered graphene arrangement. Raman analysis suggests that, at a T_{HT} of 700°C, the PPP samples are only partially carbonized and show the signature of a highly disordered quinoid-like PPP structure.

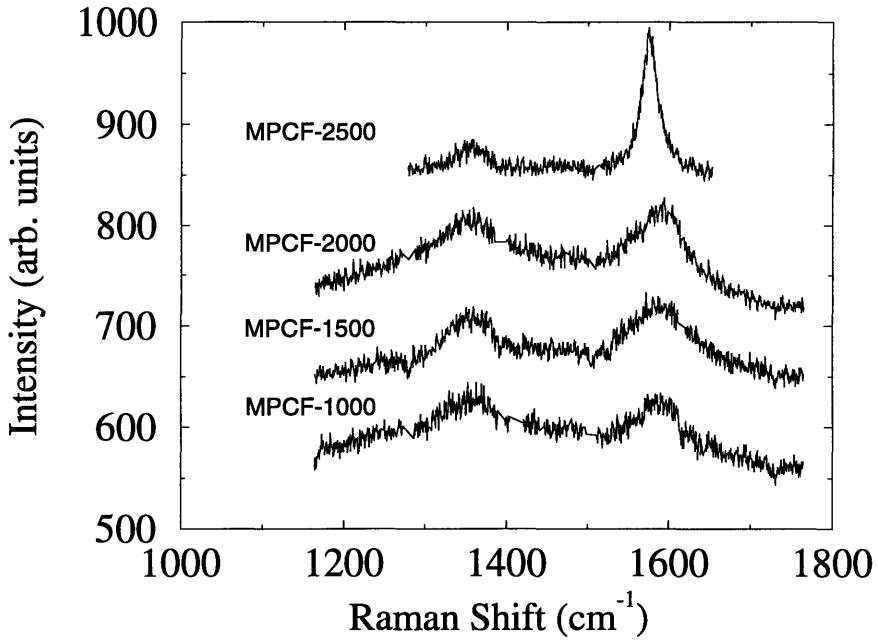

Figure 3-15: Raman spectra of MPCFs heat treated at various T_{HT}s for $E_L = 2.54$ eV. The data shown above were taken at the MIT Francis Bitter Magnet Laboratory.

3.4.2 MPCFs

Figure 3-15 shows the Raman spectra of MPCFs heat treated to various T_{HT} values above 1000°C. Since we are well above carbonizing temperatures, no precursor peaks could be resolved. As with the higher T_{HT} PPP samples, the Raman spectra seen in Fig. 3-15 have two prominent features, namely the D peak at ~1360 cm^{-1} and the G peak at ~1580 cm^{-1}. Since the samples in this case were not powder, but were actually small fibers, pressed pellets were not made, resulting in sample mounting difficulty and poor Raman scattering intensities.

Using a micro-Raman set up, however, Professor M. Endo was able to greatly enhance the Raman spectra of these samples by focusing laser energy on single fibers, and the results of that experiment are shown in Fig. 3-16. However, since the ratio of the two peaks (D, G) in the Raman spectra of carbon materials is known to be laser energy dependent, the usual Knight formula[80] which is used to evaluate the in-plane crystallite size for $E_L = 2.41$ eV ($\lambda_L = 514.5$ nm) is not applicable. I derive a more accurate form of Knight's formula and apply it to the case of MPCFs where

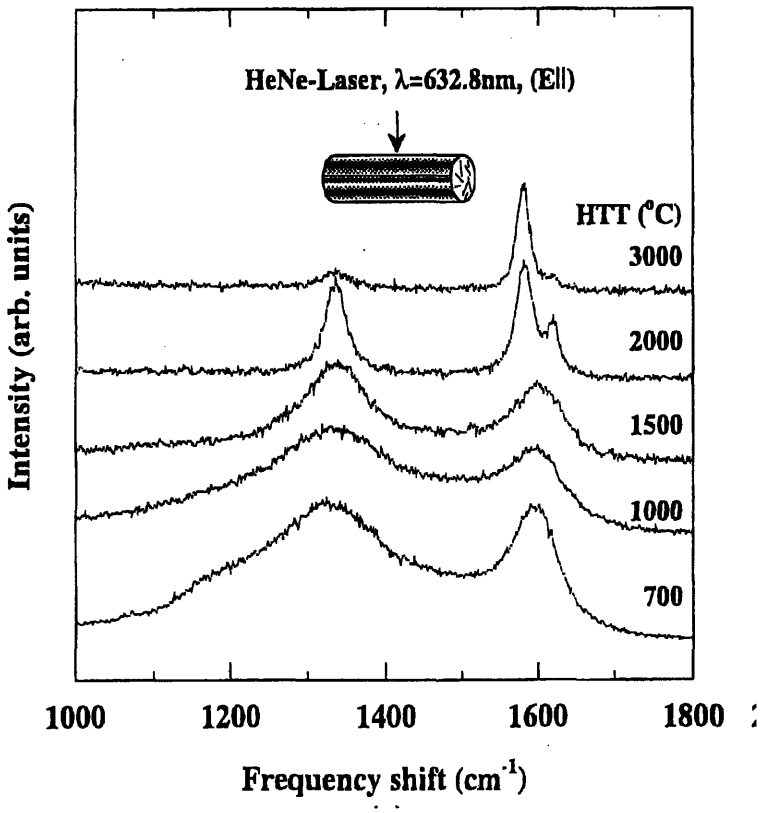

Figure 3-16: (micro)Raman spectra in the indicated geometry of MPCFs heat treated at various T_{HT} values for $E_L = 1.96$ eV ($\lambda_L = 6328\mathring{A}$)[40]. The data above was taken at Shinshu University, Nagano, Japan.

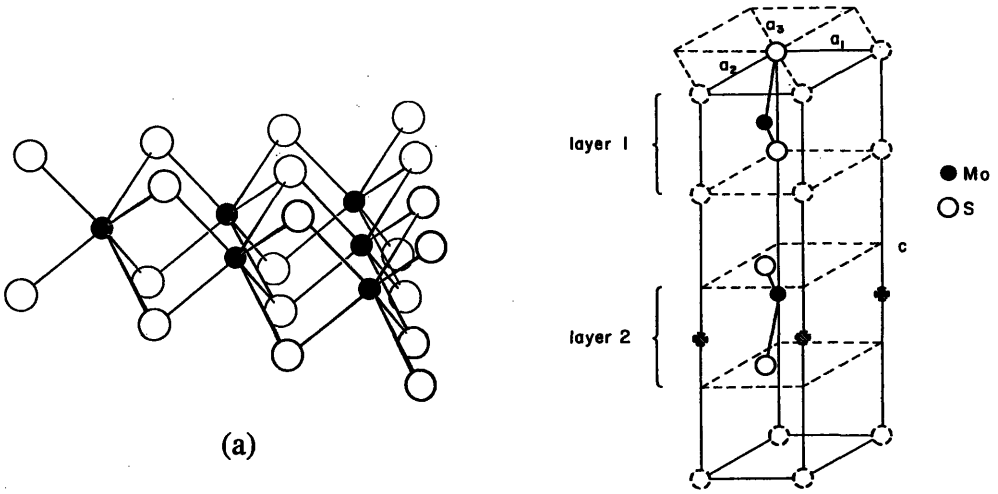

(a) (b)

Figure 3-17: (a) The coordination of molybdenum and sulfur atoms in a single layer of MoS_2 and (b) the primitive unit cell of 2H-MoS_2. The molybdenum atoms are the dark circles.

$E_L = 1.96$ eV ($\lambda_L = 632.8$ nm) to show that the Raman spectra are indeed consistent with XRD data. At E_L=1.96 eV L_a (in Å) is empirically given by

$$L_a = C(\lambda_L)R^{-1}(\lambda_L) \tag{3.32}$$

where $C(\lambda_L) \approx 110$ for $\lambda_L = 632.8$ nm and $R^{-1}(\lambda_L = 632.8\text{ nm})$ is the inverse ratio of I_D/I_G measured at . Figure B-2 in Appendix B shows the corrected L_a for MPCFs as a function of T_{HT} along with XRD data. Note that the estimated in-plane crystallite size of MPCF-based carbons approaches 400 Å, while that of PPP-based carbons (see Fig.3-4) is limited to ~120 Å for $T_{HT} \approx 3000$°C.

3.5 Raman Spectra of Molybdenum Disulfide Nanoparticles

The Raman spectra of bulk 2H-MoS_2 have been studied extensively[21, 157, 180]. The primitive unit cell and atomic coordination of the 2H-MoS_2 crystal structure

are shown in Fig. 3-17 showing the trigonal (2H) stacking of Mo and S atoms. A group-theoretical analysis of lattice vibrations in 2H-MS_2 (M=Mo, W) at the Γ point in the hexagonal Brillouin zone (BZ) has been previously published[187]. There are four Raman active modes in 2H-MoS_2, corresponding to symmetries (with measured frequencies in parentheses): E_{1g} (286 cm^{-1}), E^1_{2g} (383 cm^{-1}), A_{1g} (408 cm^{-1}) and E^2_{2g} (32 cm^{-1}). The atomic displacements of these Raman modes are shown in Fig. 3-18. In backscattering experiments on a surface perpendicular to the c-axis, the E_{1g} mode is forbidden.

The resonance Raman spectra of single crystal 2H-MoS_2 have been previously reported using laser energies near the optical absorption edge[169, 173]. The indirect and direct gaps of 2H-MoS_2 at room temperature are 1.2 and 1.95 eV, respectively; the A and B exciton energies are 1.88 and 1.95 eV, respectively[53]. These excitons are assigned to transitions at the (direct gap) K-point of the Brillouin zone, with K_4 and K_1, respectively, being the initial states, and K_5 the final state[23]. The resonance Raman scattering of 2H-MoS_2 was analyzed in terms of second-order-Raman (SOR) scattering due to the coupling of phonon modes to electronic transitions associated with the excitonic states[173]. An intense SOR band at 460 cm^{-1} is due to the 2×LA(M) overtone, while other SOR peaks are assigned to combinations of sum or difference bands involving phonons at the M point coupled to the LA(M) mode[21, 173]. If the exciting laser line is just above the 1s level of the A exciton, an additional peak appears at ~430 cm^{-1} which shifts to lower frequencies as the energy of the exciting laser increases. This peak is interpreted in terms of a two-phonon Raman process involving the successive emission of a dispersive longitudinal quasi-acoustic phonon and a dispersionless phonon, both vibrating along the c-axis[157].

Figure 3-19 displays the Raman spectra of IF-MoS_2 and 2H-MoS_2 platelets excited at 4880 Å, along with a least-square fit to the data. Two strong Raman peaks were observed at 383 and 408 cm^{-1} corresponding to the 2H-MoS_2 E^1_{2g} and A_{1g} modes, respectively. The weaker polarization-sensitive mode near 286 cm^{-1} was not observed at this excitation wavelength. As can be seen in Figure 3-19, the linewidths of the 383 and 408 cm^{-1} peaks broaden with decreasing crystallite size. The half-width at

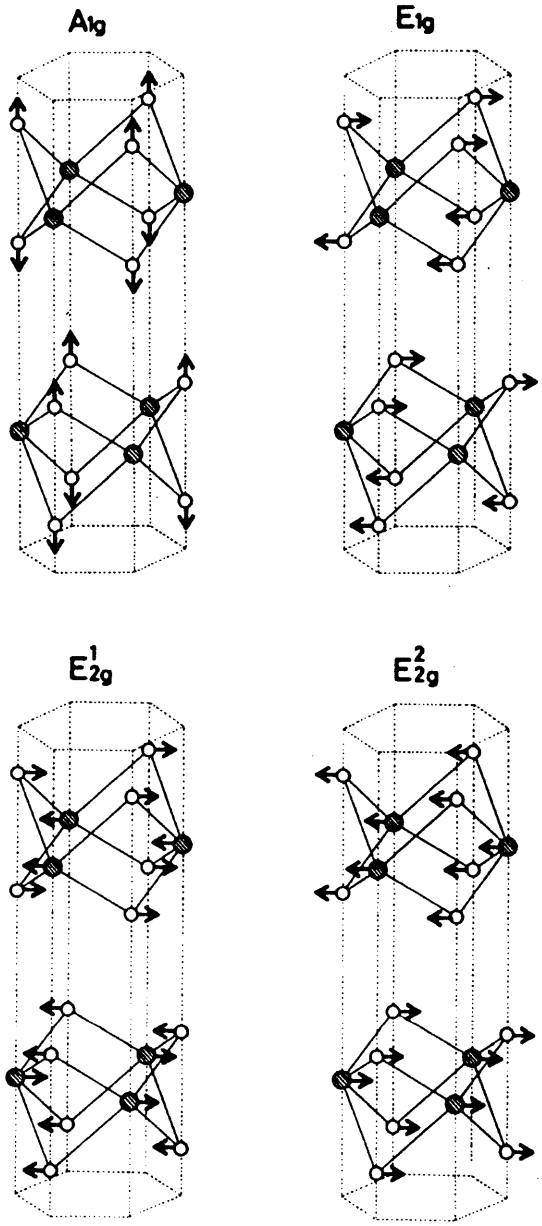

Figure 3-18: Raman-active normal modes in 2H-MoS_2. The large dark circles represent the molybdenum atoms.

half-maximum (HWHM) of both peaks increased from roughly 4 cm^{-1} for the 0.55 μm particles to 9 cm^{-1} for the 200 Å IF sample. The relative intensity of the 383 and 408 cm^{-1} peaks did not vary significantly as a function of crystallite size. Raman spectra of MoS_2 IF and nanoparticles excited with the 5145 Å line showed similar features to those obtained by the 4880 Å line. The observed broadening effect can generally be explained in terms of modifications to the space correlation function brought about by finite crystallite size. Theoretical studies on the effect of the finite size of graphite crystals[99] showed that by replacing the k-selection rule delta function and allowing non-zone-center phonons to participate in the Raman process, a wider Raman band should be observed for k=0 peaks.

Ideally, crystalline materials exhibit first-order Raman scattering only by phonons of approximately zero momentum. However, in polycrystalline materials, first-order scattering from non-zone-center phonons is activated by the disorder associated with finite crystalline size. For example, the disorder-induced peak near 1350 cm^{-1} observed in the Raman spectra of finite-size graphite particles[179] has been assigned to sharp features in the phonon density of states appearing near that phonon energy[134]. In the graphite dispersion relations, phonon bands at the M and K points of the hexagonal BZ are primarily responsible for the high density of states observed near 1350 cm^{-1}. Accordingly, with decreasing MoS_2 particle size, additional peaks are expected to appear at frequency positions that correspond to features in the density of phonon modes produced by phonons throughout the zone.

Figure 3-20 shows the resonant Raman spectra of MoS_2 nanoparticles taken by G. L. Frey at the Weizmann Institute using a laser excitation wavelength of 6328 Å. Although 6328 Å data was taken at both MIT (M. J. Matthews and G. L. Frey) and the Weizmann Institute (G. L. Frey only), the Raman setup at the latter location had superior optical components which allowed for Raman scans much closer to the laser line, and therefore low energy phonons (below 300 cm^{-1} could be probed. λ_L=6328 Å corresponds to a laser energy E_L=1.96 eV which is nearly equal to the B exciton energy of 1.95 eV. Indeed, using Eq. 3.20, the scattering cross section can be shown to increase by more than an order of magnitude (as compared to scattering at 4880

Å), thereby enhancing the phonon spectrum. The resonant Raman (RR) spectra of platelets 0.5 μm in diameter is similar to that of the bulk and includes peak broadening due to decreasing crystallite dimensions. In addition to the broadening of the peaks, however, the spectra of the nanoparticles (IF and platelets 30x50 Å) display additional Raman peaks at: 228, 250 and 498 cm^{-1}. We believe that these peaks are disorder-induced in origin, and correspond to contributions from phonons in the vicinity of the BZ edge, arising from the high density of phonon states.

Previous RR[169, 173] and inelastic neutron scattering (INS)[182] studies have shown that second-order Raman (SOR) processes involving the LA(M) phonon could be used to explain both the intense ~460 cm^{-1} peak, and other weaker peaks observed in the SOR spectra of MoS_2 bulk crystal. Both RR and inelastic neutron scattering (INS) studies found the frequency of the LA(M) phonon in question to be 230 cm^{-1}. Stacy et al. were also able from SOR spectra to estimate the frequency of the M-point optical mode (corresponding to the same branch as the zone-center mode) to be 410 cm^{-1}, close to the INS result of 397 cm^{-1}. Using similar arguments (and adapting the notation used in Ref. [173]), we can also deduce the frequencies of various BZ edge phonons. By considering several multiphonon peaks, we find that the frequency of the LA(M) phonon in the nanoparticle samples is about 228 cm^{-1}, which is slightly lower than the previously-reported result[173].

Enhanced Mo-Mo interactions, possibly caused by Mo sub-lattice disorder, could result in lowering the M point phonon frequency, as observed for single layer octahedrally coordinated 1T MoS_2[46, 154]. Accordingly, the 2H MoS_2 peak observed at 233 cm^{-1} in previous studies[169, 173] appears downshifted for the case of the nanoparticle samples, and is observed at 228 cm^{-1}. This downshift is also consistent with the frequency position of the intense asymmetric peak at 455 cm^{-1} which is the result of second-order scattering of the LA(M) phonon. The assignments of all multiphonon scattering peaks observed in the MoS_2 RR spectra are given in Table 3.3. All multiphonon bands involving the LA(M) mode are asymmetric. The dispersions of the E^1_{2g} and A_{1g} modes in the Γ-M direction are small, while the dispersion curve of the LA mode has an inverse parabolic shape near the M-point[182]. Consequently, the band

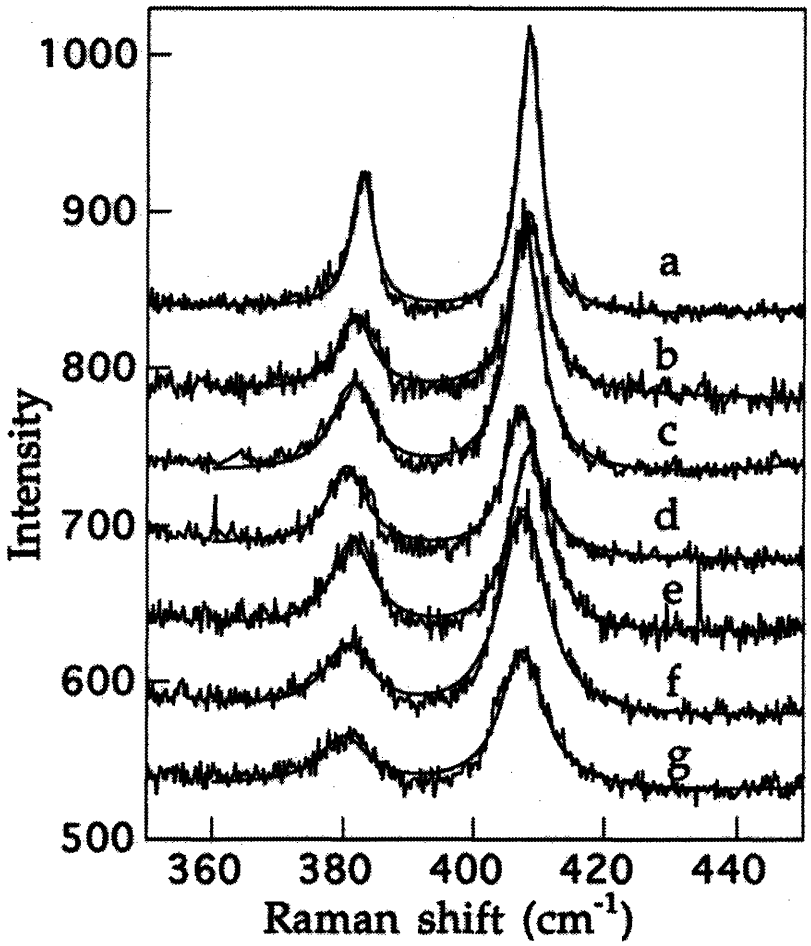

Figure 3-19: Raman spectra of various MoS_2 nanoparticles taken at λ_L=4880 Å showing the broadening of E^1_{2g} and A_{1g} lines with decreasing crystallite size. Shown from (a) to (g) (in decreasing sample volume) are: PL-MoS_2 5000 Å (a); PL-MoS_2 200x500 Å^2 (b); IF-MoS_2 1000-1500 Å (c); IF-MoS_2 800 Å (d); PL-MoS_2 50×300 Å^2 (e); IF-MoS_2 200 Å with 10-15 S-Mo-S layers (f); IF-MoS_2 200 Å with 5-10 S-Mo-S layers (g)[54].

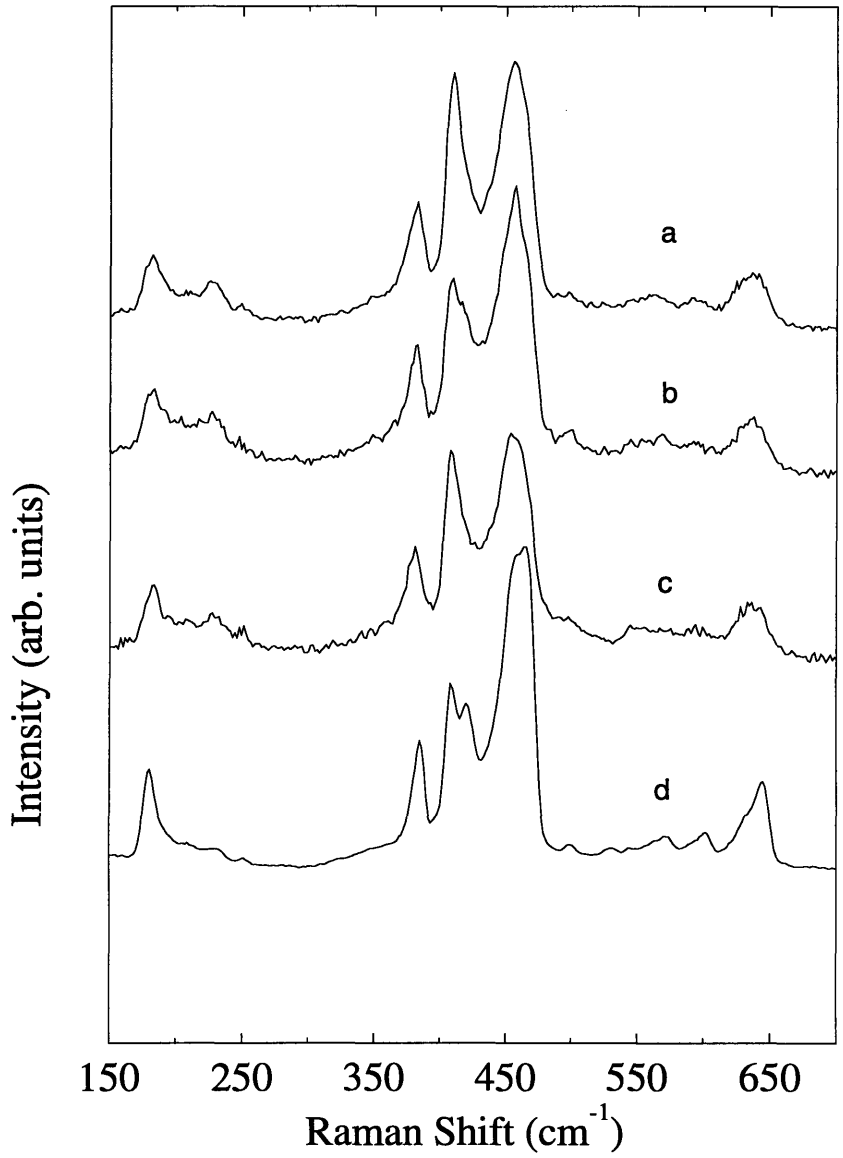

Figure 3-20: Resonance Raman spectra of MoS_2 nanoparticles taken at λ_L=6328 Å for IF-MoS_2 200 Å (a); IF-MoS_2 800 Å (b); PL-MoS_2 50×300 Å^2 (c); PL-MoS_2 5000 Å (d)[54].

at 636 cm^{-1}, which is assigned as a combination mode of the A_{1g} and LA(M) modes, is asymmetric with stronger contributions to the peak from the lower frequency side. On the other hand, the peak at 182 cm^{-1}, assigned to the difference process between the A_{1g} and LA(M) modes, is asymmetric, with peak contributions favoring higher frequencies (see Fig. 3-20). Thus, the asymmetric shape of the second-order bands involving the LA(M) phonon supports our assignments.

In terms of the new features in the RR spectra of the smaller nanoparticles, we first point out that the peak located at 228 cm^{-1} occurs at exactly the same frequency as that of the LA(M) phonon. We believe that the appearance of this feature is similar to the 1350 cm^{-1} peak in small crystallite graphite systems, as described in section 3.4. Namely, that the peak in the density of phonon modes found near a frequency of 230 cm^{-1} is the primary source of this Raman band which appears only in the smaller nanoparticle samples. Although K-point acoustic phonons may contribute, calculations of zone-edge frequencies[154] show that the K-point LA phonon is about 30 cm^{-1} lower in frequency than that of the M-point LA phonon. We believe that the peak observed at 228 cm^{-1} is a disorder-induced peak arising from LA(M) phonons. The possibility of contaminants is ruled out due to the high purity of the MoO_3 precursor[47], and the fact that the strong MoO_3 Raman bands lie outside of the 200-240 cm^{-1} frequency range.

Inclusion of disorder could also be the cause for the appearance of the other two new peaks at 250 and 498 cm^{-1}, in that the 250 cm^{-1} peak corresponds to scattering of a zone-edge phonon, while the peak at 498 cm^{-1} would then correspond to a second-order scattering process involving two such zone edge phonons. Phonon dispersion and density of phonon modes calculations for MoS_2[182] have shown that a peak in the density of phonon modes due to a low-lying TO branch could fall in the range 250-300 cm^{-1}, although INS experiments were unable to measure the frequencies of such phonons due to geometrical constraints. Ultimately, further inelastic neutron scattering studies spanning a larger fraction of the Brillouin zone would be necessary to establish whether 2H MoS_2 supports a high density of phonon frequencies near 250 cm^{-1}.

Table 3.3: Tabulated Raman bands observed in MoS_2 nanoparticles as compared to bulk.

2H-MoS_2[173] cm^{-1}	PL-5000 cm^{-1}	PL-50×300 cm^{-1}	IF-800 cm^{-1}	IF-200 cm^{-1}	Symmetry Assignments
177	179	184	182	182	$A_{1g}(M) - LA(M)$
		228	228	228	$LA(M)$
			250	250	edge phonon
287				286	$E_{1g}(\Gamma)$
383	384	381	383	381	$E^1_{2g}(\Gamma)$
409	409	408	409	409	$A_{1g}(\Gamma)$
	419				
466	460	455	455	455	$2 \times LA(M)$
		498	498	498	edge phonon
529	529				$E_{1g}(M) + LA(M)$
572	572	~560	567	567	$2 \times E_{1g}(\Gamma)$
607	601	595	593	593	$E^1_{2g}(M) + LA(M)$
643	644	636	636	636	$A_{1g}(M) + LA(M)$

As was also observed in the carbon-based systems, the Raman spectra of nanoparticles of MoS_2, both under resonance and non-resonance conditions, clearly show the effects of confinement and disorder in these layered systems. Specifically, the linewidths of the two strongest first-order modes at 383 and 409 cm^{-1} are observed to broaden with decreasing particle size. This is consistent with the phonon linewidth data given in Table 3.1 for PPP-based samples. Moreover, new peaks are observed in the MoS_2 RR spectrum which are tentatively assigned to zone-edge phonons or combination modes. Both of these features in the Raman spectrum are direct results of the finite nanoparticle size.

3.6 Photoluminescence

Turning now to the photoluminescence (PL) experiments, this technique becomes especially powerful when the electronic absorption edge of a given material is sharp, and when the carrier concentrations are low enough to quench electronic (Drude) screening. Polymer samples, which are both insulating and have nearly dispersionless

LUMO levels become ideal for PL investigation. The sharp transition energies also allow one to observe the vibronic levels discussed in section 3.2. In the following section, I describe PL measurements of heat-treated PPP samples with T_{HT} values up to 700°C. As will be discussed in Chapter 5 (section 5.3), the conductivity increases drastically above $T_{HT} = 700$°C as the polymer is carbonized, preventing PL studies above this critical T_{HT}.

3.6.1 Vibronic Structure of PPP-based Carbons

In order to study defects in the polymer precursor of PPP-based carbons, photoluminescence spectra were measured, taking advantage of the large scattering cross section for electronic transitions between molecular orbitals of PPP. Photoluminescence spectra were collected from samples PPP-600, PPP-650, PPP-675 and PPP-700 as well as from as-prepared (non-heat-treated) PPP, and these spectra are shown in Fig. 3-21. All the samples were excited at 3.54 eV (350 nm) to ensure electronic excitation into the LUMO levels which are separated from the HOMO levels by an energy gap of ~3.4 eV[158]. The sharp feature occurring at 1.77 eV (700 nm) in each of the PL spectra is due to the second-order interference of the excitation line. The dominant feature in the PL spectrum from the as-prepared PPP sample, using the Kovacic method, is the broad red PL structure centered at 1.86 eV (668 nm) with a shoulder at 1.71 eV (726 nm). The photoluminescence from the pristine PPP sample also showed well-defined spectral features in the blue-green located at 2.92 eV (425 nm), 2.75 eV (452 nm), 2.59 eV (480 nm) and 2.41 eV (515 nm). We note that, these energy values are all separated from one another by about 0.17 eV. Heat-treated samples showed a large reduction in red emissions as compared with the as-prepared sample, but still showed distinct structure at blue-green wavelengths. The photoluminescence from the PPP-600 sample consists of similar contributions in the blue-green as compared to the as-prepared sample, but the various contributions in the red are no longer distinct and are less dominant. The ratio of the total intensity of the blue-green PL to the red PL is four times lower in the as-prepared PPP sample (0.03) as compared to PPP-600 (0.14). However, the intensities of the blue-green contributions in the

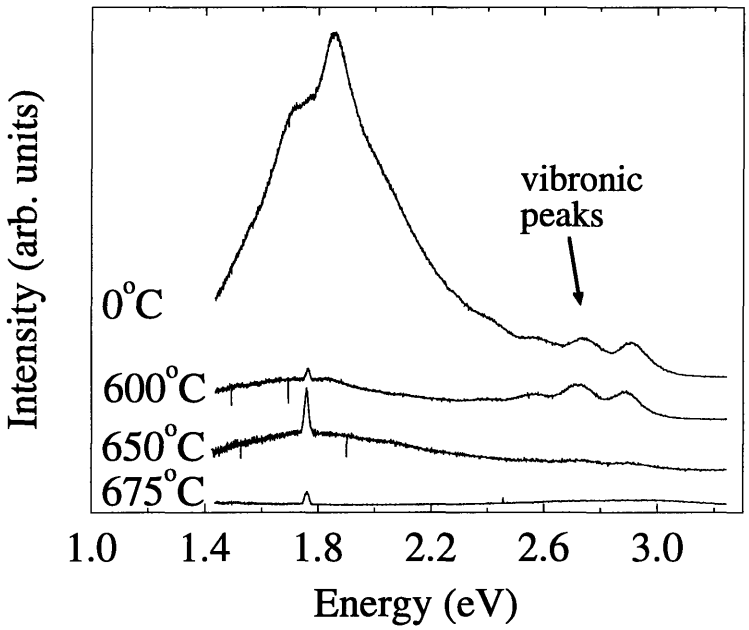

Figure 3-21: Plot of photoluminescence emission vs. energy for samples of PPP subjected to different heat-treatment temperatures (T_{HT}=0°C, 600°C, 650°C and 675°C), where T_{HT}=0°C refers to the as-prepared sample. The sharp feature near 1.8 eV is due to the second-order interference of the excitation line (3.54 eV in energy).

PPP-600 PL spectrum remain quite strong, with a spectral resolution comparable to that of the as-prepared PPP sample. The intensity of the photoluminescence in the PPP-650 sample is overall lower than that in the PPP-600 sample but the blue-green and red PL emissions are both still present. The blue-green emission lines of the PPP-650 sample are not as well resolved and the contribution at 2.41 eV (515 nm) has disappeared. Some featureless photoluminescence emission from the PPP-675 sample is found at around 2.95 eV (420 nm), but there is no red photoluminescence. There is no detectable PL from the PPP-700 sample.

The photoluminescence from non-heat-treated PPP synthesized by various methods has been previously reported. Heim *et al.* reported photoluminescence from as-prepared PPP synthesized by the Kovacic method with excitation of 330 nm (3.76 eV), showing structured peaks in the blue-green region and a broad structureless peak in the red[65]. These peaks were also reported by Rzepka *et al.* who used laser excitation at 413.1 nm on pristine PPP prepared by the Kovacic method. [151] They

compared the PL spectrum from PPP-Kovacic with the PL from PPP prepared by the Yamamoto method [191] and from electro-polymerized PPP[45]. They found the red peak to be present in only the PPP prepared by the Kovacic method, while the PPP prepared by other methods yielded only a series of PL bands in the blue-green, which are identified with a fundamental emission line along with its phonon sidebands. However, the effect of near-carbonizing T_{HT} on the PL of PPP is presented in this work for the first time, and shows that only the *as prepared* Kovacic samples exhibit a strong red luminescence. The blue-green peaks in the PL spectrum have been attributed to the intrinsic signal of the polymer, while the broad red peak (extrinsic signal) has been identified with structural defects in the sample resulting from the method of synthesis[151]. A possible origin of the red peak could be the presence of macrocycles[55] or other types of condensed aromatic ring structures. Lerner showed how condensed, aromatic ring structures could be produced through parasitic doping by the chlorine from the catalyst used in the synthesis[98]. We therefore subtracted the broad red peak from the PL spectra for the pristine polymer, in analyzing the PL spectra from the heat-treated PPP-600 and PPP-650 samples. The PL spectra resulting from the subtraction are shown in Fig. 3-22.

The contributions to the blue-green emissions of the PL spectrum arise from transitions between electron-lattice coupled states. Thus, the lineshapes will be given by Eq. 3.29, assuming fast non-radiative decay of $n \neq 0$ excited electronic state phonons. The zero-temperature "Franck-Condon factors" can then be defined as an approximation of Eq. 3.28,

$$| \langle\langle \chi(\nu_i) | \chi(0) \rangle\rangle |^2 = \frac{e^{-S_i} S_i^{\nu_i}}{\nu_i!} \tag{3.33}$$

and these factors determine the relative amplitude of the phonon sidebands in the photoluminescence emission spectrum of the polymer. The index ν_i is the number of phonons of a particular mode i in the ground state vibronic potential and $\chi(0)$ pertains to the lowest level of the excited state vibronic potential. The appearance of vibronic structure requires a finite displacement (ΔQ_{eg}) and therefore a finite Huang-Rhys parameter S_i must be taken into account.

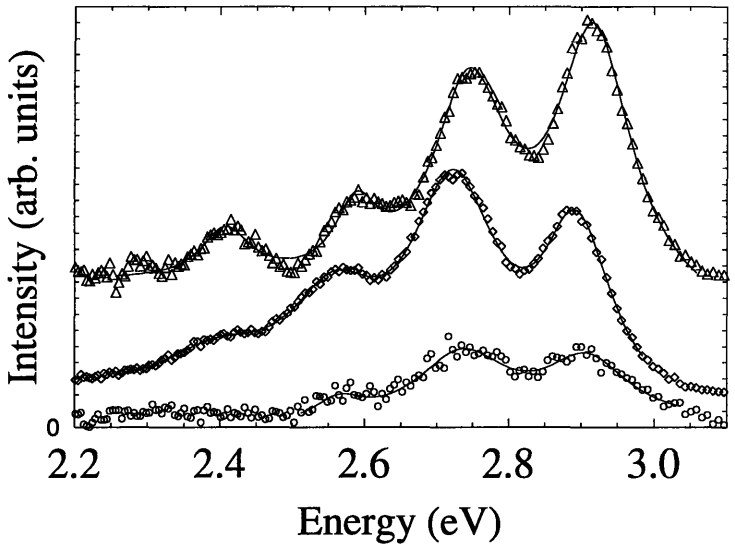

Figure 3-22: Plot of the blue-green photoluminescence vs. energy for PPP samples with T_{HT}=0°C ($\triangle$), T_{HT}=600°C ($\diamond$), T_{HT}=650°C ($\circ$). The data curves shown here are the results of the subtraction of a broad background peak (corresponding to the observed red peak) from the spectra shown in Fig. 3-21. Each solid line is a fit to a series of Lorentzian lineshapes.

To fit the emission spectrum, we consider a Franck-Condon progression of Lorentzians written in terms of a product ($\prod_i$) of vibronic matrix element square amplitudes

$$I(\hbar\omega) = \sum_{\nu_i} \frac{1}{1 + \frac{4}{\Gamma_{\nu_i}^2}(E_L - E_0 + \sum_i \nu_i \hbar\omega_i)^2} \times \prod_i |\, \langle\!\langle \chi(\nu_i) \,|\, \chi(0) \rangle\!\rangle \,|^2 \qquad (3.34)$$

where Γ_{ν_i} is the linewidth broadening parameter for the ith mode with occupation ν_i, and E_0 is the energy of the first emission line in the PL spectrum resulting from the transition from the lowest level of the excited state vibronic potential to the lowest level of the ground state potential.

Since the blue-green contributions to the PL emission spectrum are separated from one another by a constant energy value (0.17), we will, for simplicity, fit the data by considering only one phonon, corresponding to the approximation that only a single Raman-active phonon mode is involved in the electron-phonon coupling (ω_{ph}). We therefore fit the emission data to parameters ω_o, ω_{ph}, S and the various Γ_ν values. The results obtained for the four samples with different T_{HT} values are listed in Table 3.4.

Table 3.4: Values for the zero-phonon assisted transition energy ($\hbar(2\omega_0)$), phonon energy (E_0), Huang-Rhys parameter (S), and the FWHM linewidths of four prominent peaks (Γ_0, Γ_1, Γ_2, Γ_3) for samples PPP-0, PPP-650 and PPP-675.

Sample	E_0	$\hbar\omega_{ph}$	S	Γ_0	Γ_1	Γ_2	Γ_3
	eV	eV	–	eV	eV	eV	eV
PPP-0	2.92	0.17	0.77	0.12	0.13	0.13	0.08
PPP-600	2.89	0.17	1.19	0.12	0.15	0.16	0.20
PPP-650	2.91	0.17	1.14	0.21	0.16	0.41	—

The value of $\hbar\omega_{ph}$ for all three samples was found to be very close to 0.17 eV (=1370 cm^{-1}). This indicates that the electronic transitions are coupling to modes in the 1200-1400 cm^{-1} region of the Raman spectrum, with ω_{ph} being close to ω_4 ($\sim$ 1330cm^{-1}) as determined by our Raman measurements. However, because of the large vibronic energy level linewidths ($\sim$ 0.15 eV), we cannot resolve the individual phonon modes in the frequency range 1200–1400 cm^{-1} (separated by $\sim$0.01 eV) that may be coupled to the radiative transitions. From the Raman spectra taken on disordered PPP we see that there is a high density of phonon modes in this region of the vibrational spectrum. We further note that the separation of the first two prominent (and well-resolved) PL peaks in the pristine PPP spectra was carefully evaluated using only the first two prominent vibronic peaks and yielded a phonon energy of 0.165$\pm$0.0015 eV or 1330$\pm$12 cm^{-1}. The fact that the vibronic energy levels are separated by quinoid phonon energies ($\sim$1330 cm^{-1}) may give indirect evidence of mid-gap defect states formed by a cross-over to a quinoid conformation.

Leising *et al.* suggested that the primary source of PL emission in Kovacic PPP was from radiative recombination of electron-hole pairs in an exciton-polaron complex[97]. These polaron mid-gap states are separated by the quinoid band gap for highly quinoidal structures, which would produce emissions in the energy range 1-2 eV. This would explain the strong resonance effects observed in the quinoid Raman spectra when λ_L is in the red. However, from Franck-Condon analysis, the band gap E_0 appears to be much larger (see Table 3.4) than a pure quinoid band gap. Although we treated only the ground vibronic state in the conduction band when considering emis-

sion lines, inclusion of higher-lying non-zero phonon states in the conduction band would shift the resultant band gap to values closer to 1.9 eV. Thus, if we consider matrix elements of the form $|\langle\chi(\nu_i)|\chi(\nu_j)\rangle|^2$ where $\nu_j \neq 0$, transitions from higher vibronic states in the conduction band to non-zero energy vibronic states in the valence band would take place over a smaller energy gap as compared to the zero-phonon case treated above.

Returning to the zero-phonon transitions, the values of the FWHM for the individual transitions (Γ_0, Γ_1, Γ_2, Γ_3) increase with higher heat-treatment temperatures T_{HT}. The increase in linewidths with increasing T_{HT} is consistent with a reduction in the lifetime of the vibronic levels above the ground state, until the fourth transition (with linewidth Γ_3) for PPP-650 becomes too broad to be resolved. As the polymer is heated, it loses hydrogen, the phenyl rings flatten (increase their quinoid content), and the polymer chains begin to cross-link. The amount of cross-linking, then, will be strongly correlated with the % loss of hydrogen, which for PPP-600 and PPP-650 is about 6% and 16%, respectively (see §2.1.1). As the cross-linking continues, it eventually begins to disrupt the photoluminescence mechanism, since the defects associated with cross-linking would act as scattering centers for the phonons and would also enhance non-radiative processes. Hence, the electronic energy levels involving phonon states (the vibronic levels of the ground state) would tend to broaden with a decreasing lifetime, yielding broader PL bands with increasing T_{HT}. This is indeed observed for the case of the PPP-650 sample where the linewidth of the zero phonon peak is almost twice that of PPP-0. On the other hand, the spectrum for PPP-600 shows only a modest change in linewidth, showing that the increase in defect density (produced by the 6% H loss) is not sufficient in this sample to produce additional broadening.

The value of the Huang-Rhys parameter (S) increases from 0.77 for the pristine polymer to 1.19 for PPP-600 and 1.14 for PPP-650. This higher value of S indicates an increase in the difference of electron-phonon coupling constants ($\Delta\lambda_{el-ph}$) between the ground and excited states in the PPP-600 and PPP-650 samples over the value in the pristine polymer. This increase in $\Delta\lambda_{el-ph}$ is induced by the heat-treatment

of the polymer and arises from the increase in the number of defect centers in the polymer, such as the one indicated in Fig. 3-13. Since such defects are localized on either adjacent chains or segments, they will tend to couple to electronic states of adjacent polymer chains that are particularly delocalized in space. The conduction band ("anti-bonding") states, then, should be expected to be more effectively coupled to nearby defect states as compared to the valence band ("bonding") states, thereby bringing about different changes in the electron-phonon coupling of these two types of electronic states.

3.7 Future Work

The present chapter showed that Raman and resonance Raman (RR) spectroscopy can be used to study the complex influence of disorder on carbon- and MoS_2 samples. One of the strongest attributes of resonance Raman scattering is the ability to correlate electronic structure with phonon excitation, thereby "picking out" individual structures that have both characteristic phonon frequencies and electronic band gaps. In fact, resonance Raman spectroscopy was recently used to identify metallic single-walled nanotubes among non-metallic ones[75, 143] by studying the resonance behavior of nanotube ropes near λ_L=6700 Å. Such a technique, using variable λ_L could also be used to study the shift of the absorption band edge in MoS_2 nanoparticles, since this shift should be reflected in the RR spectra. Moreover, resonance Raman studies are currently being used by the Dresselhaus group to extend the research on PPP-based carbons to the UV domain, thereby probing the resonant enhancement of benzenoid modes under disorder[109].

Preliminary calculations on the electronic structure of PPP with and without defects will be presented in Chapter 7. Since the focus of this thesis was to investigate the experimental manifestations of disorder in several systems, much is left to be done theoretically, in order to model some of the complex disordered structures presented here.

Chapter 4

Electron Spin Resonance in Disordered Carbon

4.1 Introduction

This chapter presents the results of Electron Spin Resonance (ESR) measurements of PPP-based carbons as a function of microwave power and measurement temperature, with the goal of establishing a clearer picture of the electronic structure formed near the heat-treatment temperature $T_{HT} \approx 700°C$. As shown in sections 3.4 and 3.6, it is at T_{HT} values near 700°C that the PPP molecule becomes unstable and carbonized by way of dehydrogenation and cross-linking. This process is inherently accompanied by radical formation, which will give rise to robust ESR signals due to the high concentration of unpaired spins. Thus, the ESR technique allowed me to carefully study the structural rearrangement of PPP-based sp^2 carbon clusters through changes in local spin environment. In particular, identification of g-values, ESR peak-to-peak linewidths (ΔH_{pp}) and line heights (I_{pp}) as a function of measurement temperature T and microwave power P_a can help to identify the dominant interactions and the spin species involved (e.g., $\pi-$ or $\sigma-$ type radicals).

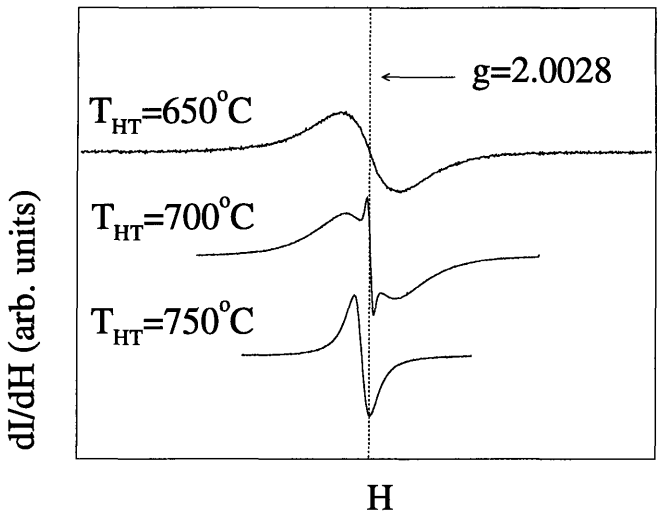

Figure 4-1: ESR traces plotted as dI/dH vs. H for PPP samples heat-treated at low temperatures (650°–750°C), showing the coexistence of two types of spin centers for the T_{HT} ≈700°C trace.

4.2 Experimental Details

ESR measurements were performed on small (∼1 mm diameter) sections of pressed powder samples to allow field penetration within the microwave skin depth ($\delta \sim 1$ cm). Samples were placed in a quartz ESR tube which was evacuated to $\sim 10^{-5}$ torr and sealed with 20 Torr of He exchange gas. ESR spectra were measured using a conventional X-band (∼9.1 GHz) spectrometer with a rectangular TE_{102} microwave cavity within an He cryostat. The magnetic field was calibrated using proton NMR markers. The microwave power P_a was maintained at or below 0.25 mW for all temperature-dependent scans to prevent saturation effects, while power-dependent studies were performed for P_a up to 196 mW.

4.3 Lineshape Analysis

The ESR lineshapes of PPP samples heat-treated to temperatures in the range 650°C $\leq T_{HT} \leq$ 750°C are shown in Figure 4-1, yielding broad (∼5 G) and narrow (∼1 G) linewidth components which are strongly dependent on T_{HT}. Shown also

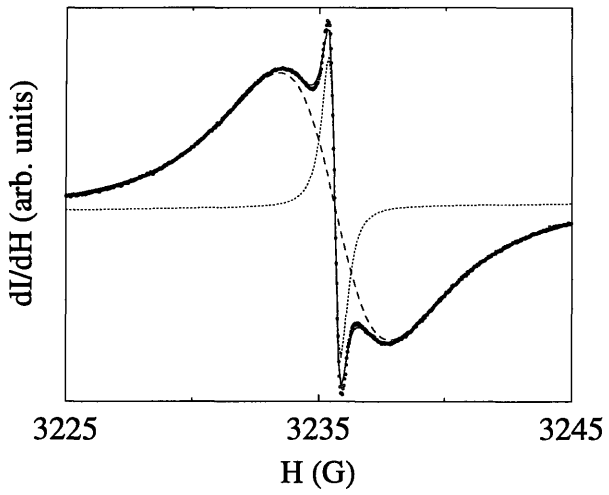

Figure 4-2: ESR trace for sample PPP-700 plotted as dI/dH vs H showing the superposition of a narrow and a broad peak Lorentzian fit.

in the graph is the position of the g-factor $g = 2.0028 = h\nu/\mu_B H$ which was found to be close to the center line for all samples studied (the g-factor for PPP-750 appeared to be slightly higher, as will be seen in section 4.4). Here $h\nu$ is the microwave resonance energy between spin up and spin down states, μ_B is the Bohr magneton and H is the magnetic field. All ESR spectra were fit to first-derivative Lorentzian lineshapes given by

$$Y'^{L}_{(H)} = \frac{16 I_{pp}[(H - H_0)/\frac{1}{2}\Delta H_{pp}]}{\{3 + [(H - H_0)/\frac{1}{2}\Delta H_{pp}]^2\}^2}. \tag{4.1}$$

Here $Y'^{L}_{(H)}$ is given as a function of magnetic field H; resonant field strength (i.e., the center of the absorption line), H_0; the peak-to-peak linewidth, ΔH_{pp}, and the peak-to-peak lineheight, I_{pp}. The resonant field strength is defined as $H_0 = \hbar\omega/g\mu_B$ where ω, g and μ_B are, respectively, the applied microwave frequency, the g-factor and the Bohr magneton. It is useful to define another parameter, the full-outer-linewidth at half-max, $\Delta H_{1/2}$, which is related to ΔH_{pp} as $\Delta H_{1/2}$=2.401ΔH_{pp} for a Lorentzian line shape and as $\Delta H_{1/2}$=1.922ΔH_{pp} for a Gaussian line shape. Thus, ΔH_{pp} and $\Delta H_{1/2}$ could be determined graphically and used to evaluate the relative Gaussian or Lorentzian behavior of the ESR lineshape.

In all our samples the lineshapes all appeared to be completely symmetric and nearly Lorentzian at 80K, with some slight asymmetry appearing at 280K in samples

PPP-700 and PPP-750. This symmetric lineshape is consistent with the idea that these samples are insulating, although small weakly-conducting regions are thought to exist within the carbonized regions for $T_{HT} \geq 700$°C. For the case of more conducting samples, the anomalous skin depth effect causes the lineshape to be Dysonian (asymmetric), which was indeed observed for samples of appreciable size (> 5 mm) with T_{HT} values above 1500°C. Thus, the relatively large skin depths (>20 cm) listed in Table I along with the relatively small values of $\sigma(T)$ below 280K, allow us to ignore any corrections to the ESR data associated with skin depth effects.

The ESR spectra observed for PPP-650, PPP-700 and PPP-750 for all $T_{\rm HT}$ values were fit remarkably well by either a single Lorentzian or the superposition of two Lorentzians. Figure 4-2 shows the superposition of peaks found in the ESR trace of PPP-700, along with Lorentzian fits to the data. From such fits the temperature-dependent g-factor and ΔH_{pp} were determined (see sections 4.4 and 4.5). We note that, although the broad peak corresponding to PPP-650 appeared to be a single Lorentzian, we found that $\Delta H_{1/2}/\Delta H_{pp} \approx 2.3$, which could be explained by a weak Lorentzian line (1.3 G) superimposed upon the main peak of 4.5 G, thereby giving a consistent interpretation for all three lines in Fig. 4-1.

The ratio $\Delta H_{1/2}/\Delta H_{pp}$ was found to be close to 2.4 for all samples studied, indicating that there was little Gaussian behavior in the ESR lineshapes. As will be shown in section 4.6, plots of $1/s$ vs. H_1^2, where s is the saturation factor given by $s = (1+H_1^2\gamma_e^2 T_1 T_2)^{-1}$, showed a non-linear behavior as a function of microwave power ($\propto H_1^2$) for both of these PPP-based samples. Such behavior could arise from spin interactions with an inhomogeneous distribution of localized proton fields (for low-T_{HT}) as well as from interactions with phenyl radicals such as Ph-O or Ph-C-O.

4.4 g-factor

The temperature dependence of the g-factor for low-T_{HT} PPP-based samples is shown in Fig. 4-3. For all temperatures, each ESR spectrum was fit and the center field, H_0, was determined, yielding the g-factor calculated via $g = h\nu/\mu_B H_0$. The results show

Table 4.1: Peak-to-peak linewidth ΔH_{pp}, ratio of the outer-full-width at half-max to the peak-to-peak width $\Delta H_{1/2}/\Delta H_{pp}$, the anisotropy ratio A/B, and skin depth δ at 9.1 GHz at 80 K and 280 K, for PPP heat treated at various temperatures $T_{\rm HT}$.

Sample	ΔH_{pp} (G)		$\Delta H_{1/2}/\Delta H_{pp}$		A/B		δ (cm)	
	80 K	280 K	80 K	280 K	80 K	280 K	80 K	280 K
PPP-650	5.00	4.89	2.35	2.33	1.000	1.008	$> 10^4$	$> 10^4$
PPP-700B	4.21	3.82	2.51	2.52	1.000	1.016	1700	22.1
PPP-750	1.34	2.05	2.52	2.54	1.008	1.015	680	28.2

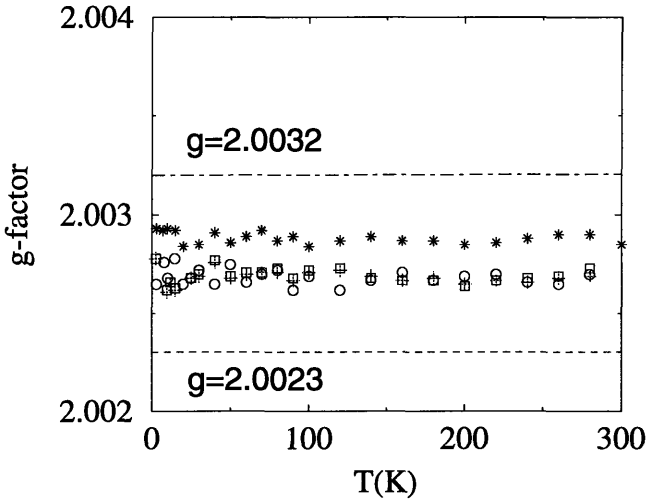

Figure 4-3: Values for the g-factor plotted as a function of temperature for both the narrow and broad ESR peaks observed in various PPP samples. Shown are results for samples PPP-650 (○), PPP-700-broad (+), PPP-700-narrow (□) and PPP-750 (∗). The dot-dashed line indicates the position of published g-values for pristine PPP, while the dashed line represents the position of the free electron g-value.

that the g-factor is essentially temperature independent and falls between published values of g=2.0032 for pristine PPP[94, 98] and g=2.0023 for the free electron value, consistent with observations in many disordered carbon systems[100, 164, 177]. The g-factors for PPP-650 and PPP-700 fall at 2.0027±0.0001, while that of PPP-750 lies at 2.0029±0.0001.

Since σ-electron radicals typically possess g-values considerably less than g_{free}[49, 93], we consider the spin centers in the present case to be associated with π-electrons. Lerner[98], who did early ESR studies of the pyrolysis of Kovacic PPP, found that, for T_{HT} up to 550°C, the g-value was observed to decrease continuously from 2.0032±0.0003

for unpyrolyzed samples to 2.0020±0.0003 for samples with T_{HT} between 550°C and 700°C. Our results for T_{HT} ≤700°C agree with the general behavior of Δg previously observed[98], but the g-value of PPP-750 shows a slight increase over that for PPP-700. Since very little polymer is expected to remain in this heat-treated sample, the g-value for PPP-750 can be explained by contributions from weakly conducting graphene regions which are formed above the critical heat-treatment temperature of 700°C. We thus expect spin centers to be either fully localized (yielding a large Curie component to χ) or partially conducting (giving a small Pauli component). If we denote the g-value of the former as g_{loc} and the latter by g_{cond}, we can write[125] for the total observed g_{obs}

$$g_{\rm obs} = \frac{g_{loc}\chi_{loc} + g_{cond}\chi_{cond}}{\chi_{loc} + \chi_{cond}} \tag{4.2}$$

where χ_{loc} and χ_{cond} are the susceptibilities for localized spins and weakly conducting spin carriers, respectively. From the measured $\chi(T)$ data, we see that the χ_{loc} term easily dominates, but a small increase in $g_{\rm obs}$ would be expected, due to Pauli paramagnetic contributions in prematurely formed graphene segments given by $\chi_{cond} \approx \mu_B^2 N(E_F)$. Therefore, at the onset of graphene segment formation, a small increase in g could be expected.

4.5 Temperature-dependent Linewidth

Figures 4-4 and 4-5 show the temperature dependence of ΔH_{pp} for the broad and narrow peaks, respectively, for all samples studied. The temperature dependence of ΔH_{pp} for the broad peaks observed in Fig. 4-4 for samples PPP-650 and PPP-700 follow mutually similar behavior with ΔH_{pp} increasing with decreasing temperature roughly as $1/T$. In contrast, the temperature dependences of the narrow peaks (see Fig. 4-5) observed in PPP-700 and PPP-750 are quite different. Although the ∼ 0.5G peak of PPP-700 shows a very weak increase of ΔH_{pp} with decreasing T, the linewidth of the ESR spectra of PPP-750 *increases* with increasing T. Moreover, at low measurement temperatures, ΔH_{pp} for PPP-750 approaches a constant value of ∼ 1.2G but peaks at ∼ 2.3G at higher temperatures as shown in Fig. 4-5.

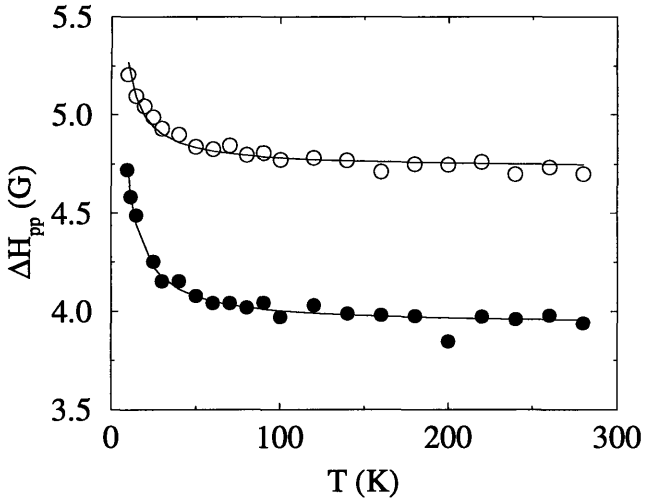

Figure 4-4: The temperature dependence of the linewidth for the broad ($\Delta H_{pp} \sim 5\ G$) ESR peak observed in samples PPP-650 and PPP-700. The solid lines are theoretical curves for a 1D diffusional narrowing model, which are fitted to the data.

4.5.1 Precarbonized PPP ($T_{HT} \leq 700°C$)

For the case of the broad peak observed in the ESR traces of PPP-650 and PPP-700 (see Fig. 4-4), presumably originating from spin centers located within polymeric or hydrogen-rich regions, Lerner[98] proposed a mechanism by which a σ radical produced on a PPP chain might be stabilized, since such a structure is expected to decay (see Fig. 4-6). Before an extended carbon structure forms as a result of full dehydrogenation, an intermediate structure with polymeric characteristics is thought to form, which essentially exchanges the σ radical for a partially delocalized π radical[98]. This reaction would involve evolution of hydrogen at pyrolyzing temperatures, and is shown schematically in Fig. 4-6. A similar structure was also proposed to explain the Raman spectrum of heat-treated PPP in the carbonization crossover temperature regime[113]. Such a mechanism would tend to create unpaired spins in aromatic regions and thereby supports the existence of a proton hyperfine interaction.

Interestingly, although an increase in radical concentration is observed in PPP-based samples with increasing T_{HT}, it is well known that the pristine polymer (no heat treatment) possesses spin centers capable of producing an ESR signal[55, 79, 94, 98, 122, 139]. In fact, the origin of this spin center remains an open question,

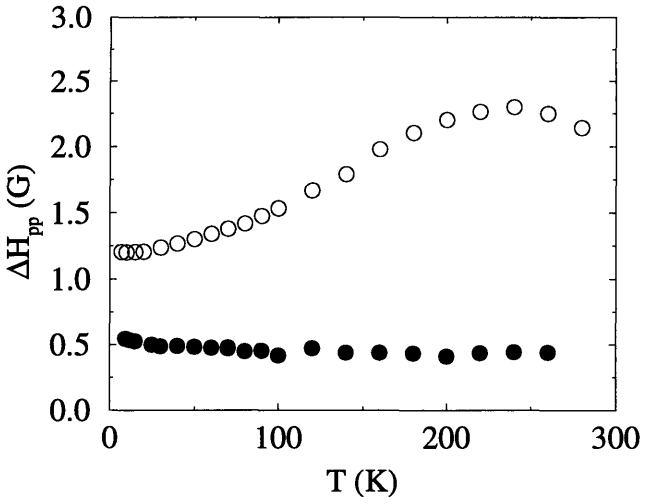

Figure 4-5: The temperature dependence of ΔH_{pp} for the narrow ($\Delta H_{pp} \sim 1\ G$) ESR peak observed in samples PPP-700 (•) and PPP-750 (○) with solid lines to guide the eye.

although some models have been proposed to try to explain the presence of spins in a molecular structure which has a spinless ground state[55, 94]. Although the temperature dependence of ΔH_{pp} for pristine PPP was not measured in the present thesis, we note that the room temperature value and temperature dependence for ΔH_{pp} for the heat-treated samples (see Fig. 4-4) is very close to that observed by Kuivalainen *et al. et al.*[94] and Peo *et al.*[139] for pristine PPP, but contrasts with the linewidth behavior of pristine PPP observed by Kispert *et al.*[79]. On this basis, we interpret the origin of the ~5 G ESR peak in the present study to be of the same nature as the ~5 G ESR peak observed in pristine Kovacic PPP.

Moreover, because the hydrogen content of low-T_{HT} samples is appreciable even up to $T_{HT} = 700°C$, an unresolved proton hyperfine interaction with trapped polarons or localized spins in small polymeric regions could be chiefly responsible for the broadening mechanism for such ESR peaks. We note further that, since polaronic structures involve a localized quinoid state (see inset to Fig. 3-13), the interpretation of defect-induced spin states would be consistent with the observation of quinoid modes in the Raman spectrum discussed in section 3.4.

With this in mind, we now turn to the temperature dependence of the broad

peak observed for PPP-650 and PPP-700. From the previous argument, it seems reasonable that this peak should be related to the hyperfine interaction, which should be completely unresolved because of disorder. Furthermore, since an unresolved hyperfine interaction is expected to bring about a Gaussian lineshape as opposed to a Lorentzian lineshape, we suspect a narrowing process due to exchange or motional narrowing. For the case of exchange narrowing, Anderson and Weiss proposed that the limiting linewidth dependence would be given by

$$\Delta H_{pp}^{exch} = \frac{2}{\sqrt{3}} \left(\frac{\Delta H_0^2}{H_e} \right) \tag{4.3}$$

where ΔH_{pp}^{exch}, ΔH_0, and H_e are, respectively, the exchange-narrowed line, the original prenarrowed line width and the exchange field. Generally, the influence of exchange is proportional to the exchange integral, J, or following Anderson and Weiss we have[6]

$$H_e = 2.83 \left(\frac{J}{g\mu_B} \right) [S(S+1)]^{1/2}. \tag{4.4}$$

However, from $\chi(T)$ measurements of samples PPP-650 and PPP-700, we find an upper bound on the exchange field, since the Weiss molecular field temperatures were all on the order of $\theta \approx$1K or less, resulting in $H_e \sim 3 \times 10^4$ G which would give hyperfine the splittings on the order of $\Delta H_0 \approx 400$ G. For pyrolyzed aromatic structures[101], however, splittings are usually on the order of 10-20 G which is significantly lower than the exchange limit estimate. We therefore do not consider exchange to be important in our systems. Previous measurements of the spin concentration of defective PPP[98] versus the ESR second moment have shown the same result. However, for the case of motional narrowing, Soos[167] derived a form for the case of charge defects diffusing along a one-dimensional path in the presence of an unresolved hyperfine interaction. This approach seems particularly applicable, since we are taking the model of a spin center located on or near a PPP segment which is partially mobile as a polaronic defect slowly diffusing along the PPP chain. The resulting frequency linewidth at low

temperatures, which results in a Lorentzian lineshape, is given by[167]

$$2\omega_{obs}^3\omega_j = \beta\omega_p^4 \tag{4.5}$$

where ω_{obs}, ω_j and ω_p are the observed frequency linewidth, jumping frequency and prenarrowed linewidth. β is a constant less than or equal to 0.2 for a Lorentzian lineshape, and is defined in ref. [167]. Converting the above relation to magnetic field, we have for the linewidth, ΔH_{pp}^{mot} due to motional narrowing of an unresolved hyperfine split line, ΔH_{hf}

$$\Delta H_{pp}^{mot} = \Delta H_{hf}^{4/3}\left(\frac{\beta g\mu_B}{2\hbar\omega_j}\right)^{1/3}. \tag{4.6}$$

Typically, radicals formed from the pyrolysis of aromatic hydrocarbons have hyperfine structures that are $\Delta H_{hf} \sim 10$ G wide[101], and, if we assume that the hopping behavior of the polaronic defect goes roughly as

$$\omega_j(T) \sim \omega_j(\infty)e^{-\Delta E/k_BT} \tag{4.7}$$

where ΔE is the characteristic polaron hopping energy, we get room temperature jumping rates for the broad peak in PPP-650 and PPP-700 close to 10^8 sec^{-1}. From Fig. 4-4 we see that an increase in linewidth can be explained by such motional narrowing, where the solid lines in the figure are fits to Eq. 4.6, yielding hopping energies $\Delta E = 0.83$ and 1.4 meV for PPP-650 and PPP-700, respectively, for a constant unresolved hyperfine envelope ΔH_{hf}. Although an increase in ΔE might be explained by an increase in polaron binding due to trapping by charged defects, we note that ΔH_{hf} for PPP-700 is probably less than that of PPP-650 since the hyperfine splitting goes as the overlap of the resonance spin wavefunction and the hydrogen nuclei (the total hydrogen content is decreasing with increasing T_{HT}). Thus, at this level of analysis, we cannot separate out the changes in polaron trapping from the changes in the overall hyperfine coupling.

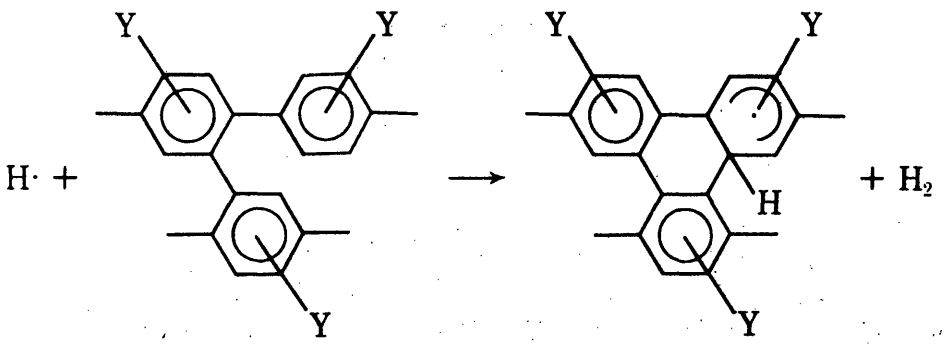

Figure 4-6: Proposed mechanism producing a stabilized spin delocalized about a polymer-like structure, from ref. [98]. The "Y" indicates the linkage of the phenyl group with another phenyl or a hydrogen atom. As shown in the figure, a unstable (liberated) H atom would induce cross-linking and thereby form a more stable H_2 molecule which diffuses away leaving a partially condensed aromatic structure plus a radical.

4.5.2 Carbonized PPP ($T_{HT} > 700°C$)

Considering now the narrow peak appearing primarily in samples PPP-700 and PPP-750, as stated earlier, the narrow peak seems to be the narrowest for the PPP-700 sample. That is, as we go from PPP-650 to PPP-750, a minimum in ΔH_{pp} is observed for PPP-700. This was also observed by Mrozowski[127] for a variety of starting precursors and was correlated with a maximum in the measured spin density $N_{\rm loc}$ at $T_{HT} = 720°C$. Although exchange narrowing was ruled out for the case of the broad PPP-derived peak discussed in section 4.5.1, a narrowing of the ~1 G peak might be expected via the exchange interaction, which is enhanced by an increase in spin density (see section 6.3). If one takes into account an exchange-coupled pair model with a *distribution* of J values[22], larger exchange fields become possible thereby increasing the importance of the exchange interaction. More recently, Tanaka *et al.*[176, 177] studied a set of polyacenic semiconductors (PACs) which also showed a minimum in linewidth for $T_{HT} = 680°C$, and these authors argued that exchange was the dominant narrowing mechanism over a wide measurement temperature range, again because of the large value of $N_{\rm loc}$.

In terms of the temperature dependence of the ~ 1 G peak observed in the ESR spectra of PPP-700 and PPP-750, Fig. 4-5 shows that ΔH_{pp} is flat over a large range

of T with a small increase at low temperatures for PPP-700, while PPP-750 shows an anomalous behavior with a decrease in ΔH_{pp} with decreasing temperature and saturation as $T \rightarrow 0$. For the case of PACs[177], it was suggested that the latter behavior could be due to a Korringa-type[83] spin-lattice T_1 temperature dependence ($T_1 \sim 1/T$), although no clear structural model allowing for such an interaction was given. In fact, the Korringa relation was first used to describe the NMR Knight shift observed in metals and can be derived in a straight forward way using standard statistical mechanical techniques[166]. By modifying the Korringa formula to describe a resonant spin that is motionally narrowed by hopping, I derive an expression for the linewidth, ΔH_{pp}:

$$\Delta H_{pp} = \Delta H_{pp}^{K} \frac{\omega \tau_R}{1 + \omega^2 \tau_R^2} \tag{4.8}$$

where $\Delta H_{pp}^{K} = A_K T$ describes the Korringa broadening with increasing temperature, ω is the microwave frequency (=9.1 GHz), and τ_R is the hopping time that can be inferred from conductivity measurements (see section 5.3) which give the hopping rate in terms of a variable range hopping (VRH) mechanism as

$$\tau_R^{-1} = \nu_{hop} = \nu_0 \exp\left[-\left(\frac{T_0}{T}\right)^{1/4}\right]. \tag{4.9}$$

In the above expression, ν_0 is the phonon assisted hopping rate taken as $\nu_0 \sim 10^{13} - 10^{14}$ sec^{-1} and T_0 is the VRH characteristic temperature and is on the order of 10^6 K. If we take $A_K \sim 0.01$ and $T_0 \sim 8.1 \times 10^5$ K, reasonable agreement is found with experiment (see theoretical curve in Fig. 4-7), although this value of T_0 is closer to that found for PPP-800 in section 5.3. Nonetheless, considering that the samples are quite inhomogeneous and that different size samples were used in the ESR and $\sigma(T)$ studies, the current theory depicts the general features of Fig. 4-7 qualitatively well.

The physics of the Korringa relation lies in the fact that the resonant spin in question is interacting with a population of degenerate electrons which, for the case of metals, are abundant. In disordered carbons, the state of the bulk system can hardly be considered metallic. However, if we consider that small carbonized regions must form in PPP-750 to take into account the observed H/C content and the Raman

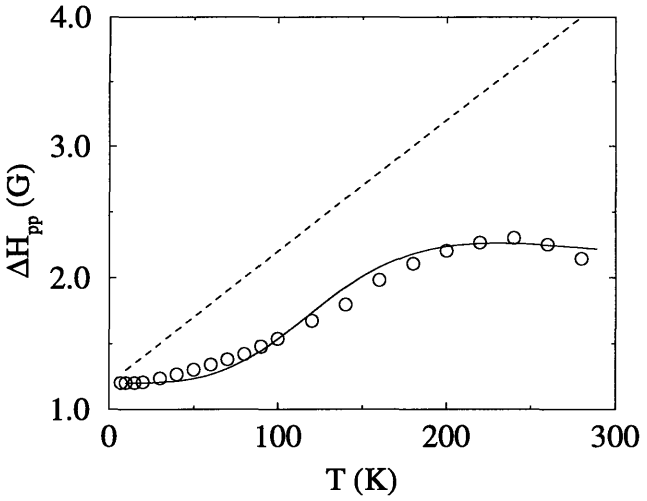

Figure 4-7: The temperature dependence of ΔH_{pp} for PPP-750 plotted along with theoretical curves of a motionally-narrowed Korringa interaction (solid line) and the same Korringa interaction in the absence of motional narrowing (dashed line).

spectrum (for example), the resulting π orbitals would form degenerate levels that could be partially emptied by way of defect traps. Thus, near a carbon clusters, electronic states look metallic so that a spin localized near a carbon cluster can interact with degenerate electronic states by way of a Korringa interaction. Moreover, as will be shown in section 5.3, these carbon clusters are what form localization sites for hopping conduction in disordered PPP-based samples. If the resonant spin hops from one localization site to the next, motional narrowing effects will tend to decrease ΔH_{pp} as T increases, so that the peak near ~250 K in Fig. 4-7 can be considered a cross-over from an pre-narrowed Korringa interaction to a narrowed one.

4.6 Room Temperature Power Dependence Studies

In order to probe the relaxation mechanisms and characteristic relaxation times of PPP-based samples over a wider T_{HT} range, room temperature ESR spectra were taken of samples heat-treated from 650°C to 2900°C[116]. Again, special attention was given to the heat-treatment range 650°C - 750°C so as to carefully study the

Table 4.2: Summary of ESR parameters (the spin-lattice relaxation time T_1, the spin-spin relaxation time T_2, the g-factor g, and the density of localized spins $N_{\rm loc}$) for the samples studied[116].

Sample	T_1 (x10^{-5} s)	T_2' (x10^{-7} s)	g	$N_{\rm loc}$ (x10^{19} g^{-1})
PPP-650	1.51	0.52	2.00270	3.18
PPP-700	1.46	1.20	2.00277	4.93
PPP-750	0.84	1.61	2.00278	5.73
PPP-800	1.24	1.21	2.00277	5.67
PPP-1000	1.27	1.15	2.00274	2.70
PPP-1500	0.81	1.09	2.00274	0.637
PPP-2900	0.44	1.24	2.00278	0.095

physics of carbonization and probe defect structures formed in sample PPP-700. In terms of lineshape, the ESR traces for samples with T_{HT} values from 750°C to 2900°C showed little qualitative difference, whereas large changes in the ESR spectra were observed for heat-treatment temperatures between 650°C and 750°C (see Fig. 4-1).

In order to characterize the relaxation processes of the spins responsible for the two apparently different ESR peaks, careful saturation measurements were performed on all samples using power levels up to 196 mW (see Fig. 4-8). For each sample, at a given value of P_a, the line-shape was fit reasonably well to first-derivative Lorentzian lineshapes, which is the result expected from homogeneously broadened ESR lines. Furthermore, a plot of line-width vs. the microwave field strength, H_1, which is proportional to $\sqrt{P_a}$, where P_a is the incident microwave power, was made for each sample and the plot indicated that ΔH_{pp} increases linearly with H_1, giving evidence that the dominant broadening mechanism appeared to be of the homogeneous type. However, some deviation from homogeneous behavior was observed for the broad peak of precarbonized PPP samples ($T_{HT} \leq 700$°C). Therefore, we cautiously approximate the broadening mechanism of each peak as being of the homogeneous type, although we expect some inhomogeneous contributions.

Assuming that Bloch's phenomenological treatment of relaxation times is valid, we can estimate relaxation times by first evaluating the inverse line-width parameter

given by

$$T_2 = \frac{2}{3^{1/2}\gamma_e \Delta H_{pp}^0} \tag{4.10}$$

where $\Delta H_{pp}{}^0$ is the asymptotic zero power line-width and γ_e is the gyromagnetic ratio, $\gamma_e = g\mu_B/\hbar$. The spin-spin (T_2') and spin-lattice (T_1) relaxation times can then be related to the inverse linewidth parameter as

$$\frac{1}{T_2} = \frac{1}{T_2'} + \frac{1}{2T_1}. \tag{4.11}$$

Least-square fits were performed of all data yielding values for ΔH_{pp}^0 and the peak-to-peak line height, I_{pp}. By comparing the saturation behavior of our samples with a standard of diphenyl picryl hydrazyl (DPPH), estimates of T_1 and T_2 could be made. In making these estimates, we assume that $T_1 \gg T_2$ so that the spin-spin relaxation time, T_2', is approximately equal to T_2. Values for T_2', T_1 and g are given in Table 4.2 along with values for the localized spin density, $N_{\rm loc}$ as determined by a Curie-Weiss fit to magnetic susceptibility data (see section 6.3). Although a Lorentzian type lineshape was determined to fit all of the data quite convincingly, the saturation behavior for low-T_{HT} samples showed some resemblance of that arising from inhomogeneously broadened lines. For a homogeneously broadened line, we expect the saturation factor given by

$$s = \frac{1}{1 + {H_1}^2 \gamma^2 T_1 T_2} \tag{4.12}$$

to have an inverse dependence on microwave power ($P_a \sim H_1^2$) for ${H_1}^2 {\gamma_e}^2 T_1 T_2 \gg 1$. In Fig. 4-8 we plot the inverse saturation factor, which is experimentally determined from

$$\frac{1}{s} = \left[\frac{\lim_{H_1 \to 0}(I_{pp}/H_1)}{I_{pp}/H_1}\right]^{2/3}. \tag{4.13}$$

From the plots in Fig. 4-8 we can see a substantial deviation from a linear dependence for the case of peak A implying non-homogeneous contributions.

The ESR spectra and associated relaxation mechanisms of disordered carbons have been investigated previously for various precursors[100, 128, 129]. Due to the

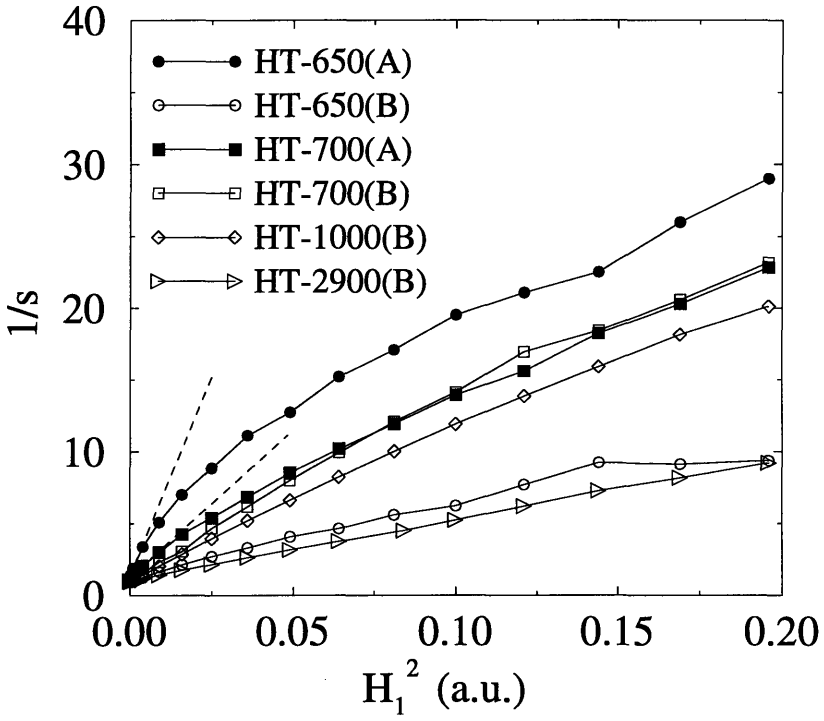

Figure 4-8: Plot of inverse saturation factor 1/s vs. H_1^2 where H_1 is the microwave magnetic field magnitude for several samples, showing the inhomogeneous broadening behavior of peak A (broad peak). Peak B (narrow peak), however, exhibits a roughly linear dependence in power, implying a mostly homogeneous broadening mechanism.

large changes of electrical properties brought about by carbonization at low T_{HT} ($\sim$700°C), the corresponding ESR signal changes rapidly for small changes in T_{HT}. At higher T_{HT} ($\gtrsim$2000°C), graphitization can occur, introducing further change in the ESR signal, usually due to interactions of the spins with conduction electrons. Since PPP forms a hard carbon through heat-treatment[115], we expect the effect of heat-treatment above 2000°C on the ESR signal to be less pronounced than for most of the carbons studied by Singer[164]. Therefore, in our study of PPP heat-treated above 650°C, we consider two distinct T_{HT} regimes separately, namely 650°C - 800°C and 800°C - 2900°C.

The ESR spectra of PPP for $T_{HT} > 800$°C, where only the narrow peak is observed, can be compared to that of other disordered carbons. The origin of the unpaired spins in these materials has been attributed to dangling σ-bonds (or terminating radicals) at the edges of the sp^2 carbon networks[36]. However, prior to evacuation of the quartz tube sample chamber, the PPP samples were exposed to air for extended periods of time allowing molecules such as H_2O, CO_2, etc., to enter the pores of the sample and to react with these highly reactive dangling bonds. Although attempts to evacuate the sample pores most likely removed most of the physisorbed agents from within the micropores of the samples, chemically-bonded -OH, -O, -CO and =CO probably remained at significant concentrations, forming ESR radicals. In the case of unpaired spins localized on odd-numbered carbon atom clusters, Yoshizawa[193] *et al.* suggested that molecular orbitals (MOs) would form, leaving the highest energy electron unpaired, and available to participate in spin resonance. Since small carbon clusters are expected to form in carbonized PPP, the resulting unpaired spins could dominate the ESR spectrum.

Dipolar interactions are important in many spin systems, causing a broadening in ESR line widths which goes as $\Delta H_{pp} \sim \mu_B / r^3$, where r is the distance between spins. Since r^3 scales as $1/N_{\rm loc}$, we would expect a narrowing of ΔH_{pp} (or an increase in T_2) with increasing T_{HT} (see Table I). This effect is not observed since T_2 for the narrow peak varies only slightly from 650°C to 2900°C, and in fact, T_2 for decreases between 750°C and 1500°C. For example, $N_{\rm loc}$ drops by almost a factor of 10 as

we go from PPP-800 to PPP-1500, corresponding to $\Delta H_{dipolar}$ going from 1 G to 0.1 G, while ΔH_{pp} for the narrow peak remains quite close to 0.5 G for the entire T_{HT} range. However, such an analysis of the measurement temperature independent dipolar interaction becomes complicated by the fact that the motional narrowing of linewidths is expected to increase with increasing electrical conductivity.

Since the hydrogen content of low-T_{HT} samples is appreciable in PPP-like regions, an unresolved proton hyperfine interaction with trapped polarons could be chiefly responsible for the inhomogeneous broadening mechanism for the precarbonized $\sim$5 G peak. We note further that, since polaronic structures involve a quinoid state, the interpretation of defect-induced spin states would be consistent with the observation of quinoid modes in the Raman spectrum.

The enhanced ability of sample PPP-700 to accommodate Li may then be linked not only to structural characteristics as previously discussed in chapter 3, but also to the creation of bipolaron states along disordered PPP segments. Thus, Li may be localized not only within carbonized regions between weakly correlated graphene ribbons as for purely carbon-based Li-C systems, but also within the uncarbonized regions which contain a mixture of benzenoid and quinoid PPP capable of supporting bipolaronic states. This postulate may then be connected with a previous ^{7}Li NMR experiment which identified two types of Li localization centers within PPP-700 samples[156]. Although Li dimers or clusters may well exist in these systems, the possibility of an 'ionic' site belonging to Li localized within the carbonized regions and a 'covalent' site belonging to Li localized near small PPP-like segments may also also explain such NMR results.

4.7 Future Work

The experimental data presented in the current chapter resulted from a one month visit to the Tokyo Institute of Technology and the work was done in collaboration with Professor T. Enoki. Therefore, only a limited amount of run time was possible for a limited sample set, and hence, much remains to be investigated following our

preliminary ESR investigations of PPP-based carbons. Future work on PPP-based carbons should focus on understanding the mobile polaronic states which bring about motional narrowing, and a more thorough understanding of carbonization of aromatic polymers. The two ΔH_{pp} values (narrow and broad) observed in the ESR spectra of PPP-700 may be due to two spin centers which interact with one another. The present study does not address this issue. However, spin echo experiments could be used to study the influence of the presence one spin on the other's relaxation mechanism. This would yield information regarding the polymeric and carbonized domain sizes in low-T_{HT} polymer-based carbons. Moreover, since both of these spins are expected to interact with ^{13}C nuclei, magic angle spinning (MAS) NMR experiments could monitor this interaction and corroborate the anomalous temperature dependent behavior of ΔH_{pp} for PPP-750.

Chapter 5

Electronic Transport

5.1 Introduction

The electronic transport of crystalline materials is invariably linked to the electronic properties of Bloch wavefunctions under a given crystal symmetry. In the case of disordered materials, however, translational symmetry is lost and the wavevector "k" is no longer a "good" quantum number (i.e., Bloch wavefunctions no longer adequately describe the electronic states near the Fermi level E_F). Anderson first proposed a formalism for treating the electronic states of disordered or "granular" materials and showed that disorder in the form of a modulated periodic potential induces localized states near the Fermi level [5, 124]. Although the electronic band structure of disordered systems is not well defined due to symmetry loss, the density of states (DOS) can still be defined such that different energies correspond to localized or extended states [74, 124]. If localized states exist at E_F, a "mobility" gap forms, separating the filled valence states and the extended conduction states.

In this chapter, I model the more disordered carbons examined in this thesis (PPP-based carbons and ACFs) as being granular disordered composites made up of small "crystallites" of graphitic carbon (see Fig. 5-1). Conduction then takes place by way of phonon-assisted tunneling or "hopping" between weakly connected graphitic crystallites which form carrier "localization" sites. The finite dimensions of the carbon crystallites is thus probed by examining the so-called localization length (ξ), average

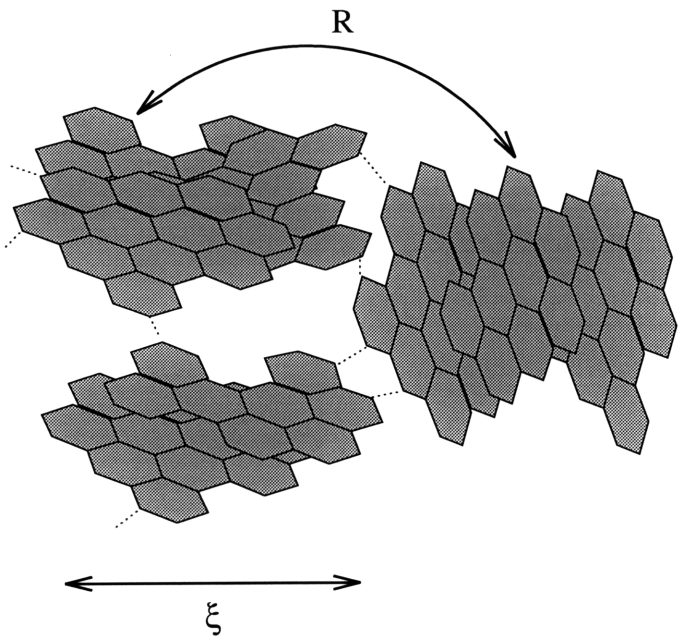

Figure 5-1: Schematic of the hopping-grain model for disordered carbons showing the effective localization length, ξ, and the hopping distance R as discussed in the text.

hopping distance(R), and the density of states at the Fermi level ($N(E_F)$), as defined in Mott's theory for conduction in non-crystalline solids [124].

The formalism of Mott describes the conduction behavior of various semiconductors, and other disordered materials, in the moderate temperature range of $77 < T < 300$K. At low temperatures, however, as the deBroglie wavelength of the carriers grows, intra-grain scattering can strongly affect the carrier transport in the form of quantum coherent backscattering and electron-electron interactions. The last section of this chapter considers such effects for the case of ACF samples, where I use low temperature, high magnetic field transport experiments as the primary probe. (Unfortunately, further high field experiments on other carbon samples were prevented by the closing of the Francis Bitter National Magnet Laboratory in 1995.)

5.1.1 Electronic States in Disordered Carbons

In well-ordered graphite, the $E(\mathbf{k})$ relations can be found by considering the overlap of σ- and π- orbitals arranged in a honeycomb lattice using a variety of techniques [170]. The resulting density of states is presented in Fig. 5-2 showing the behavior of

states near the Fermi level. For slightly more disordered graphite materials in which the stacking is "turbostratic", a 2D structure is appropriate, leading to a zero-gap dispersion and no overlap of conduction and valence states (see Fig. 5-2(c)). With increasing disorder, translational symmetry is destroyed resulting in k no longer being a "good" quantum number. However, the general structure of the DOS can still be considered, with modifications as suggested by Mott [124]. Thus, the π states near the Fermi level are expected to become localized with a mobility gap forming, as shown in Fig. 5-3, due to the disordered graphitic crystallite structure . Carriers occupying the localized states at the Fermi level must tunnel or "hop" from one localization site to another (see Fig. 5-1), where the nearest localization site may not be the most favorable site in terms of energy. Thus, a variable-range form of hopping occurs in highly disordered systems, such as low-T_{HT} PPP, and this is discussed in the next section.

5.2 Experimental Details

DC transport measurements were done using the standard four-point probe technique, applying a constant current supplied by a Keithley 220 Programmable Current Source and measuring the voltage across the sample with a Keithley 182 Sensitive Digital Voltmeter. The resistance, $\mathcal{R}$, was thus measured, allowing the evaluation of the resistivity as $\rho = \mathcal{R}(A/\ell)$ where A is the cross sectional area of the sample and ℓ is its length. I assume an isotropic bulk conductivity tensor, so that the conductivity is simply $\sigma = \rho^{-1}$. At all times the total power supplied to the fibers was less than 0.1 μW in order to prevent thermal damage (or annealing) due to ohmic heating. The temperature was monitored using sensitive carbon-glass resistors and was controlled using a Lakeshore DRC-93CA Temperature Controller. All samples were cooled using standard cryogenics techniques (a Janis dewar was used as the cryostat), and then slowly heated using a resistance heater. The heating rate did not exceed 10-100mK/min below 100K and 100-1000mK/min above 100K. For magnetoresistance (MR) measurements, the same equipment was used, with the addition of a high-field

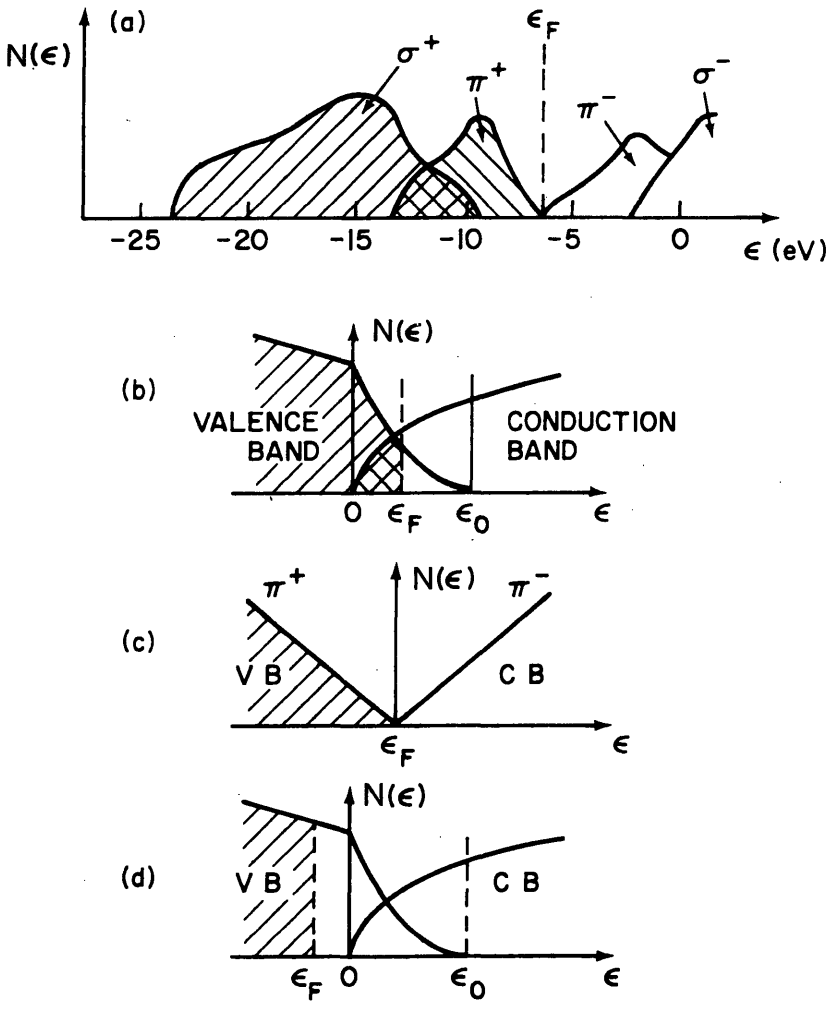

Figure 5-2: Density of states $N(E)$ in graphite: σ and π states over a broad energy range (a), the π-band overlap found from the Slonczewski-Weiss-McClure model (b), the zero-gap structure for a single graphene sheet (c), and the effect of electron traps or acceptors (d) [171].

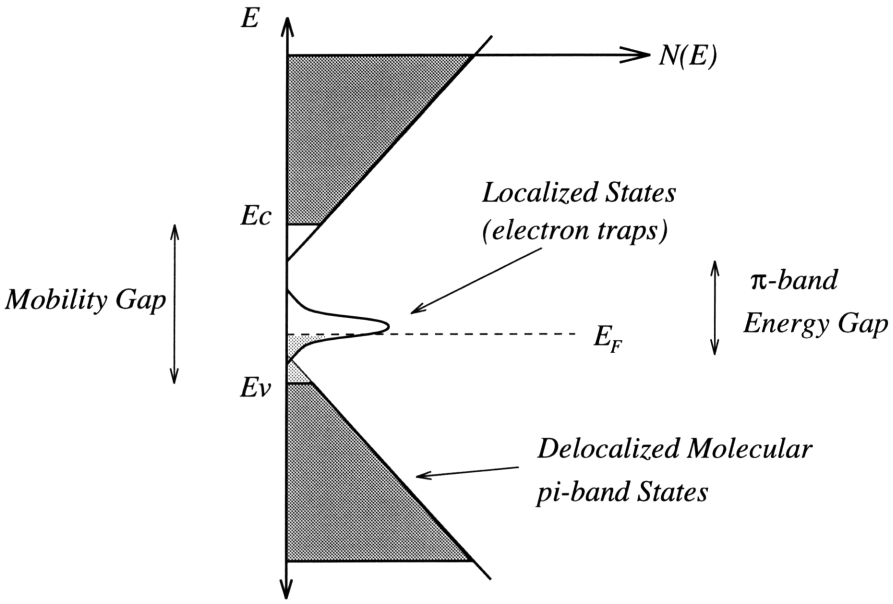

Figure 5-3: Schematic of localized states near the Fermi level for disordered aromatic (π-bonded) systems. In the figure, the dark shaded regions represent conduction and valence bands that can support extended electron and hole states, respectively. In the presence of disorder, however, carriers near the Fermi level become trapped (light shaded area) due to the appearance of localized states (the peak in Fig. 8-3). Since localized and extended states can not coexist, a so called mobility gap forms between delocalized valence band states at E_v and conduction band states at E_c.

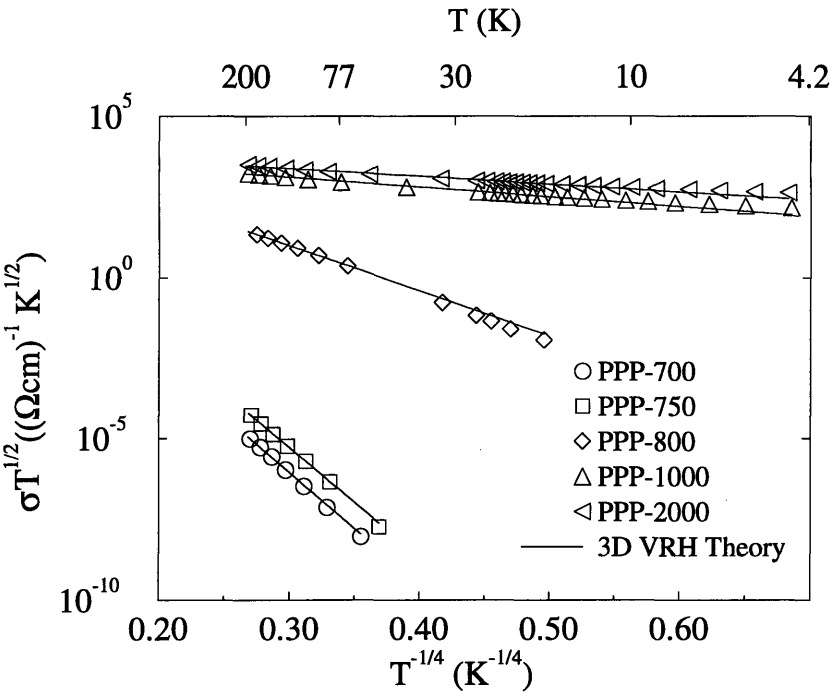

Figure 5-4: Semi-log plot of the DC conductivity $\sigma(T)$ plotted as $\sigma\sqrt{T}$ vs. $T^{-1/4}$ for PPP-based samples heat-treated to temperatures between 700 and 2000°C, along with fits to Mott's variable range hopping (VRH) model (see text). Although $\sigma(T)$ data were taken in measurement temperature increments of ~1-2 K, the above graph shows only every tenth data point so that the VRH theoretical curves could be seen (fitting was done using the full data set).

Bitter magnet for scans up to 25 T, which was utilized at the (then) Francis Bitter National Magnet Laboratory. (A superconducting magnet was used for the 11 Tesla conductivity scans.)

5.3 Hopping Conductivity in PPP-based Carbons

DC electrical conductivity measurements were previously performed [115] on PPP-based carbons heat-treated up to 2900°C, where emphasis was placed on the development of graphitic networks in this apparently non-graphitizing material. For T_{HT} above about 1000 °C, the DC electrical transport was generally characterized by a weak semiconducting-type behavior with respect to the stronger temperature dependence observed at lower T_{HT}. At lower T_{HT}, only the PPP-700 sample was investigated, but the results indicated the presence of strongly localized carriers. In order to investigate the highly localized states produced near carbonizing tempera-

tures, we performed a more detailed conductivity study on samples heat-treated in the temperature range (600-800°C) with the hope of elucidating the complex transport mechanisms and studying the manifestations of disorder in this system.

Figure 5-4 shows the results for the temperature dependence of the conductivity of the PPP-based samples below 200 K, plotted on a semi-log plot as $(T)^{1/2}\sigma(T)$ vs. $T^{-1/4}$ (this transformation of σ and T allowed for easier fitting, as will become apparent later). Pertinent materials parameters obtained from the VRH (variable range hopping) model are given in Table 5.1. Due to very high values of $\rho(T)$, samples PPP-700 and PPP-750 could only be measured down to $\sim$ 50 K, while $\rho(T)$ measurements below 20 K were possible on higher T_{HT} samples. Although temperature-dependent conductivity measurements on sample PPP-650 were attempted, the high DC resistance of this sample ($\approx$10 GΩ) prevented accurate measurements below about 250K. In Fig. 5-4, the steeper slopes correspond to a stronger localization of carriers. The conductivity of samples PPP-700, PPP-750 and PPP-800 all followed a roughly $T^{-1/4}$ temperature dependence, while some deviation in the slope of the conductivity of PPP-1000 and PPP-2000 samples was observed.

A more detailed view of the temperature-dependent conductivity of samples PPP-700 and PPP-750 is shown in Fig. 5-5, along with a plot of the room temperature conductivity σ(300K) vs. T_{HT} in increments of ΔT_{HT} = 25°C (shown in the inset). Note that the σ(300K) values of samples PPP-650 and PPP-750 differ by almost 12 orders of magnitude, which underscores the fact that PPP is effectively carbonized above T_{HT} = 650°C. Interestingly, the measurement temperature dependence of $\sigma(T)$ for the two samples studied in this T_{HT} regime (PPP-700 and PPP-750) show a quite similar behavior, despite the fact that their Raman spectra (see Fig. 3-5 of section 3.4.1) and hydrogen content differ considerably.

To explain the transport behavior of PPP-based carbons (particularly at low-T_{HT}) we started with the physical model that heat treated PPP consists of disordered polymer-like segments intermingled with disordered sp^2 carbon regions, or conducting carbon regions embedded in an insulating matrix. To explain the high-resistivity conduction mechanism observed in carbon-polyvinylchloride composites, a fluctuation-

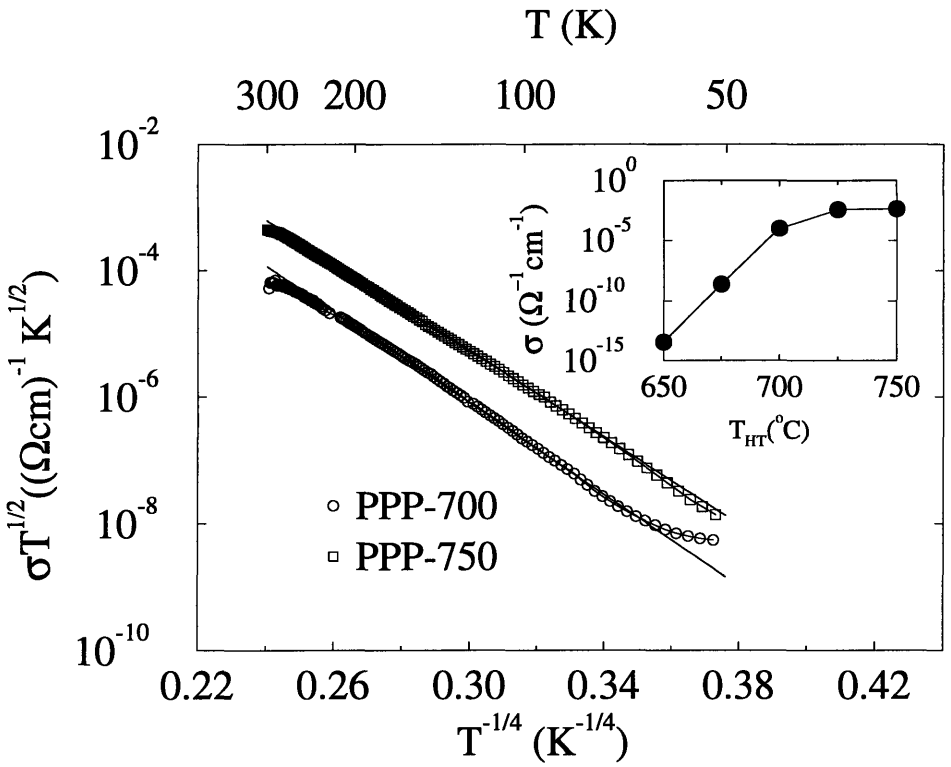

Figure 5-5: DC conductivity plotted as $\ln\sigma\sqrt{T}$ for samples PPP-700 (○) and PPP-750 (□) as a function of $T^{-1/4}$. The inset shows the room temperature (300 K) conductivity for samples heat-treated in the range $650 < T_{HT} < 750$°C.

induced tunneling (FIT) model has been previously used, where the value of the conductivity was below the percolation threshold. [162] This model yields an exponential temperature dependence, $\sigma(T) = \sigma_0 \exp[-T_1/(T + T_0)]$ where T_0 and T_1 are, respectively, the characteristic temperatures related to the tunneling and thermal activation mechanisms. However, for barrier separations between conducting grains on the order of 500 Å (an overestimate for our samples), unreasonable values for the barrier potential (greater than 100 eV) were obtained for PPP-700. Therefore, although the idea that two different regions exist in low-T_{HT} samples is indeed consistent with all other experimental results (Raman, chemical analysis, ESR), which reveal a highly inhomogeneous medium, the FIT mechanism does not dominate the transport behavior.

As shown in the inset of Fig. 5-5, and briefly discussed in [115], room temperature conductivity measurements showed that $\sigma(300K)$ differed by several orders of magnitude between samples whose T_{HT} differed by only tens of degrees Celsius. I thus propose that in terms of a granular conductor-insulator model, PPP-700 lies roughly

Table 5.1: VRH fitting parameters for PPP-700 and PPP-750 samples.

Sample	$\sigma_0(T)\sqrt{T}$ (Ω^{-1}cm^{-1}K$^{1/2}$)	$T_0^{1/4}$ (K$^{1/4}$)	$N(E_F)$ (eV^{-1} cm^{-3})	γ^{-1} ($\AA$)
PPP-700	5.58 $\times 10^4$	83.2	2.4 $\times 10^{24}$	1.2
PPP-750	1.12 $\times 10^5$	79.1	1.8 $\times 10^{25}$	0.67
PPP-800	1.68 $\times 10^5$	32.4	9.9 $\times 10^{24}$	2.7
PPP-1000	1.16 $\times 10^4$	7.0	1.5 $\times 10^{20}$	830
PPP-2000	1.42 $\times 10^4$	6.6	1.8 $\times 10^{20}$	1100

at a "percolation" threshold with regard to the formation of condensed clusters via heat-treatment. That is, at successively higher T_{HT}, there is an increasing tendency for the polymer to dehydrogenate and form percolating C-C bonds between chains, thus forming condensed aromatic clusters on which hopping localization sites may form. This is to be distinguished between an increase in conduction due to percolation *between* carbon clusters, since the main increase to the conductivity in such a model should be attributed to the density of states which increases as the aromatic cluster is formed. In fact, chemical analysis studies of heat-treated PPP show that for PPP-650, -700 and -750 samples, the atomic H/C ratio amounts to 0.53, 0.29 and 0.17, respectively. If we assume that the densities of polymeric and carbonized regions are *roughly* equal, and that the PPP segments are long, a percolation threshold of $(\mathrm{H/C})_t \sim 0.10$ is expected for spherical carbonized regions nucleating in the polymer matrix via thermal dehydrogenation.

A logarithmic plot of $\sigma(T)\sqrt{T}$ vs. $T^{-1/4}$ shown in Fig. 5-5 reveals a temperature dependence indicative of a zero Coulomb gap 3D variable range hopping (VRH) mechanism, as explained below. In this model, carriers are localized at defects or impurities and conduct by way of a thermally assisted tunneling or hopping mechanism. Mott [124] derived a general form for conduction under the VRH mechanism in d-dimensional systems given by

$$\sigma(T) = \sigma_0(T)\exp\left[-\left(\frac{T_0}{T}\right)^{1/p}\right] \tag{5.1}$$

where $p = d + 1 = 4$ for a 3D system. In the presence of a Coulomb gap, the exponent, p, is expected to be equal to 3 for a 3D system [39]. Note that we include the explicit temperature dependence of the conductivity prefactor, $\sigma_0(T)$, derived in Mott's original formulation. The forms of $\sigma_0(T)$ and T_0 are given by [123, 124]

$$\sigma_0(T) = e^2 R^2 \nu_0 N(E_F) \tag{5.2}$$

$$T_0 = \frac{\lambda \gamma^3}{k_B N(E_F)} \tag{5.3}$$

where R is the optimum hopping distance, ν_0 is the hopping rate prefactor, $N(E_F)$ is the density of states at the Fermi level, γ is the inverse decay length and λ is a dimensionless constant equal to about 20 [3, 163]. Since the optimum hopping distance (equal to 4/3 the average hopping distance $\bar{R}$) can be given by $R = [\frac{2}{3}\pi\gamma k_B T N(E_F)]^{-1/4}$, yielding a hopping energy $W = [\frac{3}{4}\pi R^3 N(E_F)]^{-1}$, we can write for $N(E_F)$ and γ as [137]

$$N(E_F) = 1.996 \times 10^{48} \frac{(\sigma_0\sqrt{T})^3\sqrt{T_0}}{\nu_0^3} \tag{5.4}$$

$$\gamma = 2.122 \times 10^{13} \frac{(\sigma_0\sqrt{T})\sqrt{T_0}}{\nu_0}. \tag{5.5}$$

A fit of PPP-based carbon $\sigma(T)$ data to Eq. 5.1 is shown in Fig.5-5 , from which we extract values for $\sigma_0\sqrt{T}$ and T_0 (see Table 5.1). Although values of ν_0 on the order of 10^{16} sec^{-1} have been successfully used in VRH theory and applied in the case of heavily doped PPP [94] and amorphous semiconductors [61], no clear argument exists as to why such high hopping rates should be physical. Therefore, we maintain Mott's original formulation in which $\nu_0 = \nu_{ph}$, the frequency of phonons assisting in hops. Assuming a graphite Debye temperature [78] of $\theta_D \approx 2300$ K (since conduction is assumed to be confined to sp^2 carbonized domains) and the fact that $\theta_D = (h\mathrm{v_k}/k_B)(6\pi^2/N)^{1/3}$ we can estimate the dominant phonon contribution to be $\nu_{ph} \sim 10^{14}$ sec^{-1}. We could also estimate ν_{ph} by the large features in the density of phonon modes of low T_{HT} PPP in the frequency range $10^{13} - 10^{14}$ sec^{-1}, since the

Raman spectra (see Fig. 3-5) of disordered materials generally reflect these features. A value of $\nu_0 \sim 10^{14}$ sec^{-1} was found to yield reasonable values for $N(E_F)$ and γ for PPP-based samples.

5.4 Magnetoresistance of Activated Carbon Fibers

5.4.1 Previous Studies on ACFs

Previous magnetoresistance studies have been done on ACFs heat treated below 1200° C to characterize the granular metallic behavior of these disordered fibers and to identify transport phenomena associated with variable range hopping mechanisms [56]. In these systems, the effective inelastic scattering length, L_i, was found to be limited by the relatively small size of the graphitic carbon clusters. Heat treatment at higher temperatures (above 1200°C) has the effect of extending the 2D graphene sheets, creating larger clusters, and thus allowing for an increase in L_i. Accordingly, for heat treatment temperatures (1200-2500° C), above the metal to insulator transition (MIT), transport behavior was observed to have a distinctly different signature, characterized by a negative magnetoresistance (MR), an absolute increase in the conductivity by two orders of magnitude and a weaker overall temperature dependence. Thus, these experiments have shown that MR can be used to characterize the relative degree of graphitization in ACFs heat treated at various temperatures.

5.4.2 Overview of Conductivity Corrections at low Temperature

For heat treatment temperatures above 2000° C, transport studies of ACFs have shown that weak localization (WL) is the dominant correction to the classical Boltzmann calculation of the conductivity at temperatures up to 300K, despite the percolative nature of transport in pregraphitic fibers [1, 11]. Thus, the turbostratic structure of ACFs provides one of the few systems capable of demonstrating room temperature WL [1]. The WL correction has been calculated for disordered 2D systems and

produces a ln(T) correction to the conductivity and a similar correction as a function of applied H field. Along with WL, however, a second effect was observed in the transport behavior at both very low temperatures and high magnetic fields. For example, intercalated carbon fiber studies showed a complete up-turn in the negative MR at relatively low temperatures [33]. Altshuler et. al [2, 96] found that at very low temperatures, disordered 2D conductors not only suffer corrections to $\sigma(H,T)$ due to WL, but also a correction due to electron-electron interaction (EEI). Although both effects are difficult to separate in zero magnetic field, the application of a relatively low magnetic field is sufficient to distinguish between the two effects [13]. This is due to the very sensitive nature of WL to the phase of the electronic wavefunctions.

In the WL effect, a net enhancement of the backscattering in the -k direction, for a carrier initially traveling with a wave vector k, with respect to all other possible scattering paths in momentum space is caused by the coherence of scattered waves of equal and opposite momentum transfer sequences (see left side of Fig. 5-6). This quantum coherence will, in fact, double the probability of backscattering relative to incoherent processes (see right side of Fig. 5-6) In terms of the magnetoresistance experiments, one may see the effect of a magnetic field on diffusive transport as an Aharanov-Bohm effect producing a net phase difference between the two partial scattered waves that enclose magnetic field lines along symmetric paths from k to -k. A relative phase shift of $2e\phi/\hbar$ is introduced by each unit of magnetic flux through the carrier path loop, thus destroying both the symmetry for time reversal and the net coherence. Hence, a magnetic field provides a useful mechanism for suppressing WL. Furthermore, MR studies have shown that EEI effects are much less field dependent for magnetic fields that are not too high [96]. Thus, both MR studies in relatively low fields and the application of a magnetic field during temperature scans of the conductivity will be dominated mainly by WL effects. EEI effects start to become important at magnetic fields high enough so that the magnetic energy $\mu_B H$ becomes larger than the thermal energy [96]. We then expect to see evidence for EEI effects as the temperature becomes low and the magnetic field becomes high. We can then use magnetic transport studies to probe the presence of other mechanisms that may

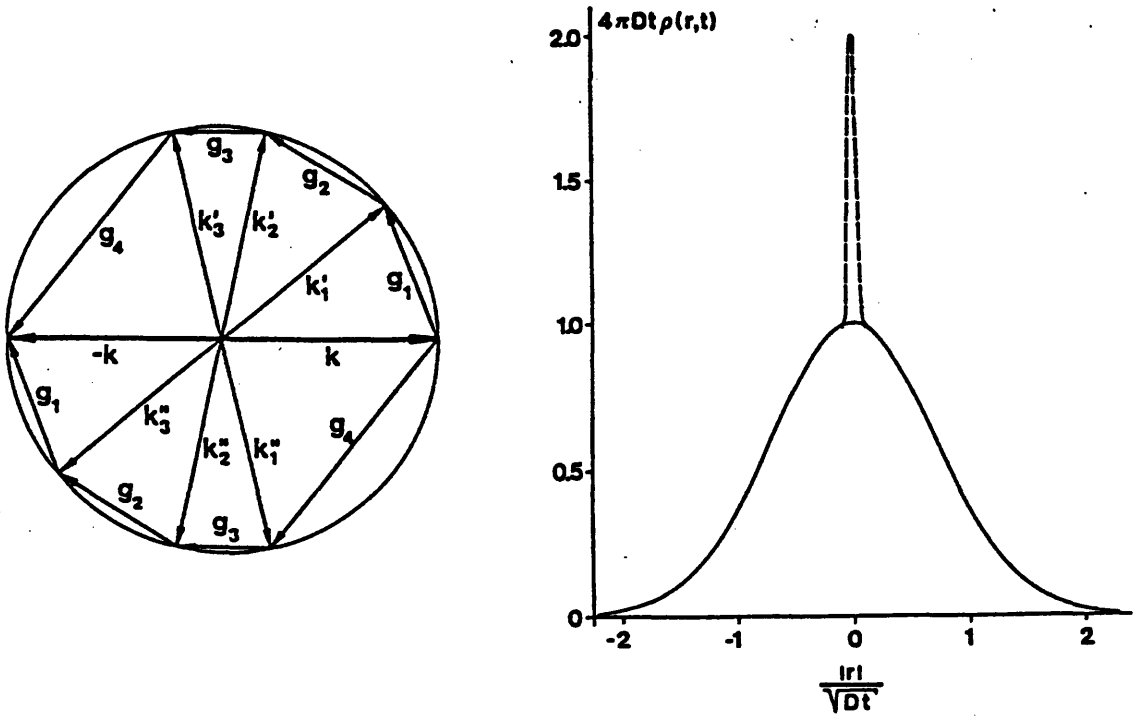

Figure 5-6: Schematic of the quantum coherent backscattering (weak localization) effect. The left figure shows the physical interpretation of the so-called "fan diagram" introduced by Langer and Neal [95] which allows calculations of quantum corrections to the conductance within the Kubo formalism, and shows enhanced scattering in the backward direction. The net effect is that an electron with an initial wavevector k scatters into two complementary series of scattering states (k', k'') connected by momentum changes (g', g'') resulting in a net amplification of scattering in the $-k$ direction. The figure on the right shows the same effect in terms of a real-space quantum diffusional model as the probability (4πDtρ(r,t)) vs. normalized position ($|r|/\sqrt{Dt}$), where the solid curve is the classical result, and the dashed curve is due to quantum coherence, showing an enhanced scattering in the backward direction[13].

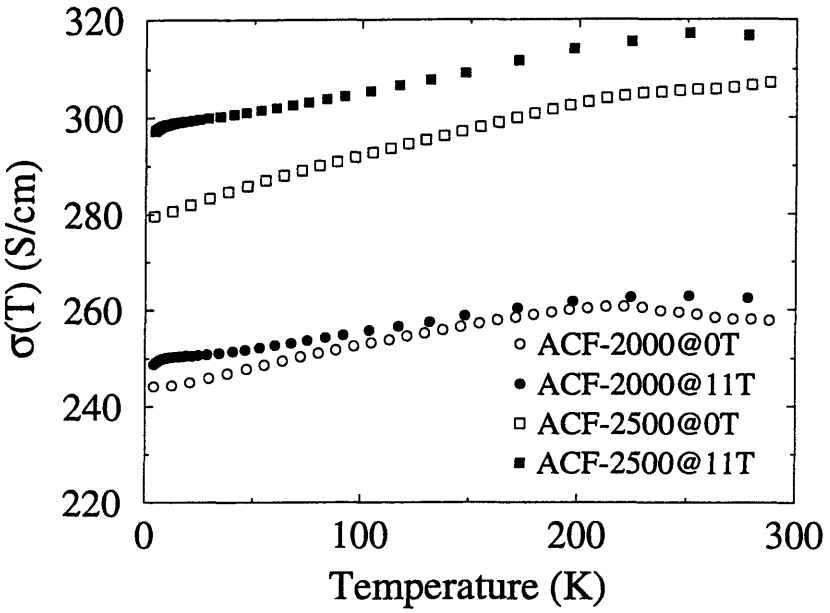

Figure 5-7: Conductivity of two FRL-based activated carbon fiber (ACF) samples with $T_{HT} = 2000°C$ and 2500°C in zero magnetic field and at 11T.

not be as field sensitive, such as EEI, as well as to characterize disorder.

5.4.3 Weak Localization and Electron-electron Interaction Effects in ACFs

In Fig. 5-7, we show the results of individual temperature scans of the conductivity at zero magnetic field and in a field of 11 Tesla. The temperature dependence is weak, varying by only ~20-30 S/cm over the entire 300 K scan which is to be compared with the several orders of magnitude increase observed in samples heat treated below the MIT over the same measurement temperature regime. The zero field plots of $\sigma(T)$ for both the ACF-2000 and ACF-2500 samples do not tend toward zero, further indicating that the charge carriers are not strongly localized. However, all samples show an increase of σ with increasing temperature, indicating semiconductor-like behavior. Thus, the heat treated fibers do not fully show metallic behavior in their transport properties, but are weakly localized due to short range disorder within the extended graphene sheets. We see also from Fig. 5-7 that the application of a magnetic field increases the conductivity in both samples over the entire temperature

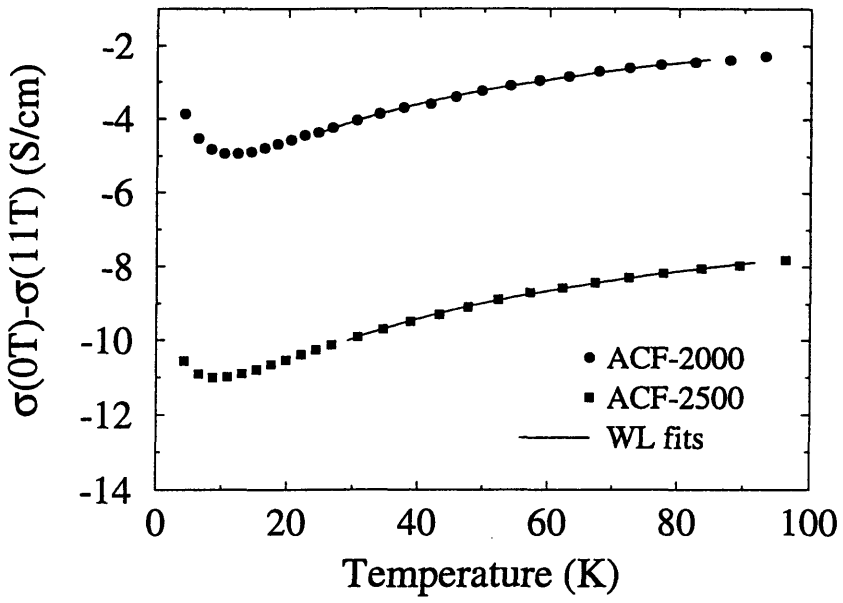

Figure 5-8: Temperature dependence of the change in ACF conductivity due to an 11T magnetic field for two samples with different T_{HT} values.

range, so that negative MR can be observed even at room temperature.

Figure 5-8 shows σ(0T)-σ(11T), the difference between the zero-field and the high-field conductivity scans, for samples heat treated at 2000° C and 2500° C along with weak localization fits. Since WL is effectively destroyed by the application of a relatively small field [12], the 11T conductivity scans exhibit T dependences arising primarily from EEI and Boltzmann (classical) mechanisms. On the other hand, the corresponding 0 T data contains contributions from WL in addition to the EEI and Boltzmann mechanisms. Thus, the difference $\Delta\sigma(T) = \sigma(0\text{T}) - \sigma(11\text{T})$ gives a temperature dependence that is related to the WL correction term. The correction due to EEI becomes more important below 20K, where an upturn in $\Delta\sigma(T)$ is observed. Thus, WL theory was used to fit the temperature scan data only down to 25K and 30K for the ACF-2000 and ACF-2500 samples, respectively. In the absence of a magnetic field, the correction in the 2D conductivity due to WL (ignoring spin-orbit and magnetic impurity effects) is given by [13]

$$\Delta\sigma_{\text{WL}} = p\frac{e^2}{2\pi^2\hbar}\ln\left(\frac{T}{T_0}\right). \tag{5.6}$$

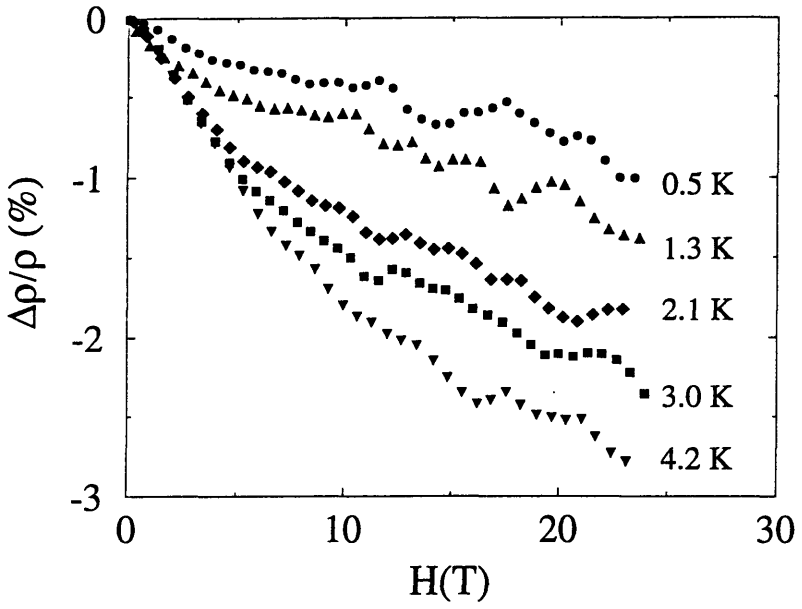

Figure 5-9: The magnetoresistance $\Delta\rho/\rho$ of the ACF-2000 sample plotted as a function of magnetic field for various temperatures below 5 K.

where p is related to the inelastic scattering process via $\tau_i \sim T^{-p}$ and T_0 is a constant characteristic of the sample. The solid lines in Fig. 5-8 represent least-square fits to Eq. 5.6 with T_0 and p as the only fitting parameters. Values of p near unity were obtained from these fits, indicating that both carrier-carrier scattering and carrier-phonon scattering play a part in determining the effective inelastic scattering length.

The EEI effect which produces the upturn in $\Delta\sigma(T)$ below 20 K in Fig. 5-8 was also studied as a function of magnetic field, where the magnetoresistance $\Delta\rho/\rho$ showed a positive contribution to the overall WL negative magnetoresistance, and this positive contribution increased with decreasing temperature. Fig. 5-9 shows MR data for ACF-2000 for magnetic fields up to 25 T. At the lowest temperature measured (0.5 K), the WL effects become nearly fully compensated by the positive EEI contribution with $|\Delta\rho/\rho| < 1$. In order to investigate the EEI effect more carefully, I fit the 4.2 K data shown in Fig. 5-9 to WL theory with and without EEI contributions. In Fig. 5-10, the effect of electron-electron interactions is shown through the combined fit of both WL and EEI correction terms to the 4.2 K MR field scans. Although a positive slope in $\Delta\rho/\rho$ was reported at high fields in similar studies of intercalated

ACFs [33], no such upturn was observed up to 25T for either of our samples. The total MR is now written as

$$\Delta\rho/\rho = (\Delta\rho/\rho)_{\mathrm{WL}} + (\Delta\rho/\rho)_{\mathrm{EEI}} \tag{5.7}$$

where $(\Delta\rho/\rho)_{\mathrm{WL}}$ is given by [13]

$$\left(\frac{\Delta\rho}{\rho}\right)_{\mathrm{WL}} = -\lambda_1 R_\Box \frac{e^2}{2\pi^2\hbar}\left\{\Psi\left(\frac{1}{2}+\frac{H_i}{H}\right) - \ln\left(\frac{H_i}{H}\right)\right\} \tag{5.8}$$

where $R_\Box$ is the sheet resistance and the characteristic field, H_i, is given in terms of the inelastic scattering time τ_i by $H_i{=}\hbar\ /4eD\tau_i$ (D is the diffusion constant). The digamma function Ψ is defined as $\Psi = d[\ln(\Gamma(x))]/dx$ where $\Gamma(x)$ is the gamma function. A scaling factor $0 < \lambda_1 \leq 1$ was used to take into account the inhomogeneity of the percolated fiber network (a value of $\lambda_1 \approx 0.1$ was used in all our fiber samples). The EEI contribution can be written as [96]

$$\left(\frac{\Delta\rho}{\rho}\right)_{\mathrm{EEI}} = \lambda_2 R_\Box \frac{e^2}{2\pi^2\hbar} g_2(h). \tag{5.9}$$

Here λ_2 is the scaling factor, $h = g\mu_B H/k_B T$, and the function g_2 behaves as $\ln(h/1.3)$ for $h \gg 1$ and as $0.084h^2$ for $h \ll 1$. A value of 2.0 was used for the Landé g factor. As expected, EEI effects are stronger for lower temperatures and higher fields. This is because the carrier sub-band spin splitting is greater for higher fields and the EEI effects dominate when the energy of the splitting is on the order of the electron thermal energy. Thus we expect EEI effects to become significant when $g\mu_B H \sim k_B T$, corresponding to a field of roughly 3 T at 4.2 K. A value of H_i=0.57 T was found for the characteristic field in the WL fit of the 4.2 K data, corresponding to an inelastic scattering length of 170 Å. This roughly corresponds to the estimated grain size of 200 Å previously found [58] in Raman studies of ACFs with similar heat treatments.

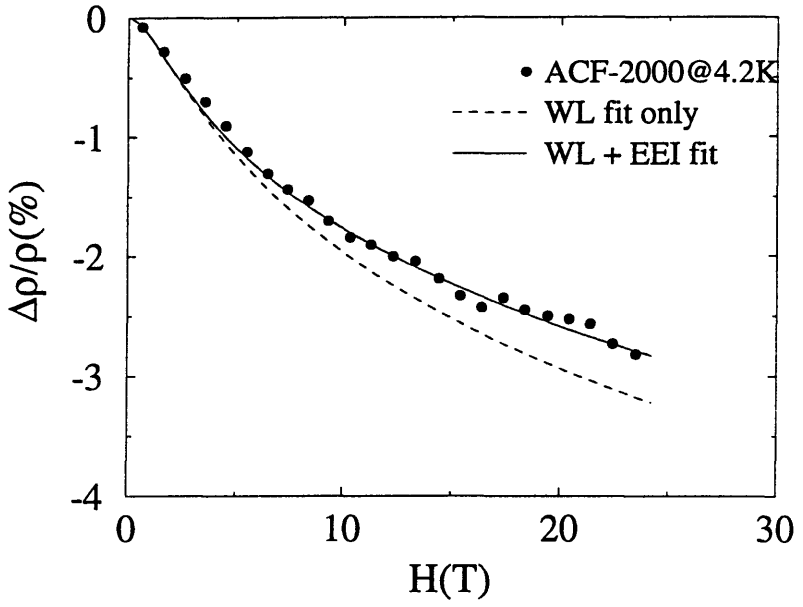

Figure 5-10: Fits of the magnetoresistance $\Delta\rho/\rho$ to WL and EEI theories for sample ACF-2000 at 4.2 K.

5.5 Future Work

The transport behavior of granular systems remains a very intriguing field. Disordered materials such as PPP- and ACF-based carbons provide systems whose degree of disorder is tunable with T_{HT}, and these systems thus are useful for studying effects such as VRH, WL and EEI. In fact, other transport behavior such as Coulomb gap effects [39] (not studied here) also become important in certain highly porous systems such as carbon aerogels [148], and can also be studied as a function of T_{HT}. Although a considerable amount of work has been done in the Dresselhaus group to investigate the transport behavior of disordered carbon structures with T_{HT} above 1000°C and room temperature conductivities $\sigma > 0.1$ S/cm [1, 56, 57, 82, 148], work remains to be done to extended the investigation to lower T_{HT} carbons. Specifically, the huge change in σ(300K) occurring near the critical T_{HT} of 700°C (see Fig. 5-5) takes place due to percolating carbonized regions that are weakly connected following partial dehydrogenation. Although high DC resistances prevented a more complete study of low-T_{HT} PPP-based carbons, AC resistivity measurements could give useful information on the characteristic length scales of these systems. Critical path

methods [3, 161] could then be applied to model the connectivity and cross-linking of polymeric/carbonaceous structures such as PPP-700.

Chapter 6

Static Magnetic Properties of Carbon-based Systems

6.1 Introduction

In this chapter I describe the diamagnetic and paramagnetic moments observed in disordered PPP- and MPCF-based carbon samples. The paramagnetism of these systems is undoubtably dominated by a large Curie-Weiss magnetic moment at low-T_{HT} values, which is due to localized spins ($N_{\rm loc} \sim 10^{19} g^{-1}$). These localized spins arise mainly in the form of dangling (unpaired) spins, and in odd-number-carbon clusters in samples with lower T_{HT}. Thus, analysis of the Curie paramagnetism can give direct characterization of disorder, which can be quantitatively evaluated in terms of a localized spin density.

The diamagnetism of carbon systems, on the other hand, is not directly linked to unpaired spins or atoms at cluster edges, but is due to the extent (or lack thereof) of the graphene/aromatic network. Thus, a large diamagnetic moment is expected for graphitic systems with large L_a, since the in-plane magnetic susceptibility $\chi_\perp$ of graphite is on the order of -21$\times 10^{-6}$emu/g (i.e., the susceptibility for **H** parallel to the c-axis). Interestingly, the out-of-plane susceptibility of graphite for **H** in the plane normal to the c-axis is $\chi_{||}$ = -0.3$\times 10^{-6}$emu/g, yielding the largest known diamagnetic anisotropy of any material. $\chi_{||}$ is essentially due to core carbon electrons, and is

independent of the $\pi-$ and $\sigma-$bonding arrangement. $\chi_{\perp}$, however, is very sensitive to L_a and decreases in magnitude with decreasing crystallite size L_a, so that evaluation of the diamagnetic susceptibility can yield information on the in-plane crystallite dimension, which can then be compared with the crystallite sizes L_a evaluated for the carbon-based systems by analysis of XRD or Raman scattering experiments, as discussed in section 3.4.

6.2 Experimental Details

Magnetization and susceptibility measurements of PPP- and MPCF-based carbons were made using a Quantum Design SQUID magnetometer over the temperature range 2.5–310 K in fields up to H=5 Tesla. The zero field susceptibility was estimated by measuring the magnetization in the low-field (linear) regime as a function of temperature and then applying the isotropic relation $\chi = M/H$.

For the magnetic alignment experiment, milled MPCFs were dispersed in ethyl alcohol, placed in a 3 cm glass dish and then mounted within a conventional DC magnet. A magnetic field of 0.3 Tesla was applied parallel to the radius of the dish. The fibers were kept in this dispersed state (for both zero field and 0.3 Tesla field measurements) for $\sim$10 minutes as the alcohol evaporated from the dish. Adhesive graphite tape was then carefully applied to the fiber sediment to allow for 3 kV high resolution SEM observations.

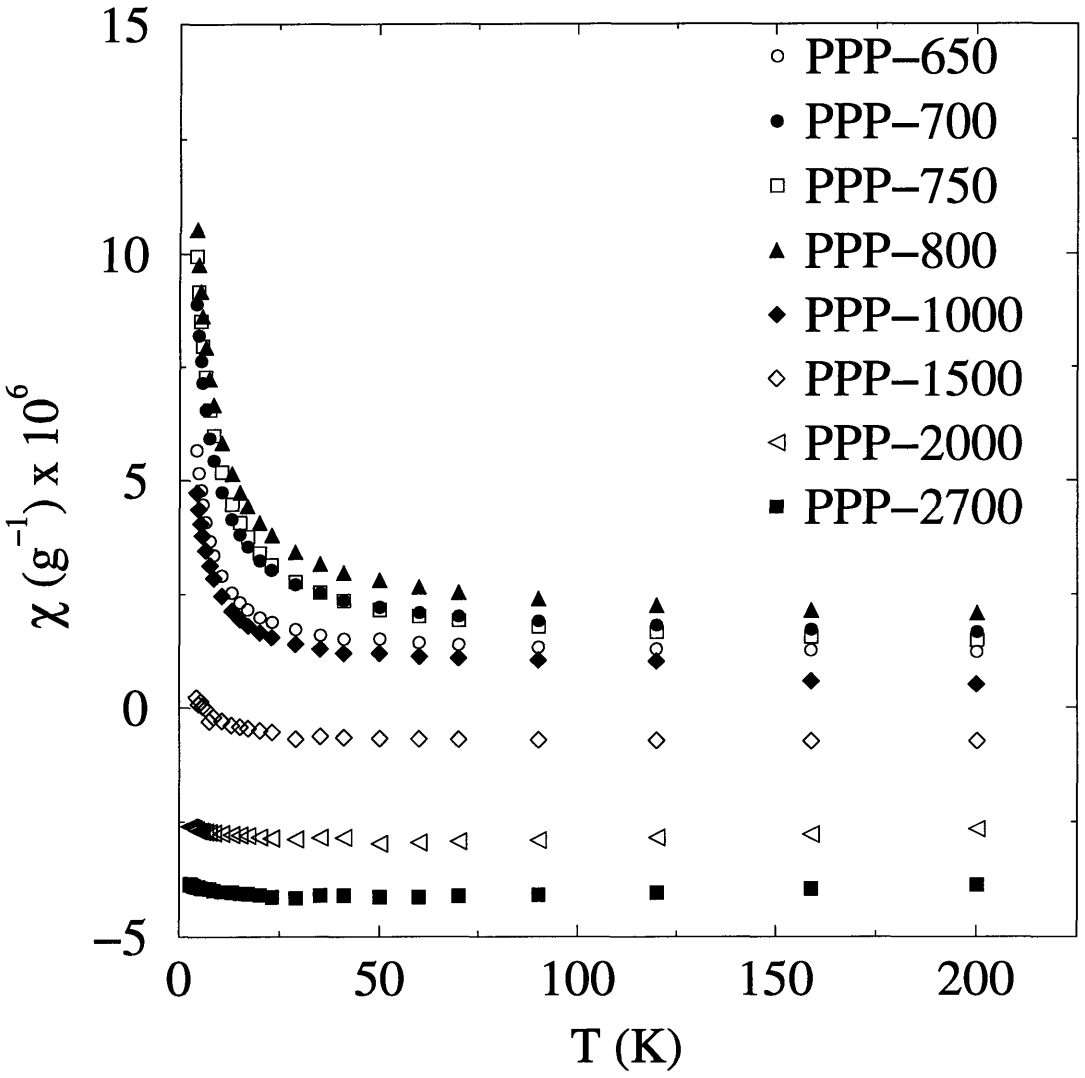

Figure 6-1: Temperature dependent magnetic susceptibility measurements for PPP samples heat treated to various T_{HT} values.

6.3 Curie-Weiss Paramagnetism in Disordered Carbons

6.3.1 PPP-based Carbons

Temperature-dependent susceptibility measurements (Fig. 6-1) for samples heat treated in the range 650°C $\leq T_{\mathrm{HT}} \leq$ 2700°C are well fit by a Curie law

$$\chi = (C/T) + \chi_0 \tag{6.1}$$

over the measurement temperature range $4 < T < 20$K, where the slowly varying offset, χ_0, represents the diamagnetic contribution which is weakly temperature dependent. In truth, there is some temperature dependence in the χ_0 term, but as we will see in the next section, this T-dependence is quite weak. From the slope of χ vs. $1/T$, the Curie constant

$$C = \frac{N_{\mathrm{loc}} S(S+1) g^2 \mu_B^2}{3k_B} \tag{6.2}$$

is obtained, from which we extract the localized spin concentration (N_{loc}) for each PPP sample (Fig. 6-2), using $g = 2.003$ and a spin quantum number $S = \frac{1}{2}$. We see that the number of unpaired localized spins N_{loc}, increases with increasing T_{HT} at low-T_{HT} values, reaches a maximum between 750°C and 800°C, and N_{loc} gradually decreases to very small values upon heat treatment to higher temperature. For T_{HT} > 800°C, we can tentatively correlate N_{loc} with the relative integrated intensity of the disorder peak from Raman data, $(I_G/I_D)^{-1}$ since a defect that produces a localized spin is also likely to produce a local loss of symmetry, which brings about the excitation of disorder-induced phonons in the Raman effect. Thus, as graphitization proceeds at higher T_{HT} values, the number of unpaired spins per unit volume formed at the dangling bonds along the edges of the pregraphitic microcrystallites tends to decrease as the amount of 'edge' vs. 'volume' of a given microcrystallite decreases.

As indicated earlier, analysis of samples heat treated in the range 650°C $\leq T_{\mathrm{HT}} \leq$

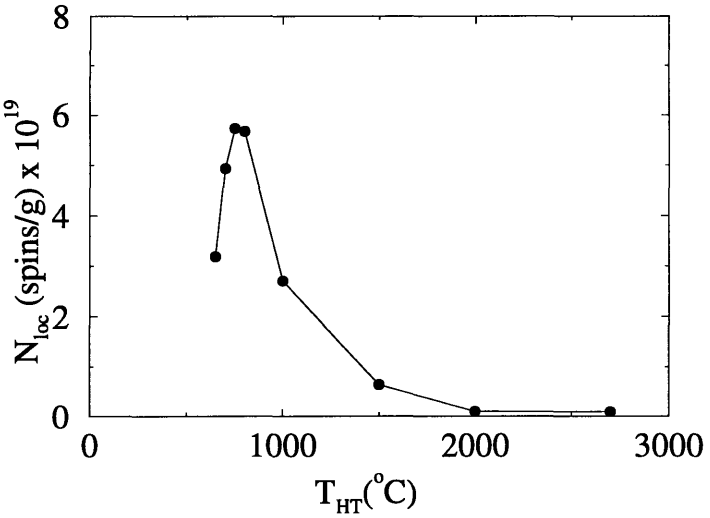

Figure 6-2: Localized spin density ($N_{\rm loc}$) for PPP-based samples heat treated at various $T_{\rm HT}$.

800°C is best done from the perspective of a disordered ($T_{\rm HT} < 775$°C) polymer, as opposed to a disordered carbon ($T_{\rm HT} > 775$°C). Hence, disorder decreases as we move away from the peak near $T_{\rm HT} \sim 775$°C in Fig. 6-2, for either increasing or decreasing $T_{\rm HT}$. At a $T_{\rm HT}$ of 650°C, many edge sites of the carbonaceous clusters, consisting of partially dehydrogenated PPP (H/C $\sim$ 0.54 from Fig. 2-3), are terminated by hydrogen atoms. These hydrogen atoms are quickly expelled at higher $T_{\rm HT}$, thus exposing unpaired electrons localized at carbon atoms along the edges and within the bulk of the crystallites. For sample PPP-700, the exposure of hydrogen-terminated sites is only partially complete (H/C $\sim$ 0.3), implying that each crystallite will have many dangling bonds as well as hydrogen atoms at edge locations. Evidence for spin centers localized near hydrogen atoms was given in terms of an unresolved hyperfine interaction in section 4.5. Interestingly, very near $T_{\rm HT} = 700$°C we find a global maximum in the total number of unpaired spins in our system. This peak bears a striking resemblance to the peak in evolved H_2 as a function of $T_{\rm HT}$ reported in Ref. [190] for measurements made on thin film PPP. Thus, the special electrochemical properties of PPP-700 may be related to this maximal exposure of *ortho*– sites which produces a maximum of localized spins. However, it would seem that the presence of hydrogen is important as well, since $N_{\rm loc}$ is also quite high for the case of PPP-725

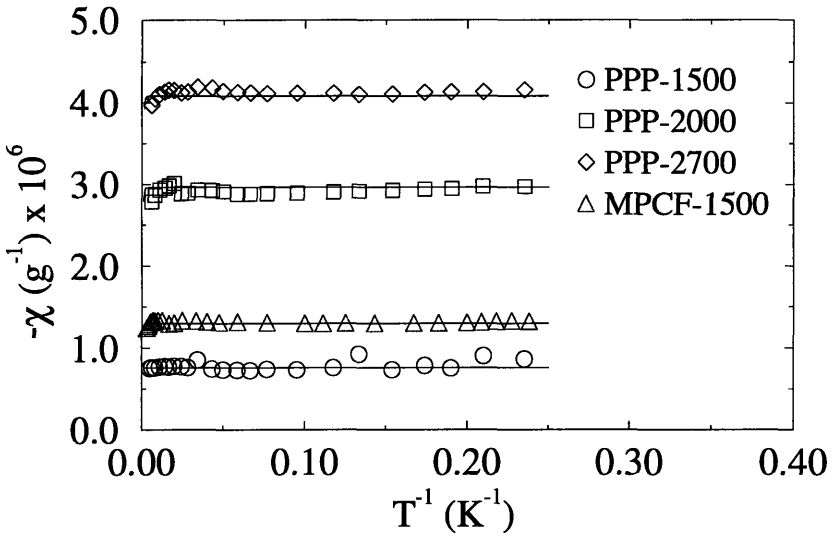

Figure 6-3: Diamagnetic susceptibility measurements for PPP- and MPCF-based samples heat treated to various T_{HT} values. The solid lines represent a fit to the London-Hoarau theory (described in the text) for P=18, 23, 34, 42 in order of increasing $|\chi|$.

and PPP-750.

6.4 Diamagnetism of Aromatic Carbon Clusters

6.4.1 PPP-based Carbons

While Curie paramagnetism dominates χ for $T_{HT} < 1000$°C, higher T_{HT} PPP samples begin to show the onset of graphite-like Landau diamagnetism which is due to conduction carriers. As mentioned in section 2.1, however, the graphitizing nature of PPP-based carbons is somewhat limited, since only the interplanar graphene distance approaches graphite values ($d_{002} = 3.352$) as T_{HT} increases to large values ($\approx 3000°$). L_a and L_c, on the other hand, remain at small values (≤ 110Å) even up to $T_{HT} = 2700$°C which can be correlated with TEM images[115] of PPP-2700 that show a ribbon-like structure for this material.

Figure 6-3 shows the diamagnetic susceptibility of PPP-based samples above T_{HT} values such that the diamagnetic susceptibility could be reasonably subtracted from the Curie-dominated curve. As is usual in the literature, I plot $-\chi$ vs. 1/T in Fig. 6-

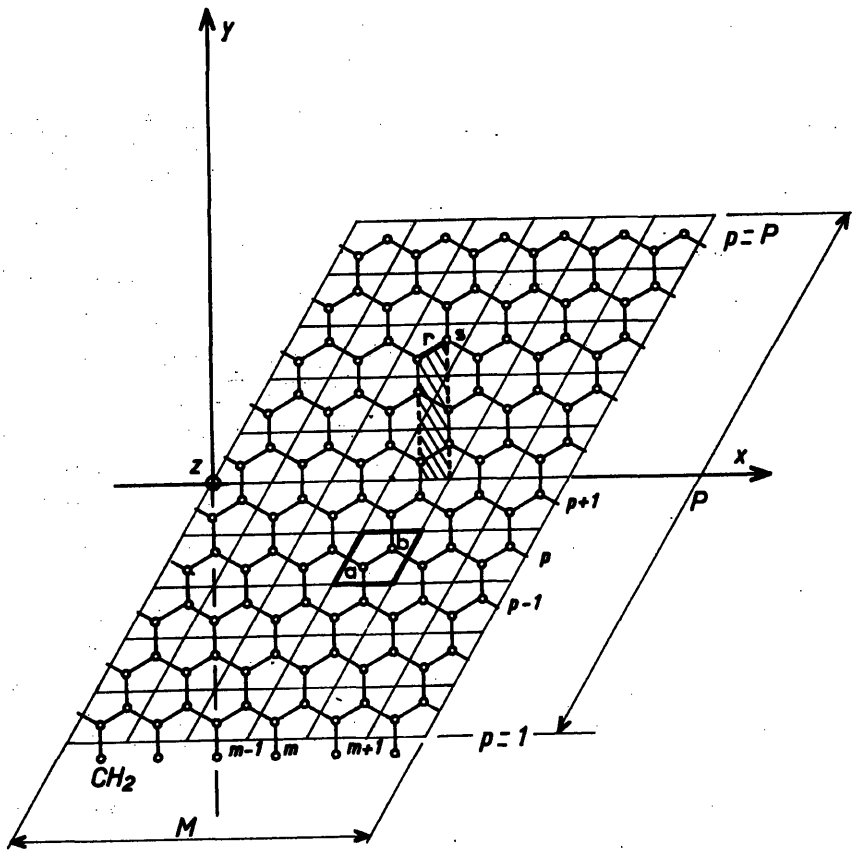

Figure 6-4: Structural model due to Hoarau and Volpilhac for a repeated MxP supercell (repeated along the x-direction) of a graphite ribbon for P=10 and M=6. Edge carbon atoms are artificially bonded to hydrogen atoms, producing non-bonding orbitals which do not contribute to the London diamagnetism. The shaded region refers to cell areas considered in the complete theory (see Appendix C).

3, and the results show a very weak temperature dependence at high measurement temperatures. Note that with higher T_{HT}, the magnitude of χ increases, and becomes more T-dependent at high measurement temperatures. For comparison, I also plot the diamagnetic susceptibility of MPCF-1500, which shows a similar L_a value ($\sim$ 50Å) to that of the PPP-based samples. Higher-T_{HT} MPCF-based samples had larger L_a values, but in this case, the special "folded" microstructure of carbon fibers[43, 135] tends to affect χ, and we will treat the magnetic properties of MPCF-3000 in section 6.4.2. However, at low-T_{HT}, MPCF samples can be expected to have disordered structures that are similar to those for the PPP-based samples.

Since the lateral extent of PPP-based carbons is limited to only dozens of aromatic

rings, the question arises as to whether a 2D graphite treatment of the magnetic susceptibility is appropriate. Hoarau and Volpilhac[69] derived a form for the magnetic susceptibility of "pregraphitic" carbons based on London's early formalism which used Hückel π-electron theory to treat the diamagnetism of aromatic molecules[103]. Figure 6-4 shows the elementary unit cell used by Hoarau and Volpilhac to calculate the electronic properties of ribbons of 2D graphite, confined in the "P" direction, but repeated in the "M" direction, and the calculations were carried out using cyclic Born-von Karman conditions. This produces a *discrete* energy spectrum, which in the absence of a magnetic field, is given by

$$E_{\pm}^{0} = \pm\beta^{0}(1 + 4\cos^{2}u + 4\cos\vartheta\cos u)^{1/2} \tag{6.3}$$

where $u = \pi j/\mathrm{M}$ and $\vartheta = \pi k/(\mathrm{P}+1)$ for $0 < j,k \in (\text{integers}) < \mathrm{M},\mathrm{P}$. The overlap integral $\beta^{0} \approx -2.3$ eV is analogous to the γ_0 term introduced by Wallace[183] and used in McClure's formalism for the magnetic susceptibility for 2D graphite[117]. The lower value for this overlap integral (as compared to the $\gamma_0 = -3.1$ eV value) is chosen so that the energy spectrum is more consistent with small aromatic structures like benzene[136].

In the presence of a magnetic field, the levels split, producing an average magnetization $\langle \mathbf{M} \rangle = -\partial F/\partial \mathbf{H}$ where the free energy F is written as an ensemble of particles with energies given by Eq. 6.3 (see Appendix C). The final form of the orientationally averaged diamagnetic susceptibility is given by

$$\chi_{dia}(T) = \frac{1}{3}\chi_{\perp} + \chi_{\parallel} = \frac{1}{3}(\chi_{I}^{L} + \chi_{II}^{L}) + \chi_{\parallel} \tag{6.4}$$

where the $\chi_{\parallel}$ term takes into account the in-plane core diamagnetism neglected by London's theory. The London contributions to $\chi_{\perp}$ are explicitly given by

$$\chi_{I}^{L} = \frac{N(\beta^{0})^{2}\xi^{2}}{12\mathrm{M}(2\mathrm{P}+1)} \sum_{\vartheta,\ u} Q_{1}^{2}(\vartheta,u)\left[f(E_{+}) + f(E_{-})\right], \tag{6.5}$$

Table 6.1: Summary of PPP-based carbon static magnetic properties.

Sample	χ_0 $g^{-1} \times 10^6$	P	L (Å)	L_a (Å)
PPP-1500	-0.75	18	44	38
PPP-2000	-3.25	34	68	71
PPP-2700	-4.62	42	110	88
MPCF-1500	-1.30	23	46	48

$$\chi_{II}^{L} = \frac{-N\beta^0\xi^2}{6\mathrm{M}(2\mathrm{P}+1)} \sum_{\vartheta,\, u} Q_2(\vartheta, u)\,[\bar{n}(E_+) + \bar{n}(E_-)] \tag{6.6}$$

where the London factors Q_1, Q_2 are functions of the ribbon width parameter P, and are given in ref. [20], while $\bar{n}(E_\pm)$ is the Fermi occupation number and $f(E) = \partial\bar{n}(E)/\partial E$, while $\xi = 2e\eta/\hbar c$ where η is the surface area of a graphene hexagon. I have neglected to include the Pauli paramagnetic contribution χ_P, since theoretical calculations[69] have shown that for M=200 and P<90, $\chi_P < 10^{-9}\ g^{-1}$, and therefore χ_P negligible.

Using M=200, and various values of P, Eq. 6.4 was used to fit the diamagnetic susceptibility of PPP-based carbons from $T_{HT} = 1500$°C up to $T_{HT} = 2700$°C. The extracted values for P can then be converted to equivalent ribbon widths L using the relation[69] $L = 2.1\mathrm{P}$ where L is in Å. Table 6.1 shows the comparison of the L ribbon width with the in-plane crystallite size L_a found in section 3.4.1. We note that the two lengths are well coordinated, and, in fact, agree quite well. Although the physical picture of confined regions of graphitic material would imply that one should consider disconnected "sheets," such a model would not explain the relatively high conductivities ($\sim$ 1 S/cm) in carbonized samples. As described in section 5.3, the conductivity of low-T_{HT} samples is limited mainly by hopping in a strong localization regime. Above $T_{HT} = 1000$°C, however, the graphitic regions must be more strongly connected, thereby producing a conductive path. There is still lateral confinement, however, even in samples with T_{HT} values above 1000°C, which is evidenced both by Raman and XRD studies. Therefore, a ribbon-like structure can explain the structural, electronic and magnetic data for heat-treated PPP and related carbons.

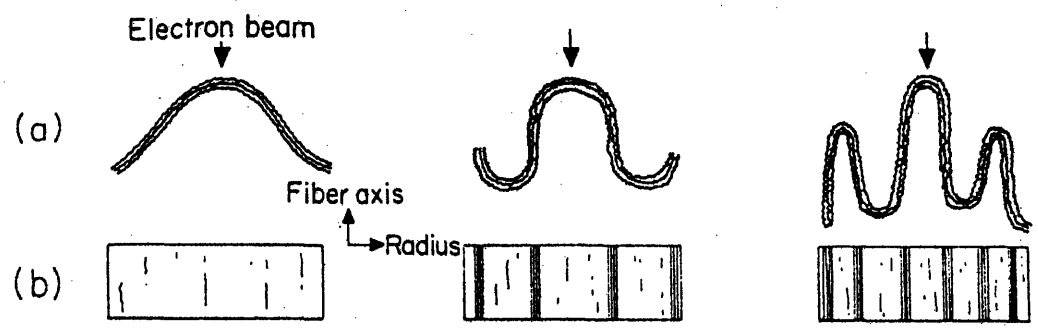

Figure 6-5: Folded ribbon model used to explain how various folded graphene structures shown in (a) can produce associated 002 dark field TEM images, shown schematically in (b), which were observed for the case of MPCFs[43]. Where the electron beam strikes the ribbon at an angle such that the graphene layers are nearly parallel with the beam, a dark image is observed[36, 43].

Other structural considerations, such as the folding of graphene ribbons, should also affect the diamagnetism, and in fact it becomes necessary to consider the effect of the folding of graphene ribbons (see Fig. 6-6) for the case of carbon fibers (McClure-Hickman Theory). I consider these effects in section 6.4.2.

6.4.2 MPCFs

Unlike the case of heat-treated PPP, the diamagnetism of high-T_{HT} carbon fibers based on various precursors has been studied extensively[36, 51, 110]. For the case of pitch-based carbon, heat treatment at high T_{HT} produced quite graphitized materials, as compared to so-called "hard carbons" such as PPP. Although the general behavior of the temperature dependence of χ(T) in graphite materials was explained by McClure[117], who applied Luttinger and Kohn's method to a quasi-two dimensional graphite lattice and derived a form for the magnetic susceptibility in the zero field limit. Ultimately, however, a more complete analysis must be made that takes into account the microstructure of the carbon fibers.

High resolution TEM work by Oberlin *et al.* for PAN-based carbon fibers[135] and by Endo for MPCFs[43, 63, 64] gives evidence that the microstructure of carbon fibers can be characterized by a turbostratic arrangement of graphene ribbons which have many kinks and folds within each ribbon. Figure 6-5 shows the folded ribbon model

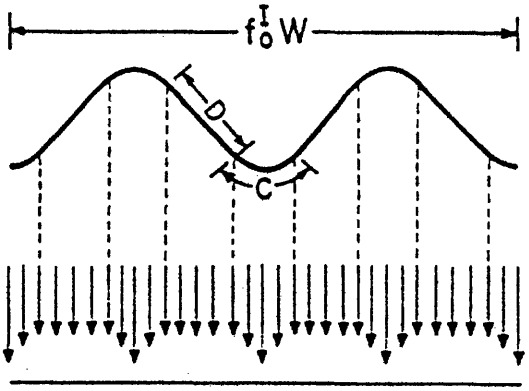

Figure 6-6: Cross section of the folded ribbon model. The graphene sheets extend infinitely in the x-direction which is perpendicular to the plane of the diagram. The vertical arrows represent the effective component of a magnetic field applied perpendicular to the ribbon[119].

used in Ref. [43] to explain the 002 dark field TEM images observed in MPCF samples. The ribbons are assumed to stack locally, with interlayer spacings typically larger than that of graphite ($d_{002} > 3.354$ Å), and the layers are arranged such that their c-axes are along a direction perpendicular to the fiber axis. By considering this microstructure, McClure and Hickman (MH) derived a form for χ(T), based on McClure's earlier formalisms, that indeed describes the observed temperature dependence of χ(T) for various carbon fibers[119]. The particular form of the susceptibility trace derived by MH can be written as

$$\chi_T = (f_0^I)^2 \chi_{00}^I + [1 - (f_0^I)^2]\chi_{11}^{II} + \chi_b. \tag{6.7}$$

Here f_0^I is the folding ratio, χ_{00}^I and χ_{11}^{II} are related to the components of the magnetic field perpendicular and parallel to the graphene ribbon, respectively, and χ_b is a constant background term, typically about 0.5 x 10^{-6} emu/g. The folding ratio is defined as $f_0^I = W'/W$ where W' is the width of the folded ribbon, while W would be the width of the ribbon unfolded. Figure 6-6 shows a schematic of the structural model used in the MH theory for a single graphene sheet. χ_{00}^I and χ_{11}^{II} are functions of ribbon width, W (to be compared with the London-Hoarau ribbon width L), the in-plane interaction energy, γ_0, and the folding wavelength, $L' = C + D$ (see Fig. 6-

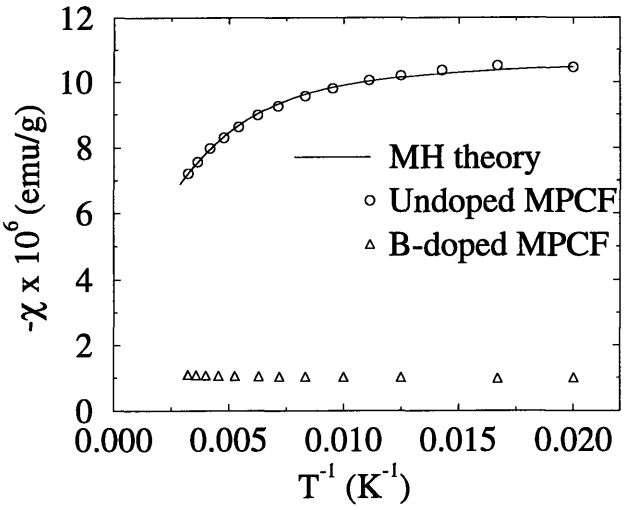

Figure 6-7: Plot of χ vs. 1/T for MPCF powder samples, both undoped and ~1% B-doped. The solid line represents a fit to the undoped fiber data using the McClure-Hickman model.

6). The particular forms of the optimized susceptibility fitting functions are given in ref. [119].

In Fig. 6-7 the results of magnetic susceptibility measurements for undoped and B-doped MPCF-3000 are shown along with a fit of the undoped data to the function given by Eq. (6.7). Reasonable agreement is found between theory and experiment, if one uses the following parameters: γ_0 = -2.8 eV, f_0^I = 0.39, W = 384 Å and L' = 22 Å. These parameters are in general agreement with previous results for high-T_{HT} carbon fiber systems[110, 119]. Although a reasonable fit is obtained assuming a folded ribbon model, we note that other approaches based on defect scattering arguments may also apply to such a system[84]. The B-doped data were not fit to the MH model because, although MH theory treats the microstructural effects in detail, it removes any dependence on acceptor doping levels by implicitly assuming that the Fermi level lies exactly midway between conduction and valence bands (where they meet in 2D graphite). I will briefly discuss the effect of boron doping on χ for the case of MPCFs in section 6.4.3.

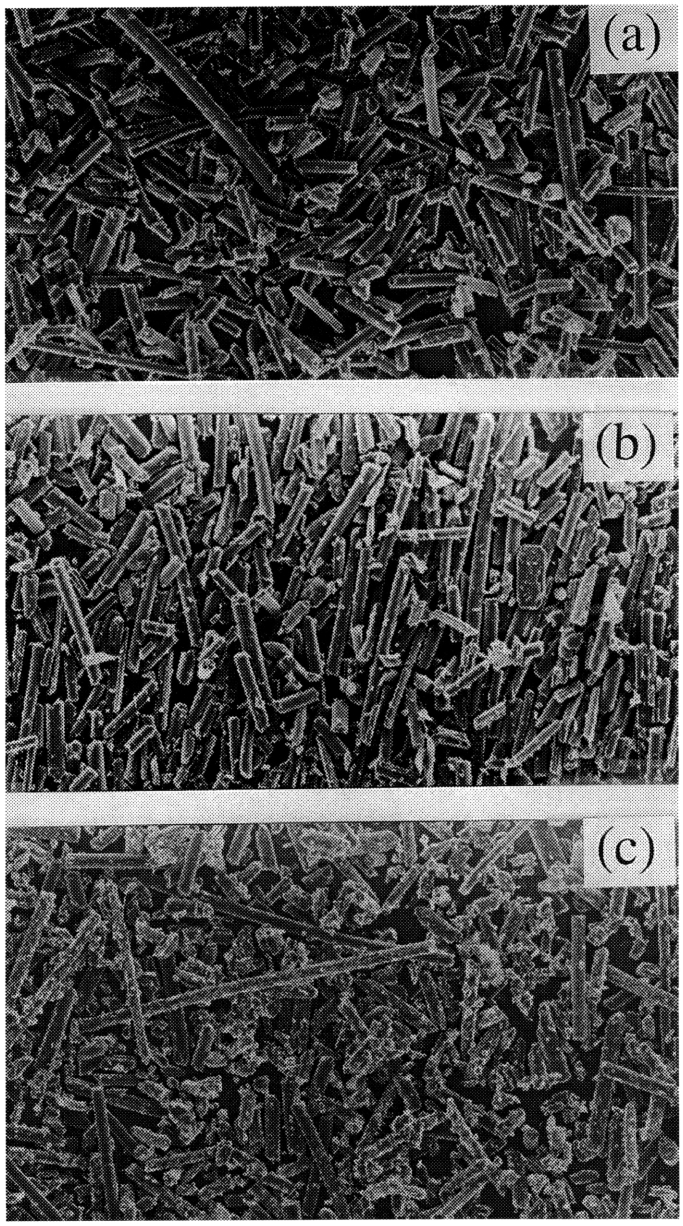

Figure 6-8: SEM images of undoped MPCFs in zero field (a) and in a field of 0.3 Tesla (b) where the magnetic field H is oriented in the vertical direction of the SEM images. Comparing (a) and (b), a clear alignment effect is observed due to the applied magnetic field. This alignment effect was not observed in B-doped samples, also exposed to a 0.3 Tesla field (c)[114].

6.4.3 Magnetic Alignment of Carbon Fibers

The SEM images of Fig. 6-8 show the effect of a magnetic field on the alignment of milled MPCFs[114]. In Fig. 6-8(a), many short undoped MPCF segments are visible with an overall random arrangement of the fibers, while Fig. 6-8(b) shows the effect of a 0.3 Tesla magnetic field on the alignment of these fibers. The same experiment was performed on B-doped MPCF samples, but from Fig. 6-8(c), we see that the application of a 0.3 Tesla magnetic field apparently has a very much smaller alignment effect on the B-doped fibers, in terms of macroscopic alignment of the fiber segments. In order to quantitatively assess the amount of alignment observed in each of the SEM images of Fig. 6-8, fiber angles θ were directly measured from an arbitrarily chosen 100x600μm area of each image containing roughly N_s=40 fiber segments. Histograms of the resulting data are plotted in Fig. 6-9 showing clearly the higher probability for a given fiber to be aligned for the case of undoped fibers in a magnetic field of $H = 0.3$ T as compared to the other two cases (zero field of boron doped).

As a first approximation, this observation may be understood by considering a given fiber to be composed of $\mathcal{N}$ non-interacting (flat) 2D graphene sheets which are parallel to the fiber axis, but are otherwise randomly arranged (see Fig. 6-10). We use a Cartesian coordinate system with the z-axis along the fiber axis such that the magnetic field lies in the y-z plane and makes an angle θ with the z-axis. Let the ith graphene sheet within the fiber have a normal vector $\hat{\mathrm{n}}_i$ that makes an angle ϕ_i relative to the x-axis. The magnetic moment per unit mass of the ith sheet in the presence of an applied magnetic field can be written in terms of a transformed magnetic susceptibility tensor, χ', and expressed as

$$\mathbf{M}_i = \chi' \cdot \mathbf{H} = R^{-1}(\phi_i)\chi R(\phi_i) \cdot \mathbf{H} \tag{6.8}$$

where $R(\phi_i)$ corresponds to a ϕ_i rotation about the fiber axis (see Fig. 6-10), and χ is diagonal. Note that the tensor elements of χ ($\chi_\perp$, $\chi_\parallel$, $\chi_\parallel$, where $\chi_\perp$ is the component of χ for H normal to the graphene sheet) are all negative, and highly

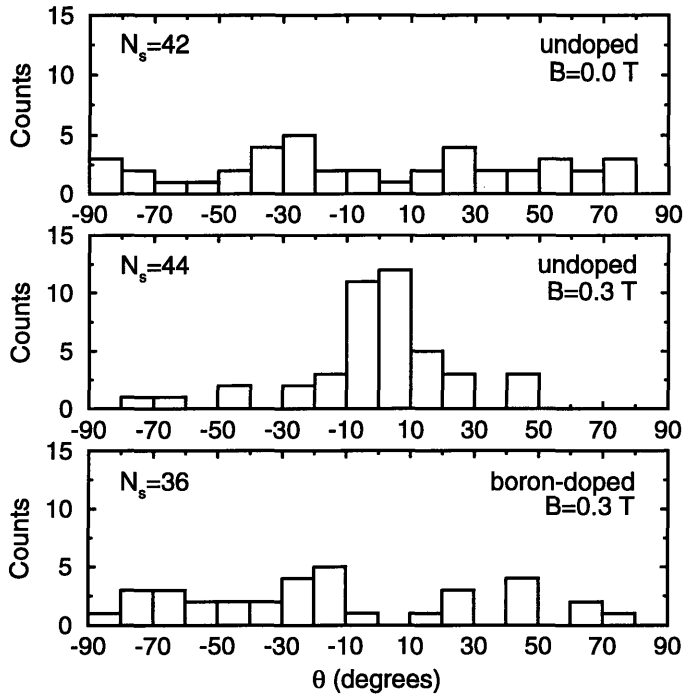

Figure 6-9: Histogram plots of the angle θ that each fiber in a $100\times600\mu$m area of the SEM images (containing N_s fibers) in Fig. 6-8 makes with the applied magnetic field H. A clear tendency for fibers to align in a magnetic field is observed in the middle plot.

anisotropic ($|\chi_\perp| \gg |\chi_{||}|$). Evaluating the matrix products in Eq. (6.8) yields

$$\mathbf{M}_i = H \begin{pmatrix} [\chi_\perp - \chi_{||}]\cos\phi_i \sin\phi_i \sin\theta \\ [\chi_\perp \sin^2\phi_i + \chi_{||}\cos^2\phi_i]\sin\theta \\ \chi_{||}\cos\theta \end{pmatrix}. \tag{6.9}$$

Using this expression for $\mathbf{M}_i$, we can write down a form for the total energy of the $\mathcal{N}$ sheets in terms of a sum of the energies for each sheet of mass m_i to obtain

$$\begin{aligned} \varepsilon(\theta) = \; & -H^2 \textstyle\sum_i^{\mathcal{N}} m_i \{(\chi_\perp \sin^2\phi_i + \chi_{||}\cos^2\phi_i)\sin^2\theta \\ & + \; \chi_{||}\cos^2\theta\} \end{aligned} . \tag{6.10}$$

If $\mathcal{N}$ is large and ϕ_i is a random variable, the sum in Eq. (6.10) may be approximately evaluated using $\sum m_i \sin^2\phi_i \approx \mathcal{N}\bar{m}\langle\sin^2\phi_i\rangle = \mathcal{N}\bar{m}/2$, and similarly for the sum on $m_i\cos^2\phi_i$. Here $\bar{m}$ represents the average mass of a single graphene sheet in the sample, where we assume that the sets $\{m_i\}$ and $\{\phi_i\}$ are independent. Since $\mathcal{N}\bar{m}$ is

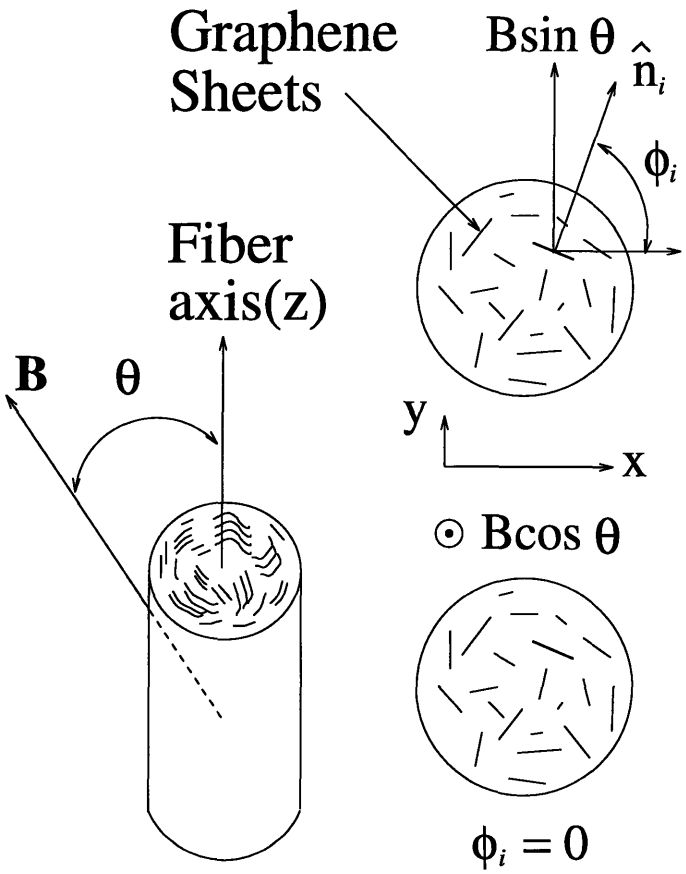

Figure 6-10: Schematic diagram of a typical MPCF showing the parameters used in the alignment model of the fibers in a magnetic field.

just the total mass of the fiber, which can be expressed in terms of the fiber length, ℓ, fiber radius, R, and fiber mass density, ρ (assuming a cylindrical geometry), we can then rewrite the total energy of a fiber in a magnetic field $\varepsilon(\theta)$ as:

$$\varepsilon(\theta) = \frac{1}{2}\pi R^2 \ell \rho H^2 \sin^2\theta |\chi_\perp - \chi_\parallel| + \pi R^2 \ell \rho H^2 |\chi_\parallel|. \tag{6.11}$$

We immediately see that $\varepsilon(\theta)$ has a global minimum at $\theta = 0$, resulting in a preferred orientation of the fiber axis along the magnetic field. The dependence of $\varepsilon(\theta)$ on orientation results in a net torque τ on each fiber which can be derived from $\tau = \partial\varepsilon/\partial\theta$ yielding

$$\tau = \pi R^2 \ell \rho H^2 \sin\theta\cos\theta |\chi_\perp - \chi_\parallel|. \tag{6.12}$$

Note that τ scales directly with the magnetic anisotropy and that $\tau \to 0$ for perfectly aligned ($\theta = 0$) or misaligned ($\theta = \pi/2$) fibers. We stress that this simple treatment neglects many details of the fiber system, particularly edge effects, misalignment of sheets relative to the fiber axis, and other inhomogeneities in the fiber.

In light of the above model, the effect of B-doping on the alignment of fibers in a magnetic field can then be easily understood. Substitutionally-doped boron in a graphitic lattice acts as an acceptor, thereby lowering E_F on the basis of a rigid band model[36, 110] and reducing the average magnitude of both the diamagnetic susceptibility of each fiber and its magnetic anisotropy $|\chi_\perp - \chi_\parallel|$ [120]. The main effect of E_F depression on the magnetic susceptibility is to effectively remove the large contribution of the lowest magnetic energy π orbitals near the conduction band and valence band junction[36]. From Eq. (6.12), the reduction of $|\chi_\perp - \chi_\parallel|$ results in a lower net torque acting on a given misaligned fiber. Furthermore, since the magnetic anisotropy for B-doped MPCFs at room temperature is almost a factor of 10 smaller than for undoped MPCFs at room temperature (see Fig. 6-7), we can see that the net torque on a given fiber will be correspondingly smaller. We also mention that the downward shift in E_F, which reduces the net magnetic anisotropy, is also thought to give rise to the observed enhancement of the charge-discharge capacity in B-doped MPCF-based electrodes, as compared to the undoped system.

In terms of applications of the fiber alignment effect, preferential orientation of the MPCFs during preparation of MPCF-based negative electrodes in a Li-ion secondary battery may be used to enhance battery performance as well as the electrode mass density as a result of better fiber alignment [42, 130]. Since an aligned fiber sample should show some bulk anisotropy in both the electronic and ionic transport properties, fiber alignment in the anode might increase the charge-discharge rates. Aligned fibers could also find application in cold cathode ray tube (CRT) technology, since an applied voltage has been shown to stimulate field emission from carbon fiber tips[7, 8]. An increase in carbon fiber quality (particularly of the tip) coupled with an efficient means of alignment could help to overcome some of the previous drawbacks of the carbon field emitter, such as poor reproducibility and tip lifetime. Recently, the potential for using aligned carbon nanotubes for CRT applications was demonstrated in terms of a very compact flat panel display[31]. In this work, alignment of the nanotubes was achieved by rubbing the nanotube samples with a piece of Teflon or aluminum foil. Since nanotubes[146] possess a magnetic anisotropy similar to that found in carbon fibers or graphite, magnetic fields should provide a convenient means for the alignment of carbon nanotubes, provided the individual nanotubes can be made sufficiently mobile.

6.5 Future Work

Future work in the area of diamagnetic characterization of novel carbon materials could include work on nanotube samples, since the large moment in these samples will also be quite size (both length and diameter) dependent[152]. Such a study could yield important experimental information on the interesting electronic structure of carbon nanotubes. Moreover, in terms of the fibers, a more complete theoretical model could be developed, which would include explicitly the effects of microstructural disorder in the form of folding and dangling bonds, and boron doping.

Chapter 7

Ab Initio Investigation of Polyparaphenylene

7.1 Introduction

In this chapter I briefly describe the calculated ground state geometries for polyparaphenylene as determined through *ab initio* energy minimization techniques. This ground state configuration is then perturbed theoretically by exciting an electron from the highest occupied molecular orbital (HOMO) energy level to the lowest unoccupied molecular orbital (LUMO) level in order to investigate the coupling of phonon modes to electronic transitions. The results of force calculations can then be used to determine which phonon modes couple most strongly to the lowest lying electronic transitions.

In what follows, I first describe in section 7.2 the concepts and algorithms involved in the energy minimization calculations. This is followed by section 7.3, where the results for the ground state geometry investigations are presented, yielding ground state lattice constants and bond angles. In section 7.4, I present a method, which is completely *ab initio*, for investigating the vibronic-electronic structure and I then discuss the theoretical results obtained for the PPP molecular configuration. Finally, I briefly discuss the prospects for future work in this field in section 7.5.

7.2 *Ab initio* Iterative Minimization Techniques

In this section I review the basic principles of total energy pseudopotential calculations. An excellent review can be found in ref.[138], which describes both the solid state theory and the iterative minimization algorithms involved in state-of-the-art pseudopotential calculations.

In contrast to the formalism presented in section 3.2, the present method does not explicitly treat the dynamic lattice. Instead, a fixed set of ionic coordinates is used. Again, the justification for considering a static lattice for the dynamic electron-ion problem is generated from the adiabatic approximation, where the ionic motions are much slower than those of the electrons. A plane wave basis set is used for the electronic wavefunctions, and in order to limit the plane wave set to a tractable size, a pseudopotential $V_{\text{ion}}(\mathbf{r})$ with associated pseudo-electrons is considered instead of the actual $\sim 1/r$ potential of the ionic cores[24, 141]. The electron-electron interactions (EEI) are handled by way of density functional theory (DFT)[70, 81] coupled with a local density approximation (LDA). Using DFT, the strongly interacting many-electron problem can be mapped onto a set of non-interacting one-electron problems (moving in an effective potential) to produce the same total ground state energy as a unique function of electron density. The equivalent one-electron eigenvalue problems are given by the single particle Kohn-Sham equations[81]:

$$\left[-\frac{\hbar^2}{2m}\nabla^2 + V_{\text{ion}}(\mathbf{r}) + V_H(\mathbf{r}) + V_{XC}(\mathbf{r})\right]\psi_i(\mathbf{r}) = \varepsilon_i(\mathbf{r}), \tag{7.1}$$

where $\psi_i(\mathbf{r})$ is the wave function of the electronic state i, ε_i is the Kohn-Sham eigenvalue, and the Hartree potential $V_H(\mathbf{r})$ is given by

$$V_H(\mathbf{r}) = e^2 \int \frac{n(\mathbf{r}')}{|\mathbf{r}-\mathbf{r}'|} d^3\mathbf{r}'. \tag{7.2}$$

Here $n(\mathbf{r}) = 2\sum_i |\psi_i(\mathbf{r})|^2$ is defined as the electronic density of doubly occupied electronic states. After the exchange-correlation potential $V_{XC}(\mathbf{r})$ is appropriately chosen, self-consistent minimization of the Kohn-Sham eigenvalues with respect to

one-electron densities will then lead to wavefunctions that minimize the *Kohn-Sham energy functional*

$$E[\{\psi_i\}] = 2\sum_i \int \psi_i^* \left(-\frac{\hbar^2}{2m}\right) \nabla^2 \psi_i d^3\mathbf{r} + \int V_{\text{ion}}(\mathbf{r}) n(\mathbf{r}) d^3\mathbf{r} + \frac{e^2}{2} \int \frac{n(\mathbf{r}) n(\mathbf{r}')}{|\mathbf{r} - \mathbf{r}'|} d^3\mathbf{r} d^3\mathbf{r}' + E_{XC}[n(\mathbf{r})] + E_{\text{ion}}(\{\mathbf{R_I}\}). \tag{7.3}$$

Minimization of the Kohn-Sham energy functional gives the total ground state of the system. In Eq. 7.3, the ion-ion interaction described by $E_{\text{ion}}(\{\mathbf{R_I}\})$ can be conveniently solved using Ewald's method[192].

In terms of the actual calculation of the total energy, the problem then is to efficiently solve the set of equations given in Eq. 7.1. This can be done using a number of different algorithms. Car and Parrinello[16] developed a way to treat the electronic wave functions $\{\psi_i\}$ as dynamical variables in a Lagrangian that yields an equation of motion (EOM) in terms of the Kohn-Sham Hamiltonian and $\{\psi_i\}$. Although this algorithm is not so accurate, it is relatively fast converging for its memory usage, and it is convenient to use when starting from a random set of initial plane waves. Thus, the calculations performed in this thesis were first done for a few iterations of the EOM starting with a random plane wave set, and then employing the more powerful preconditioned gradient (PCG) technique developed by Teter *et al.*[178].

After minimizing the total energy of a fixed ionic configuration with respect to the electronic degrees of freedom, the entire structure can be *relaxed* by allowing the ions to move along (negative) force field gradients. The ionic moves are done in increments so that after each move the electronic energy can again be minimized for the slightly new ionic configuration. One way to do this is to calculate the force on each ion and to divide by some spring constant to determine the displacement or step length. The jth component of the force on ion i for a given configuration with energy E can be written as[50]

$$f_{ij} = -\frac{dE}{d\tau_{ij}} \tag{7.4}$$

where $d\tau_{ij} = (dx, dy, dz)$ for the ith ion. The new ionic positions $\{\mathbf{r_i}\}$ are then expressed as

$$\mathbf{r_i} = \mathbf{r_i^0} + K_{spring}^{-1}\mathbf{f_i} \tag{7.5}$$

where $\mathbf{r_i^0}$ is the old ionic position and K_{spring} is an effective spring constant for the system. If the exact values for K_{spring} for each ion were known and applied, the system would relax as it would in nature; however, knowledge of the exact values is not necessary in order to find the minimum in energy. The choice of K_{spring} is then somewhat arbitrary, but if K_{spring} is too small, the change in position $\Delta\mathbf{r_i} = K_{spring}^{-1}\mathbf{f_i}$ will be too large, and the ionic motions will "overshoot", causing the system to diverge away from equilibrium. Therefore, the spring constant should be chosen to be larger that the stiffest K_{spring} of the real system, which in this case is the K_{spring} of the H-C bond. The vibrational frequency ω_{H-C} of a typical aromatic normal mode involving multiple H-C bonds can be estimated from the H-C stretch optical mode frequencies of substituted benzene ring structures[25] which are about 3100 cm^{-1} in magnitude. Using the proton mass $m_p = 1.67 \times 10^{-24} g$, the spring constant is estimated to be approximately $K_{spring} \approx m_p\omega_{H-C}^2 \approx 36$ eV/ Å^2. To ensure that K_{spring} is greater than any effective spring constant in the system, a value of 60 eV/ Å^2 was used since it allowed for rapid relaxation of the ionic positions without any divergence of the ionic motions.

7.3 PPP Ground State Geometries

The polycrystalline structure of Kovacic-type PPP has been investigated by Kawaguchi and Petermann[76] using electron diffraction, showing that the structure is nematic with a parallel-chain packing structure. The orthorhombic unit cell was found to be $(a, b, c) = (7.781, 5.520, 4.300)$ (in units of Å), where a, b are normal to the chain axis and c is along the chain axis. In the a, b plane there are two chains per unit cell, while along the c-axis, two phenyl groups of each chain form the basis of the unit cell as shown in Fig. 7-1. I assume a *Pbam* space group symmetry, as opposed to a *Pnnm* structure, although this choice is somewhat arbitrary. The *Pbam* and *Pnnm* space

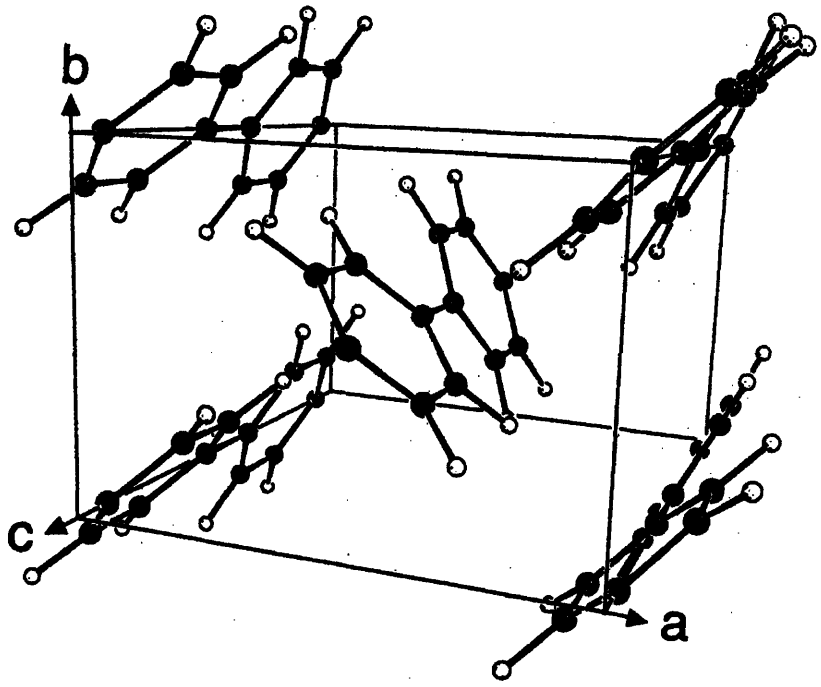

Figure 7-1: 3D structure of crystalline PPP corresponding to the *Pbam* space group. The dark circles that form hexagons correspond to the carbon backbone, while the light circles correspond to hydrogen atoms. The unit cell contains only two (rotated by $\sim 90°$ out-of-phase) bi-phenyl units, although five chain segments are included in the figure to show the packing structure[4].

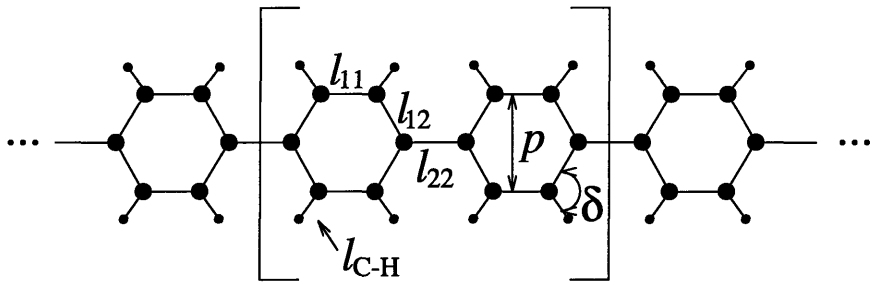

Figure 7-2: Molecular structure of a single PPP chain indicating the structural parameters listed in Table 7.1. The brackets indicate the 8.54 Å repeat unit. Two such units of two PPP chains form the unit cell of the 3D structure.

groups are related to one another by a $c/2$ shift along the c-axis of one of the chains in the unit cell, so that a moderate amount of shift disorder, which is observed from electron diffraction studies[76], can produce a coexistence of the two structures. As it turns out, previous *ab initio* calculations of the electronic structure of PPP that were performed with both structures yielded almost identical results[4].

Figure 7-2 shows the geometry of a single PPP molecule and the structural parameters extracted from the calculations following relaxation of the ionic positions are indicated on the figure. The ground state energy was allowed to converge to within 0.0005 eV/unit cell. In terms of the structural parameters shown in Fig. 7-2, l_{11}, l_{12} and l_{22} are the carbon-carbon distances within (l_{11}, l_{12}) and between (l_{22}) phenyl rings, while l_{C-H} is the hydrogen-carbon distance. The parameter p represents the width of the phenyl units, while δ is the angle between l_{C-H} and l_{12} as shown in the figure. In Table 7.1 are listed the calculated values for the structural parameters shown in Fig. 7-2, along with theoretical values obtained by Ambrosch-Draxl *et al.*[4] who also used pseudopotential calculations and experimental values obtained from several sources. Since the structural parameters vary between the two rings in the PPP structural unit cell, I also present the values for l'_{11}, l'_{12}, l'_{22}, l_{C-H}, p' and l'_{C-H} which represent the same distances and angles as described above, but for the second ring. However, the structural parameters for the second *chain* in the 3D PPP unit cell were identical to those for the first within a few hundredths of a percent. The agreement with both previous *ab initio* calculations and experimental results is quite good.

Table 7.1: Ground state structural parameters (see Fig. 7-2 predicted by *ab initio* calculations, along with previously published results and experimental values.

Parameter	This work	Ref. [4]	Expt.[10, 32, 149, 155]
l_{11} (Å)	1.382	1.375	1.356-1.409
l_{12} (Å)	1.407	1.398	1.371-1.425
p(Å)	2.419	2.394	2.342-2.405
l_{C-H} (Å)	1.103	1.100	0.96-1.129
δ (degrees)	120.4	120.5	116-128
l'_{11} (Å)	1.381	1.375	
l'_{12} (Å)	1.404	1.399	
p'(Å)	2.413	2.397	
l'_{C-H} (Å)	1.104	1.100	
δ' (degrees)	118.9	120.3	
l_{22} (Å)	1.450	1.45	

7.4 Approximation of Excited States in PPP

Using the ground state configuration as determined by the relaxation of the ionic and electronic degrees of freedom, the excited state of the molecule can be approximated by removing one electron from the HOMO level and placing it in the LUMO level. This is only an approximation, since this process corresponds to a simultaneous excitation of one electron per unit cell throughout the crystal, and involves only one band-to-band transition. In reality, other bands near the band edges will contribute to the excitation, and the excited states need not be delocalized.

Nonetheless, by studying the forces exerted on the ions as a result of this redistribution of electronic charge, one can get a reasonable idea of which normal modes couple to inter-band transitions. The eigenfrequencies of these modes should then correlate with the vibronic spacings observed in the photoluminescence spectra (see Fig. 3-22) as discussed in section 3.4. In fact, the Franck-Condon relaxation of the ionic coordinates is basically generated by the forces exerted on the ions from the redistribution of charges. The ionic displacements $q_i = R_i - R_i^0$, as described in section

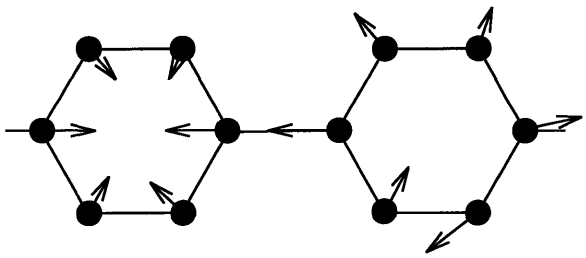

Figure 7-3: Schematic diagram showing the calculated Hellmann-Feynman forces for an excited electronic state acting on carbon atoms in a unit segment of a PPP chain showing the presence of the ~1300 cm^{-1} A_g breathing mode (see text).

3.2.1 (see Eq. 3.9), can then be decomposed into normal modes Q_j, such that

$$q_i(t) = \sum_j a_{ij} Q_j(t) \tag{7.6}$$

describes a sum of normal modes weighted by the a_{ij} (real) amplitudes, and each of the Q_j corresponds to an eigenfrequency ω_j and a complex amplitude β_j where

$$Q_j(t) \equiv \beta_j e^{i\omega_j t}. \tag{7.7}$$

Hence, in terms of the Franck-Condon formalism given in section 3.2.2, the most dominant Q_j (i.e., the mode with the largest $|a_{ij}|$) will represent the normal mode that is most strongly coupled to electronic transitions and determines the vibronic spacings, as depicted in Fig. 3-1.

Figure 7-3 shows the direction of the forces (using Eq. 7.5) acting on the carbon atoms when one electron per unit cell is promoted from the HOMO level to the LUMO level. The average force per carbon atom within each ring is equal to 1.44 eV/Å, while the forces on the hydrogen atoms tend to be almost a factor of 3 less (~0.43 eV/Å). By inspection, and referring to Fig. 3-11 of section 3.3, one can easily see that the A_g breathing mode comprises a strong component of the ionic motions. The fact that the forces lie along directions not completely described by the breathing mode displacements is consistent with the idea that many normal modes are activated by the redistribution of charges. Yet, the weakening of intra-ring bonds by way of promotion of valence electrons from HOMO bonding states to LUMO anti-bonding

states should give rise to a small increase in lattice constants *throughout* the phenyl ring, thus involving a breathing mode motion of carbon ions. This effect is then manifested in the photoluminescence spectra of PPP as the $\sim$ 1300 cm^{-1} vibronic spacing of the 2.5-2.9 eV emission peaks which arise from the breathing mode phonon coupling to electronic transitions.

7.5 Future Work

The forces calculated above for the case of an electronic exited state are proportional to the displacement of the ionic coordinate equilibrium positions following an electronic transition. Therefore, force calculations can be used to directly calculate *ab initio* the Huang-Rhys parameter S, since S is also related to the displacement of normal mode equilibrium positions ΔQ_{eg} through the equation

$$S = \frac{\mu\omega^2}{2\hbar\omega}\Delta Q_{eg}^2 \tag{7.8}$$

which was discussed in section 3.2. The challenge lies in accurately describing the excited electronic state, which could be either localized or delocalized, or involve various different bands within the Brillouin zone. However, to date, no *ab initio* vibronic calculations have ever been reported in the literature, although a large body of work has been established in order to employ more empirical methods[160, 186]. The challenge of accurately applying novel iterative energy minimization techniques and force calculations to organic molecules will remain as a future work, which will be addressed in a future publication[112].

Chapter 8

Application of Disordered Carbons to Li Rechargeable Cells

8.1 Introduction

The purpose of this chapter is to describe the application of disordered carbons and graphite to the technology of rechargeable lithium ion batteries, and to connect the optical and electronic characterization of carbon-based systems to battery performance. In fact, all of the carbons examined in this thesis (except for the ACFs) were initially synthesized with the intent of applying them to electrochemical cells. Although the science of electrochemically-doped graphite is more or less understood under the guise of graphite intercalation compounds (GICs), the insertion process of lithium into disordered carbon is still poorly understood, primarily because of the lack of knowledge of the physical and electronic structure of these materials. Therefore, I attempt in this chapter to relate the development of carbon structures, ordered domain sizes, and defect densities to various electrochemical parameters such as discharge capacity and discharge voltage.

To clarify the important issues in lithium-based rechargeable battery research, I will follow this introduction with a general description of Li-ion cells in section 8.2. Useful definitions and concepts, along with some historical commentary, will also be covered in that section (8.2). Since the physics and chemistry of GICs is relatively

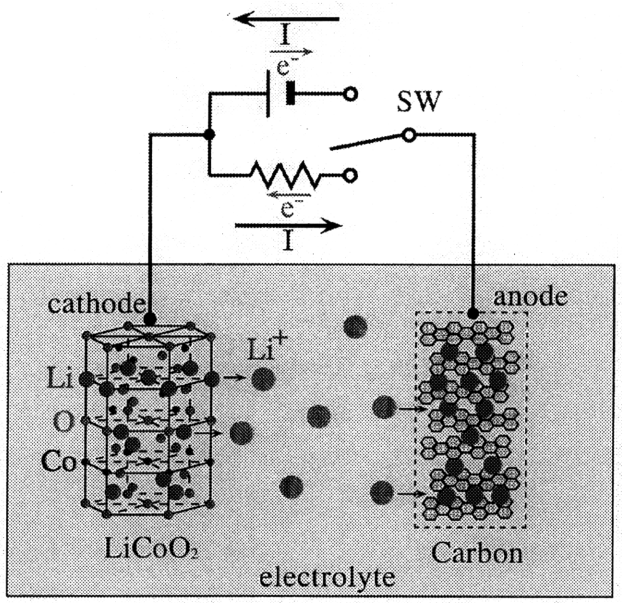

Figure 8-1: Schematic of a typical Li-ion rechargeable battery involving a carbon-based anode.

well established, I continue with section 8.3 which covers GICs and Li-ion cells based on well-ordered (graphitic) anode hosts. This section will thus be particularly useful in understanding the electrochemical attributes of MPCF-based anode hosts, since these materials form well-graphitized systems at high T_{HT}. PPP-based (PPP-700) anodes were recently shown to yield superior Li uptake capability[156] as compared to the GIC/MPCF systems, and the electrochemical properties of PPP-700 as measured by our collaborator Professor M. Endo and co-workers at Shinshu University are thus presented in section 8.4. Finally, in section 8.5, I attempt to correlate the electrochemical properties of PPP-700 and MPCF-3000 with the electronic and optical properties of these materials, which were presented in chapters 3, 4, 5 and 6.

8.2 Li-ion Batteries: A General Description

8.2.1 Basic Principles of Li ion Charge-Discharge Processes

It should be noted that batteries, in general, are among the oldest known electrical devices in Western history. The famous "Voltaic Pile" was first invented by Alessan-

dro Volta in 1792, and later was well-described in 1834 by the electrochemical reaction laws of Michael Faraday[153]. Needless to say, the basic principles of battery chemistry and physics have not changed significantly in the past 200 years, despite the fact that the materials science of batteries remains an active field. Moreover, it can be argued that the science of energy storage has not been sufficiently challenged in recent times, with regard to novel storage mechanisms. Through the years, many types of electrochemical cells have been investigated and commercialized based on various materials (e.g., Lead acid, NiCd, Metal Hydride, etc.,). The lithium ion cell, however, represents the state-of-the-art in small rechargeable batteries and is capable of delivering almost 4 volts with specific energies near 120 Whr/kg[28]. Moreover, the shelf life of Li-ion cells can be quite long while the materials contained in Li-ion cells are essentially harmless to the environment.

Figure 8-1 shows the basic idea of the lithium ion *secondary* battery. A secondary battery is simply one that can be recharged, while a *primary* battery is essentially a "one-shot" device. Li-ion secondary (rechargeable) batteries, like the one shown in Fig. 8-1, are also called "rocking chair" batteries because of the back-and-forth action of Li ions between intercalant hosts. Note that no lithium metal is ever present in such a cell, which is a rather attractive facet of these batteries in terms of safety[28]. As with usual batteries, electrons are transferred from the anode to the cathode during the *discharge* process through an external circuit thereby providing electrical work, while, in the case of Li-ion batteries, electrical neutrality within the cell is ensured by the transfer of Li ions from the anode host to the cathode host via the electrolyte. During the *charge* process the opposite occurs. The total discharge reaction can be written as:

$$Li_xC_6 \longrightarrow Li_{x-\delta x}C_6 + \delta Li^+ + \delta e^- \quad (anode) \tag{8.1}$$

$$\delta Li^+ + \delta e^- + Li_yMO_2 \longrightarrow Li_{y+\delta x}MO_2 \quad (cathode). \tag{8.2}$$

Typical cathode materials are of the stoichiometric form, Li_yMO_2, where M = Mn, Co or W, for example. Detailed pseudopotential calculations have shown that the key attribute of such cathode materials is the ability for oxygen $2p$ and $3s$ states to tightly

bind donated lithium $2s$ electrons during discharge[19]. At the carbon-based anode, the opposite is true, since Li $2s$ electrons donated to the carbon anode π orbitals occupy extended states, as they would in lithium metal. Thus, the basic principle of rocking chair (or any other) battery operation can be described as *electron transfer from extended states at the anode to bound states at the cathode.* The more "free" the extended states are, and the deeper in energy the bound states are, the larger is the difference in the standard voltages between the two electrodes, thus producing a larger overall cell voltage.

8.2.2 Lithiation and Capacity of a Carbon Host Material

Since the studies in this thesis focus on the anode material, I will not discuss the electrochemistry of the cathode further. In fact, the following sections describe the charging and discharging of isolated (half-) cells of Li_xC_6, where the cathode is an inert platinum electrode and the anode is a carbon powder mixed with some inert binder and pressed to form an electrode. The two electrodes are then placed into a conducting ionic solution, typically composed of $LiClO_4$ dissolved in either propylene carbonate (PC) or a 50:50 mixture of ethylene carbonate (EC) and diethyl carbonate (DEC). A current between the anode and cathode producing the opposite reaction to that shown in Eq. 8-1 causes Li ions from the ionic solution to electrochemically dope the carbon material. This charging continues until all the available binding sites in the carbon are filled, at which point the reaction is stopped. The maximum amount of lithium inserted during such a process (per unit mass) is called the *charge capacity* or sometimes the *specific capacity*. Capacity is usually measured in mAh/g, or charge/unit mass, but can be equivalently described in terms of the dimensionless variable x where the charged carbon-based material has the stoichiometry Li_xC_6. In this chapter I use both notations. For example, in graphite-based anodes, the maximum capacity is near 372 mAh/g ($x = 1$), while for carbonaceous materials such as PPP-700 the capacity can be as high as 1100 mAh/g ($x \approx 3$), although this charge capacity is *not* equal to the amount of usable stored lithium.

8.2.3 Reversibility and Passivation

Upon discharging the lithiated carbon, it has been found that not all the lithium charged into the carbon can come out in a reversible fashion. Thus, the *discharge capacity* is usually not equal to the charge capacity over a given cycle, resulting in some of the inserted lithium being permanently or *irreversibly* bound at the anode. This amount of irreversibly stored anodic lithium is called the *irreversible capacity*, while that which can be cycled reversibly is called the *reversible capacity*. Of course, no process is completely reversible, and after continued cycling, the reversible capacity diminishes, and finally falls below reasonable values for battery operation. The number of times a lithium ion cell can be cycled reversibly while maintaining some threshold capacity is called the *cyclability* and this number is sometime used as the cyclability figure of merit. Thus, cyclability and reversibility are two important issues regarding lithium ion battery commercializability.

One source of irreversibility is the formation of a *passivation* layer at the surface of the carbon electrode. This passivation layer forms due to the reaction of the doped lithium and the electrolyte solution. This reaction is driven by the instability of Li-doped carbon in the presence of a non-aqueous solution like PC, which is essentially the same source of instability that Li metal experiences in such an environment. The insoluble reaction products therefore form only at the interface. Since this layer tends to be electrically insulating but ionically conducting, it is sometimes referred to as the *solid electrolyte interphase* (SEI) and, once formed after the first cycle, acts to prevent further electrolyte decomposition. The Li thus stored in the SEI contributes to the irreversible capacity. Other sources of irreversibility arise from any permanent trapping of Li in the carbon, such as the reaction of Li with dangling bonds at the periphery of carbon clusters[131].

8.2.4 Discharge Voltage and Skew

Two other important characterizing parameters are *skew* and *discharge voltage*. These terms refer to plots of cell voltage vs. capacity ($V(x)$ vs. x) as a Li ion cell

is discharged (usually *after* the first cycle). The discharge voltage as a function of capacity x is given by

$$V(x) = -\mu(x)/e \tag{8.3}$$

where $\mu(x)$ is the chemical potential of the Li atom in the carbon host, and e is the magnitude of the electronic charge. By studying the discharge voltage profiles, one can gain important information on the electrochemical state of the lithium-carbon system through measurement of $\mu(x)$. In order for the chemical potential to be meaningful, it must be measured relative to some standard which is almost always chosen as the chemical potential of a Li atom inside Li metal. Thus, the discharge voltage is usually plotted "vs. Li metal" so that a low voltage means that the Li ions feel like they are being plated onto Li metal. Since the purpose of Li-carbon anodes is to replace Li metal (for safety reasons), low discharge voltages are preferred in commercial cells, so that extended ("free") electronic states prevail at the anode, similar to Li metal. If every binding site in the host material were equal in energy at all stages of charging/discharging so that $\mu(x) = \mu_0$, the charge-discharge voltage curves $V(x)$ vs. x (see for example Fig. 8-2) would appear flat in the adiabatic charging limit. This behavior is also favored in commercial systems, since it corresponds to the constant voltage output of a battery cell throughout its discharge lifetime. In reality, however, the chemical potential changes with capacity ($\partial\mu(x)/\partial x \neq 0$) leading to a *skew* in the voltage discharge curve. Thus, beside providing a highly reversible capacity and high cyclability, the ideal Li-carbon anode should display a flat discharge voltage ($V(x)$ vs. x) with values of $V(x)$ near zero vs. Li metal.

8.3 Graphite Intercalation Compounds

Graphite Intercalation Compounds (GICs) generally have no problem in providing extended states to the anode system and thus they have low discharge voltages due to their well-ordered and semi-metallic properties. Moreover, due to their high symmetry, lithium intercalation binding sites are very uniform in energy, leading to a very flat discharge curve with little skew. However, an additional type of feature appears

in the charge-discharge curves of staged compounds, due to the coexistence of phases at a given capacity value. As we will see below, when the chemical potential $\mu(x)$ of two given phases become equal as x is varied, a lower ionic resistance is encountered due to the sudden access of new staging sites which produces "plateaus" in the $V(x)$ vs. x curves. These plateaus can be vividly identified by plotting the so called differential capacitance $\pm \mathrm{d}x/\mathrm{d}V$ vs. V for charging (-$\mathrm{d}x/\mathrm{d}V$) and discharging (+$\mathrm{d}x/\mathrm{d}V$). The differential capacitance of a GIC-based cell is shown in the inset of Fig. 8-2 where the the sharp peaks in $\mathrm{d}x/\mathrm{d}V$ vs. V correspond to the small steps (marked with solid dots) in the $V(x)$ vs. x curve of Fig. 8-2.

X-ray absorption spectroscopy (XAS) experiments[27] have demonstrated that in the low-doping limit, $\mathrm{d}x/\mathrm{d}V$ plotted versus $\mu(x)$ closely resembles the XAS absorption curve versus photon energy. In the XAS experiment, a photon is used to eject a core electron, transferring it to an unoccupied state in the conduction band, leaving a tightly bound hole which is screened much in the same manner as an Li ion would be screened by the same conduction band states in Li-GICs. Although short lived, these conduction band electrons are still believed to effectively screen the hole[107]. Therefore, taking into account the same screening effect, the filling of conduction band states with electrochemically transferred electrons should probe the same density of unoccupied states as in the XAS experiment. The correlation of the two experiments is described in detail in ref. [27]. The main thing to emphasis here is the physical insight that the differential capacitance curves strongly reflect the density of states $N(E)$ above the Fermi level, while being modulated by Li-Li interactions that give rise to staging.

MPCFs heat-treated to T_{HT}=3000°C contain large crystallites that have electronic properties similar to graphite, as we have shown in chapters 3 and 6. Therefore, in addition to GIC-based cells, we examine here (see §8.3.2) the charge-discharge curves (and differential capacitance curves) for undoped and B-doped MPCFs. The charge-discharge curves and associated differential capacity curves for these samples are expected to resemble those of typical GICs.

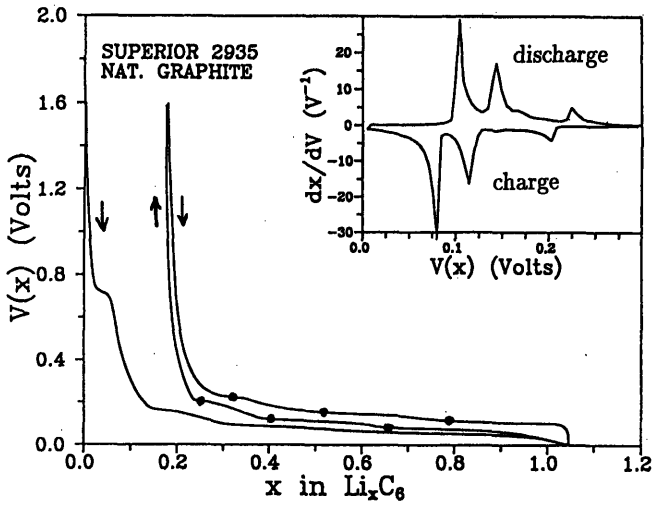

Figure 8-2: Charge-discharge curves for a typical Li-GIC sample based on natural graphite (adapted from ref.[28]). The inset shows the differential capacitance $\mathrm{d}x/\mathrm{d}V$, which is defined as the inverse first derivative of the main plot $V(x)$ vs. x, showing peaks which correspond to phase transitions between the various phases in a GIC system. The three peaks $\mathrm{d}x/\mathrm{d}V$ can be correlated with the steps in $V(x)$ vs. x marked by solid dots along the charge ($\downarrow$) and discharge($\uparrow$)[28] of the second cycle (the right-most two curves in the main figure).

8.3.1 Phase diagram of $\mathrm{Li}_x\mathrm{C}_6$

The fact that the discharge curves (see Fig. 8-2) of Li-GIC cells show very little skew is favorable in terms of device applications, since discharging at a constant voltage (vs. Li metal) which is small, is typically preferred. Figure 8-2 shows both the voltage profile and the differential capacitance curves for a graphite-based Li-carbon cell. The voltage profiles show a series of small plateaus in $V(x)$ vs. x, which correspond to peaks in the differential capacitance. Note that the second charging of the graphite begins at a higher initial capacitance x due to the SEI (solid electrolyte interface) so that the irreversible capacity ($\sim$0.2 or 74 mAh/g) can be directly evaluated as the shift along the x-axis of the 1st and 2nd cycles. It has been shown[30] that the plateaus occurring below 0.5 V correspond to phase coexistence of GICs of various stages (except for the shoulder in the first charging near 0.7 V, which is due to electrolyte decomposition).

By studying the *in situ* XRD profiles as a function of x, Dahn[30] was able to construct the phase diagram for electrochemically doped GICs at ambient temperatures.

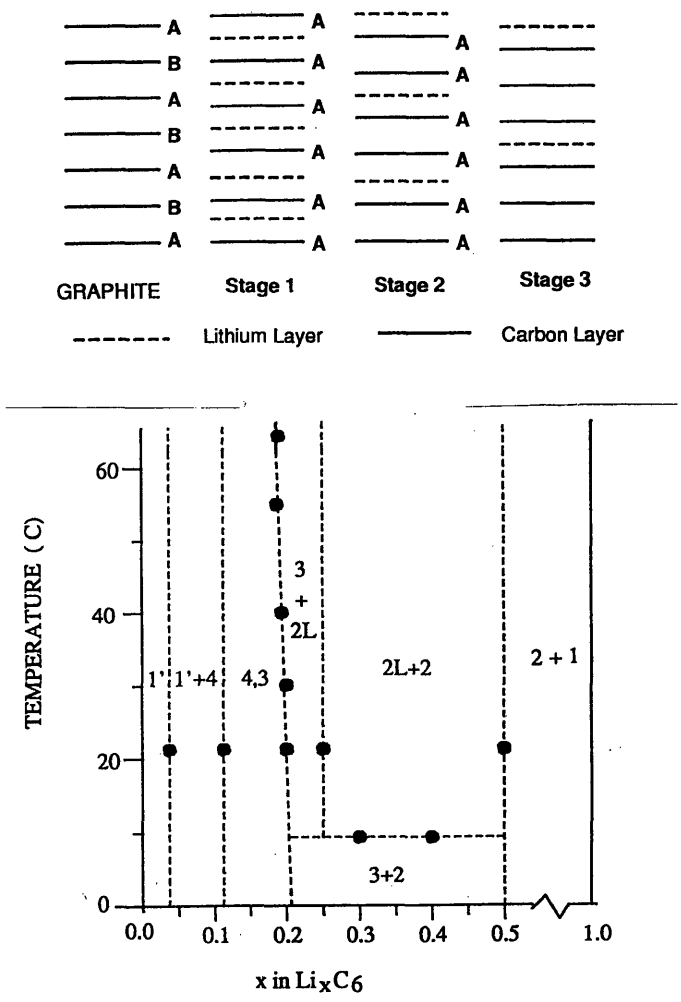

Figure 8-3: Staging behavior of Li_xC_6 systems (top) with the corresponding phase diagram (bottom) plotted as temperature vs. x in Li_xC_6. The numbers in the phase diagram refer to the dominant stage observed at that temperature based on XRD data; 1' refers to a *dilute* stage 1 compound, whereas 2L refers to that of a liquid-like stage 2. The "addition" of phases indicates that XRD measurements were able to clearly identify the coexistence of both phases, while for the case of the "4,3" phase, a coexistence of phases could not be confirmed[30].

Figure 8-3 shows the schematic of GIC staging along with the Li_xC_6 phase diagram derived from Dahn's XRD studies. Upon intercalation, the ABAB..., stacking of graphene layers changes to AAA... while the Li ions occupy $\sqrt{3} \times \sqrt{3}$ superlattice sites above and below carbon hexagon rings. Thus the features in the charge-discharge curves of Fig. 8-2 directly relate to the phase of the GIC and the various stages produced during intercalation.

Specifically, during the electrochemical intercalation of Li into a well-ordered graphite host, the Li_xC_6 system first forms a dilute stage-1 GIC (denoted in Fig. 8-3 as 1'), where Li ions are uniformly distributed among all $\sqrt{3} \times \sqrt{3}$ sites, but with a low probability for occupation. As the density of the Li species increases, long-range correlations begin to induce an ordered stage-4 arrangement intermingled with the dilute stage-1 (denoted by $1' + 4$ in Fig. 8-3). Above $x \approx 0.12$, a stage-3 compound probably forms with some amount of stage-4, but a clear coexistence of phases in this case was not detectable by XRD[30], while above $x = 0.2$ a liquid-like stage-2 ("2L") forms. For some values of T and x, an ordered stage-2 forms, coexisting with either a stage 2L or a stage-3 phase, and then finally, above $x = 0.5$, a stage-1 GIC forms with the stoichiometry LiC_6[30]. Note that phases are typically intermingled with one another and that only at the highest or lowest Li concentrations are single phases observed.

8.3.2 MPCFs and the Effect of Boron doping

The charge-discharge curves associated with Li-intercalated milled MPCFs ($T_{HT} =$ 3000°C) are shown in Fig. 8-4. Note the similarity of Fig. 8-4 to Fig. 8-2 in terms of staging, which is due to the well-ordered nature of the MPCF-3000 system. We have seen that both the Raman spectrum and the diamagnetic susceptibility of samples such as MPCF-3000 are substantially modified by boron doping. Namely, B-doped samples are expected to have lower Fermi levels E_F due to the acceptor action of substitutionally inserted boron, thus decreasing the magnitude of χ_{dia} (see sect. 6-4). Likewise, boron doping tends to shift the E_{2g_2} Raman mode and to lower the ratio $R(\lambda) = I_D/I_G$ of the high-T_{HT} MPCF- and PPP-based carbons. Interestingly,

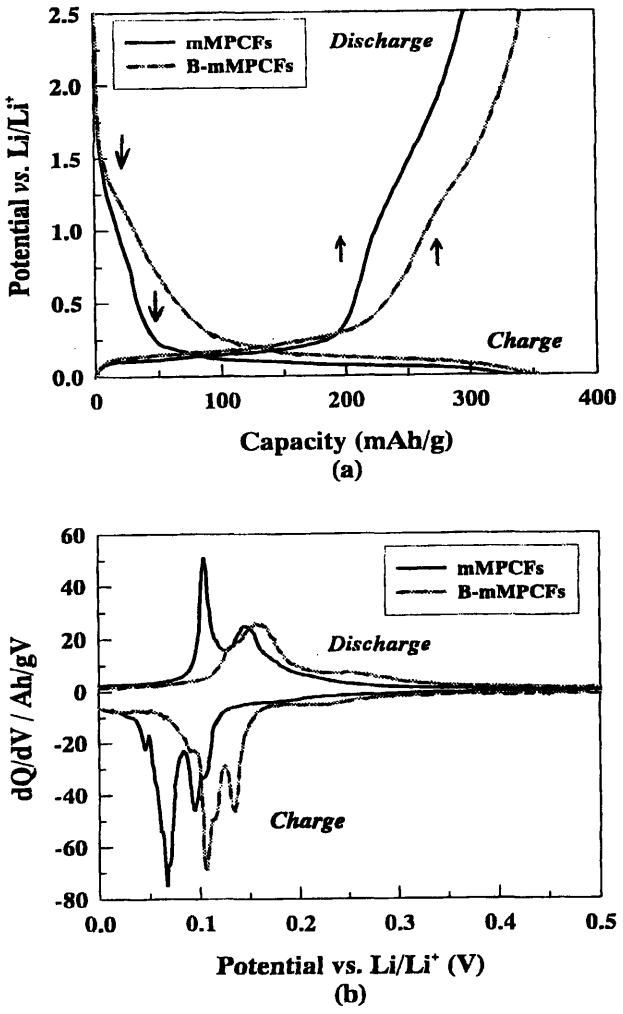

Figure 8-4: Second cycle charge-discharge curves plotted as Potential $V(x)$ vs. Capacity (a) and differential discharge curves (b) of a milled mesophase pitch carbon fiber (MPCF)-based Li ion cell using undoped (solid) and ~2-3% B-doped (dashed) MPCFs[41]. For clarity, the discharge curves of (a) are inverted relative to the charge curves so that instead of going from ~350 mAh/g ($x \sim 0.94$) to ~0 mAh/g as shown in Fig. 8-2, the discharge curves are shown going in the opposite direction (from 0 to ~350 mAh/g). Note that the addition of boron increases the discharge capacity.

although substitutional boron is expected to increase in-plane phonon scattering and enhance the D peak, the decrease in electron density between graphitic layers causes the inter-planar distance ($c_0/2$) to decrease[104] which can enhance the interlayer "registry" of atoms involved in graphitization.

A decrease in c_0 would tend to decrease the average graphite-intercalant distance thereby strengthening the bond between the two. This increase in binding, could then partially overcome the ion-ion repulsion of Li ions (which ultimately limits the stoichiometry to x=1) thus allowing for more Li to intercalate, although the enhanced binding should increase $V(x)$. Figure 8-4 shows the second-cycle charge-discharge curves for MPCF and B-doped MPCF at a charging rate of 30 mA/g-carbon. A clear increase in capacity at a constant potential is observed for the discharge cycle upon boron addition, along with an increase in charging voltage at a constant capacity for the B-doped MPCF versus the undoped fibers. Since MPCFs are known to maintain a finite amount of disorder even at the highest T_{HT} (see Fig. 3-15), the sharp staging effects observed in the $\mathrm{d}x/\mathrm{d}V$ curves of Fig.8-2 are somewhat broadened. The suppression of staging due to modest disorder has been studied in depth by Zheng and Dahn[26, 195] for heat-treated coke-based carbons, and will be considered for case of extreme disorder in the next section.

8.4 Lithium Insertion into PPP-based Carbons

The preceding section (§8.3) reviewed an area of battery electrochemistry that has been well described experimentally and theoretically in the literature over the past three decades[28, 37, 52]. However, only in the last decade or so has the electrochemistry of Lithium/disordered carbon systems been investigated. Interest in this new field came after the observation that a substantial increase in discharge capacity can be obtained from so-called hard carbons heat-treated below 1000°C.

This increase, in fact, is *not* unique to PPP-based carbons, although one of the first reports of this capacity increase in disordered carbons was due to PPP-700[156]. Figure 8-5 shows the discharge capacities found in a few high-capacity/low-T_{HT} carbon

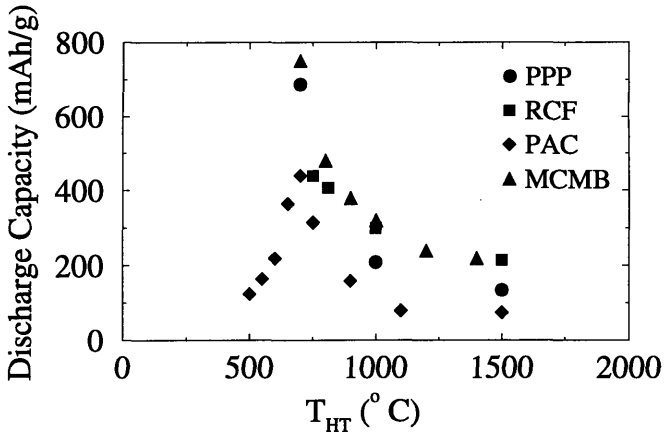

Figure 8-5: Second cycle discharge capacities observed in a variety of low-T_{HT} carbons showing a maximum at T_{HT}=700°C [44, 72, 105, 111].

systems, namely PPP[44], ribbon-like pitch-based carbon films (RCF)[111], phenol-formaldehyde resin-based "polyacenic" (PAC) carbons[72], and coal-tar pitch-based mesocarbon microbeads (MCMB)[105]. It is clear that all of the carbons shown in Fig. 8-5 have a maximum discharge capacity near T_{HT}=700°C. Although not shown, the discharge capacities of PPP-based carbons with $T_{HT} < 700$°C were all below 500 mAh/g. Due to the large amount of disorder in low-T_{HT} carbons, lithium ions are believed to bind to graphene ribbons such that two $\sqrt{3} \times \sqrt{3}$ layers of Li bind to each *single* graphene ribbon[102] (see Fig. 8-6). Thus, for disordered carbons, there will be two layers of Li atoms for every single layer of graphene ribbon, resulting in a higher lithium to carbon ratio as compared to first-stage GICs, as can be seen in Fig. 8-6.

Furthermore, an increase in the number of edge sites in low-T_{HT} disordered carbons could also increase the amount of lithium doping that is possible. However, the precise doping mechanism and associated Li binding sites are presently not well understood, primarily because the structure of low-T_{HT} carbons is highly disordered and quite complex.

Figure 8-7 shows a charge-discharge curve for PPP-700. No clear plateau structures in the voltage range $0< V(x) < 0.5$ V are observed in the trace, implying that staging effects are not at work in these systems, although a shoulder in the discharge curves near 1 V gives rise to broad peaks in the differential capacitance. However,

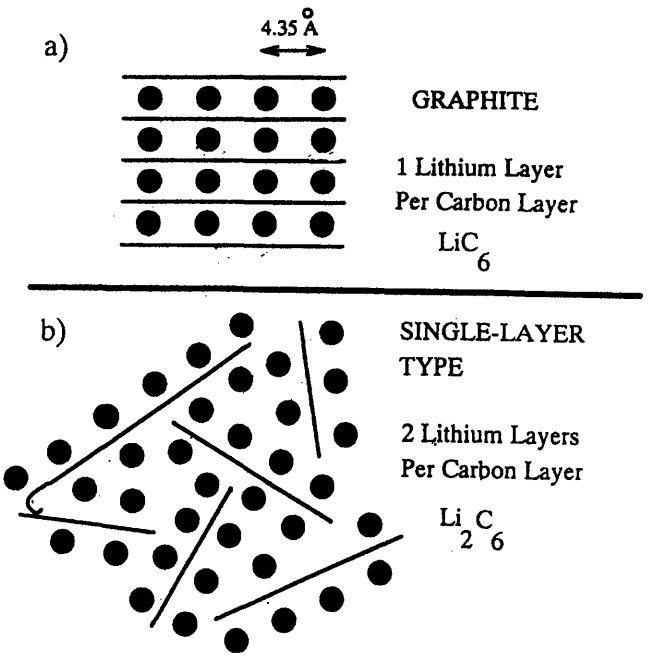

Figure 8-6: Schematic diagram showing the insertion of lithium into (a) graphitic structures and (b) single-layer hard (non-graphitizing) carbon structures. The nearest-neighbor Li-Li distance is 4.35 Å in both examples[102].

instead of differential capacity, I show in Fig. 8-7(b) the current vs. voltage of a cyclic voltammogram (CV) which is directly proportional to dx/dV. Note that the voltage profile of Fig. 8-7(a) is not flat, and this arises because of the "non-degenerate" binding sites where each lithium ion is discharged at a different chemical potential. The average discharge potential (vs. Li metal) is higher as well for the case of PPP-700 as compared to the GIC system. Thus, as in the B-doped case, a trade off is observed between higher Li uptake and voltage characteristics. In terms of irreversibility, PPP-700 samples also suffer a large irreversible capacity ($\sim$700 mAh/g) which is shown as the difference between the first and second discharges of Fig. 8-7 (drawn as solid and dashed lines, respectively). Nonetheless, a reversible capacity of about 680 mAh/g is observed in the second cycle which is almost twice the capacity of conventional Li-GICs.

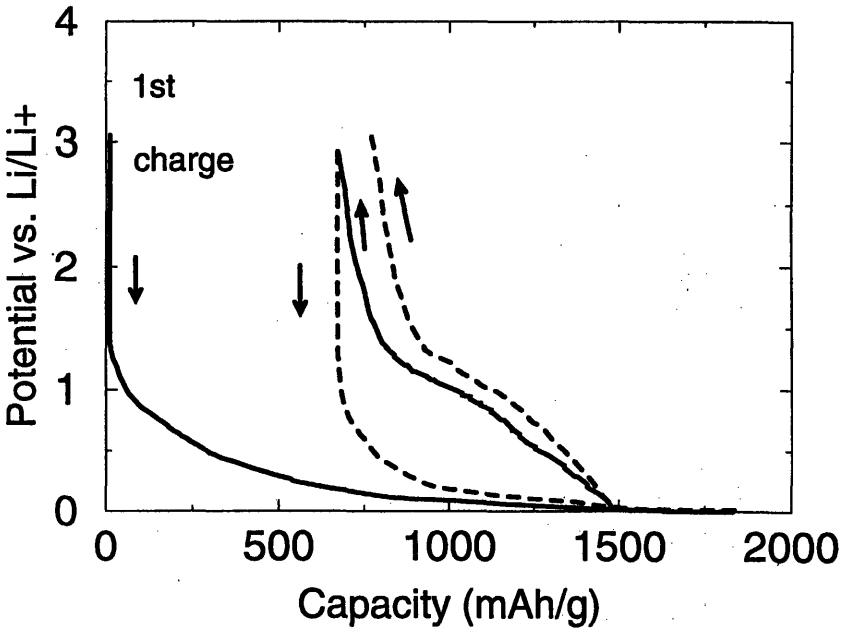

(a)

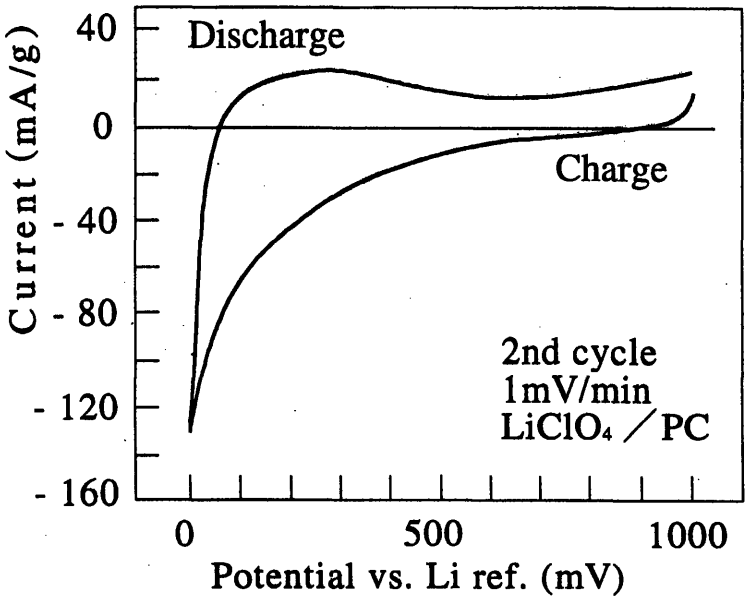

(b)

Figure 8-7: Charge-discharge curves (a) and CV (cyclic voltammogram) curve (b) for a Li/PPP-700 cell during the first (solid lines) and second (dashed lines) cycles, showing the compromise between increased capacity and increased voltage allowed by such disordered-carbon-based cells[44, 145]. The features in the CV curve of (b) are essentially the same as those in the dx/dV curves (not shown).

8.5 Model for Li Uptake in Disordered Carbons

The discharge capacity behavior for PPP-based carbons as a function of T_{HT} can be understood by considering the results of experiments described in previous chapters. Firstly, elemental analysis (see Fig. 2-3) showed that T_{HT}=700°C represents the threshold for hydrogen evolution. That is, at this T_{HT}, hydrogen can be dissociated from the PPP backbone, leaving a dangling σ-bond in its absence. However, since this dangling bond is highly reactive, cross-linking occurs, creating small condensed ring structures that have a finite amount of hydrogen (H/C $\sim$ 0.3) at edge sites. These condensed ring structures are, in fact, the localization sites that account for the VRH conductivity discussed in section 5.3. Thus, for T_{HT} lower than 700°C, the bulk conductivity of the samples ($\leq 10^{-11}$ S/cm) is not sufficient to provide adequate charging, due to the insulating action of PPP. Therefore, to achieve sufficient conductivity for the charging process, it is necessary to increase T_{HT} to values equal to or above 700°C.

Although the conductivity of PPP-based samples continues to increase for T_{HT} values above 700°C (see inset of Fig. 5-5), we note that the system actually gets *more* disordered in the T_{HT} range $700 < T_{HT} < 1000$°C. This increased disorder can be inferred from the increase in Raman linewidths displayed in Table 3.1 over this T_{HT} range, and the large value of the localized spin density $N_{\rm loc}$ ($\sim$ 1 spin per 800 carbons) displayed in Fig. 6-2. Thus, maximum disorder does not correspond to maximum Li uptake.

Saito *et al.*[131] performed unrestricted Hartree-Fock calculations to show that in the case of C_{96} aromatic carbon clusters with dangling bonds, lithium atoms tend to covalently bond *irreversibly* to the unpaired edge sites, whereas hydrogen-terminated clusters of the same size tend to bind Li reversibly in the π orbitals. Therefore, in the T_{HT} regime where the carbon host is conducting, the amount of irreversibly bound Li should scale roughly with the number of dangling bonds. Alternatively, the reversibly doped Li should show a proportionality with hydrogen content. This proportionality, in fact, was first noted by Dahn *et al.*[29] by examining a set of carbonaceous samples,

all heat-treated above 700°C, thus showing a linear dependence of discharge capacity on the amount of hydrogen remaining in the carbonaceous samples.

As T_{HT} increases above 1000°C, where the localized spin density drops below 1×10^{19} spins/g and the in-plane crystallite size grows to roughly 50 Å, one might expect an increase in discharge capacity due to an increase in the number of reversible binding sites. However, as XRD shows (see Fig. 2-4), the inter-planar distance starts to approach that of turbostratic graphite, thereby preventing the binding of Li to either side of *single* graphene layers (Fig. 8-6). At higher T_{HT}, the discharge capacity is expected to increase again, as the carbon becomes well ordered and doping is by way of intercalation thereby forming a GIC.

The electrochemical characteristics of carbon-based anodes can then be summarized as follows. In well-ordered systems, lithium insertion is limited to a discharge capacity of ~372 mAh/g (LiC_6) due to ion-ion repulsions, which can be partially overcome in substitutionally B-doped systems. The discharge voltage is flat and close to zero (vs. Li metal), which is credited to the translational symmetry of the chemical potential and the semi-metallic bands of graphite, respectively. A higher capacity is observed in certain low-T_{HT} systems, due to the increased likelihood of binding Li ions to either side of a given graphene sheet. However, because of the disorder necessary to allow for such a disordered single-sheet arrangement, binding sites are no longer translationally invariant, thereby producing a slope to the discharge curves which is typically not as close to zero (vs. Li metal) as is their GIC counterpart.

8.6 Future Work

Because of the close relation of the density of states $N(E)$ above E_F to the Li insertion process, future work should focus on identifying the nature of unoccupied states in disordered carbons. Transport experiments performed in this thesis were used to evaluate the large density of states near E_F using hopping models (see §5.3) since carrier conduction is strongly dependent on $N(E_F)$. Photoconductivity experiments, as were used to study carbon aerogels[148], could be used to excite electrons near E_F

and probe the density of hole and electron states away from E_F. One should then, in principle, be able to connect the general features of dx/dV to the photo-current.

Chapter 9

Conclusions

9.1 Summary

Since a description of future work has been given at the end of each chapter, this chapter simply serves to draw a few conclusions based on the findings of this thesis work. To reiterate, the goal of this thesis was to gain a better understanding of the influence of structural disorder introduced by heat-treatment on the electronic and optical properties of various carbon-based materials. Particular emphasis was placed on PPP-based carbons, and these materials were, in fact, studied from a T_{HT} regime in which the pristine precursor (polymer) was abundant, to one where a purely carbon structure structure is formed, which could be compared with graphitic materials only on a local scale.

In terms of the PPP polymer, the vibronic states of the ground state pristine polymer were probed to reveal a change in the Huang-Rhys parameter, S, as T_{HT} increased to 650°C which is due to an increase in local disorder. This disorder in PPP structure was also evidence by relative changes in the quinoid/benzenoid content, and the quinoid form appeared to be an intermediate step in the carbonization of PPP. At T_{HT} values above 700°C, Raman scattering studies of disordered-induced phonons in both PPP- and MPCF-based carbons allowed for an approximation of the in-plane crystallite size L_a, and this parameter was then used to evaluate the ordered domain sizes. L_a was shown to strongly influence both the transport and magnetic properties

of these systems.

Specifically, I showed that the magnitude of diamagnetism of disordered carbon structures based on PPP and MPCF could be modeled using London-Hoarau theory for L_a values less than ~120 Å to yield 2D graphene ribbon sizes L that could be correlated with the in plane crystallite size. Although the high-T (200-300 K) dependence of $\chi(T)$ was not well accounted for by the theory, the close correspondence of carbon cluster size and $\chi(T \approx 0)$ imply that the London formalism may be more appropriate than that derived by McClure for small domain sizes. For the larger L_a (>200 Å) encountered in the MPCF-3000 samples, London-Hoarau theory fails to accurately take into account the folded-ribbon structure, which led me to analyze the MPCF-3000 $\chi(T)$ data using the McClure-Hickman theory thus giving reasonable results. Furthermore, the large diamagnetic anisotropy $|\chi_\perp - \chi_{||}| \approx 10$ of the MPCF-3000 made possible interesting alignment effects, which could easily be understood using a simple geometrical model.

The ESR measurements focused on PPP-based carbon heat-treated near $T_{HT} =$ 700°C, both because of the technological application of PPP-700 as described in chapter 8, but also in order to study the effect of molecular/atomic rearrangement produced by carbonization. As was shown, the localized spin density N_{loc} experiences a maximum near carbonization temperatures due to radical formation, and these spins were then used to probe the local environment. A trapped polaron model, in which a charged quinoid-like defect that could slowly hop along a PPP chain, was used to explain the behavior of $\Delta H_{pp}(T)$ with T for precarbonized PPP (PPP-650 and PPP700), while hopping between conducting grains appeared to be more important to ESR line broadening mechanisms in PPP-750. Such a hopping behavior was also investigated by studying the electronic transport of these low-T_{HT} systems, again showing that the changes in electronic properties caused by heat treatment were directly related to the development of graphene/aromatic clusters and thus on in plane crystallite dimensions of graphene ribbons.

The carbonaceous PPP-based structures formed at low-T_{HT} were thus shown to possess novel properties which could be attributed to defective polymeric structures

that apparently resembled both PPP and disordered carbon. The investigation of low-T_{HT} PPP have allowed for new insight into the carbonization process and Li-rechargeable cells based on disordered carbon.

Appendix A

Approximation of Resonance Raman Intensities

When the laser energy, E_L, is much less than the energy gap, E_0, an approximate form for the resonance Raman polarizability tensor (equation 3.18)

$$(\alpha_{\rho\lambda})_{I\to F} = \sum_V \frac{\langle F|m_\rho|V\rangle\langle V|m_\lambda|I\rangle}{E_V - E_I - E_L - i\Gamma} + \frac{\langle F|m_\lambda|V\rangle\langle V|m_\rho|I\rangle}{E_V - E_F + E_L - i\Gamma} \tag{A.1}$$

can be found by considering only the lowest vibronic level in the electronic excited state as a virtual state (see Fig. A-1). Since we are considering an off-resonance transition, we must consider both terms in Eq. 3.18. However, we make the simplifying assumption that the electronic dipole operators are isotropic ($\rho = \lambda$) and that the adiabatic approximation is valid. Thus, the electronic-vibronic matrix elements can be written as Born-Oppenheimer states connected by an isotropic dipole operator m ($=m_\rho = m_\lambda$):

$$\begin{aligned}\langle F|m|V\rangle\langle V|m|I\rangle &= \langle\psi^{(g)}|m|\psi^{(ex)}\rangle\langle\psi^{(ex)}|m|\psi^{(g)}\rangle\langle\phi^{(g)}(1)|\phi^{(ex)}(0)\rangle\langle\phi^{(ex)}(0)|\phi^{(g)}(0)\rangle \\ &= M^2(Q)\langle 1|0\rangle\langle 0|0\rangle. \end{aligned} \tag{A.2}$$

In the above equation, the Franck-Condon matrix elements, $\langle m|0\rangle$ are written in terms of phonon occupation numbers, and are assumed to be real. Since we are considering

only one phonon excitation (i.e., the initial state has zero phonons and the final state has one), the energies in the denominator of Eq. A.1 can be written as

$$E_V - E_I = E_0 \tag{A.3}$$

$$E_V - E_F = E_V - E_I - \hbar\omega_{ph} = E_0 - \hbar\omega_{ph} \tag{A.4}$$

where $\hbar\omega_{ph}$ is the energy of the excited phonon. The isotropic polarizability then becomes:

$$\alpha = M^2(Q)\langle 1|0\rangle\langle 0|0\rangle \left(\frac{1}{E_0 - E_L - i\Gamma} + \frac{1}{E_0 + E_L - \hbar\omega_{ph} - i\Gamma}\right) \tag{A.5}$$

where Γ is the homogeneous electronic linewidth or (inverse) "lifetime" of excited states. Squaring the above equation finally gives

$$I \approx M^4(Q)|\langle 1|0\rangle|^2|\langle 0|0\rangle|^2 \left(\frac{(2E_0 - \hbar\omega_{ph})^2 + 3\Gamma^2}{[(E_0 - E_L)^2 + \Gamma^2][(E_0 + E_L - \hbar\omega_{ph})^2 + \Gamma^2]}\right) \tag{A.6}$$

In order to derive an approximate form for the ratio of integrated line intensities of various Raman modes in the spectrum of PPP, we note that $\hbar\omega_{ph}, \Gamma \ll E_L, E_0$ where $E_L < E_0$. Keeping terms linear in $\hbar\omega_{ph}$ and denoting $\varepsilon_1, \varepsilon_2$ as the energies of the two phonons we wish to compare, the ratio of the squares of the polarizabilities is given by

$$\frac{\alpha_1^2}{\alpha_2^2} \approx \kappa \left(1 + \frac{(\varepsilon_1 - \varepsilon_2)}{E_0}\left[\frac{E_0 - E_L}{E_0 + E_L}\right]\right) \tag{A.7}$$

where κ is the ratio of the Franck-Condon factors for each vibronic spacing given by

$$\kappa = \frac{(|\langle 1|0\rangle|^2|\langle 0|0\rangle|^2)_1}{(|\langle 1|0\rangle|^2|\langle 0|0\rangle|^2)_2}. \tag{A.8}$$

If we can describe the wavefunction overlaps of each phonon by individual Huang-Rhys parameters (as given by Eq. 3.15) such that the Franck-Condon factors become

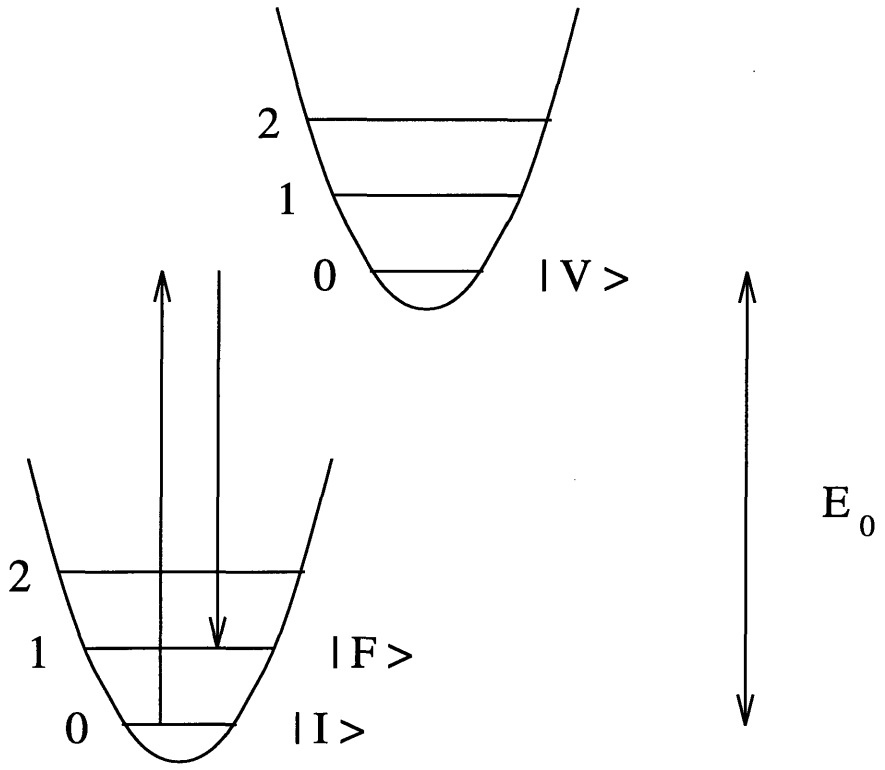

Figure A-1: Excitation of one phonon via electronic transitions near the electronic absorption edge.

$|\langle 1|0\rangle|_i^2 = S_i e^{-S_i}$ and $|\langle 0|0\rangle|_i^2 = e^{-S_i}$ $(i = 1, 2)$, we find that

$$\kappa = \left(\frac{S_1}{S_2}\right) e^{-2(S_1 - S_2)} \tag{A.9}$$

yielding for the ratio of Raman intensities as a function of laser energy,

$$\frac{I_1}{I_2} = \left(\frac{S_1}{S_2}\right) e^{-2(S_1 - S_2)} \left(1 + \frac{(\varepsilon_1 - \varepsilon_2)}{E_0} \left[\frac{E_0 - E_L}{E_0 + E_L}\right]\right). \tag{A.10}$$

Thus, the general result is that the lower frequency phonon intensity increases with increasing laser energy, as compared to the higher frequency phonon. As E_L approaches E_0, however, we expect higher lying virtual states to contribute so that an expression more complete than Eq. A.10 is needed.

Appendix B

Modification of the Knight Formula for Variable E_L

Tuinstra and Koenig[179] first noted that the ratio of the integrated Raman intensity of the so-called disorder-induced (D) peak to that of the symmetry-allowed E_{2g_2} (G) peak scaled almost linearly with the lateral crystallite dimension, L_a, of graphite systems. Knight and White[80] later summarized the Raman spectra of various carbon systems measured at 514.5 nm ranging from coke and burnt wood, to diamond-like thin films and pyrolytic graphite.

They thus derived an empirical relationship between the $R = I_D/I_G$ ratio and the in-plane crystallite size L_a as determined by x-ray diffraction:

$$L_a = 44\frac{I_D}{I_G}^{-1} = \frac{44}{R}\mathring{A}. \tag{B.1}$$

However, since R for graphitic systems has been found to be laser wavelength dependent[9, 121, 184] for a given sample, the above equation should hold only for λ=514.5 nm. This laser wavelength dependence is intimately related to the resonant behavior of Raman lines in graphitic systems, which also produces frequency dispersion in the D and G' bands.

The dependence of I_D/I_G on laser frequency has been extensively discussed in the past and attributed to a modest decrease in I_D, but a stronger increase in I_G with

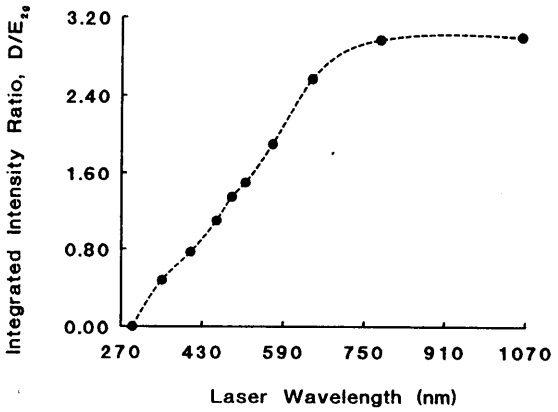

Figure B-1: Plot of I_D/I_G vs. laser wavelength for glassy carbon heat-treated to T_{HT}=2000°C (Wang *et al.*).

increasing laser energy for a variety of carbon samples.[9, 108, 121, 147, 165, 181, 184] The strong increase in I_G is due to a singularity in the dielectric function $\epsilon(\omega)$ vs. frequency as the photon energies approach the $\sigma - \sigma^*$ transition near 4.5 eV.[165, 175] This singularity thus produces a maxima in the Raman scattering efficiency which is proportional to $|\partial\epsilon(\omega)/\partial\omega|^2$.[18]

For the problem of modifying the Knight formula, we first caution that this formula is empirical, since XRD primarily probes lateral dimensions, while R is related to the amount of graphene edges in the sample. Nonetheless, for L_a fixed versus λ we have

$$L_a = C(\lambda)R^{-1}(\lambda) \tag{B.2}$$

where $C(\lambda)$ is a variable scaling coefficient such that $C(514.5\text{nm}) \approx 44$ Å. In order to estimate the appropriate $C(\lambda)$ for a given wavelength (in nm), we note that Wang *et al.*[184] measured R vs. λ for the case of glassy carbon heat-treated to 2000°C (see Fig. B-1), and found a roughly linear relationship in the (visible) wavelength regime $400 < \lambda < 700$ nm which can be given as

$$R = R_0 + \lambda R_1 \tag{B.3}$$

where $R_0 = -2.30$ and $R_1 = 0.00745$ nm^{-1}. The L_a value in this study was estimated using Eq. 1 to be 29 Å. Thus, we could estimate the empirical form of $C(\lambda)$ (given

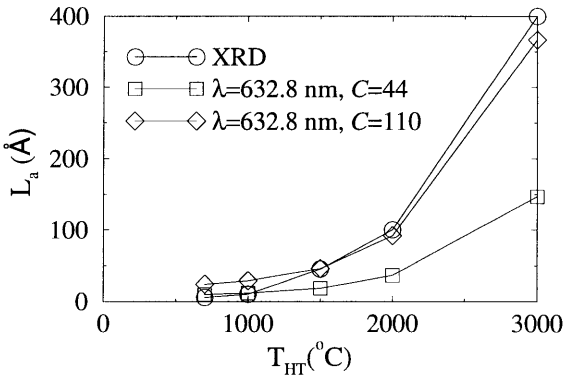

Figure B-2: Plot of L_a vs. T_{HT} for MPCF as determined by: XRD data ($\circ$), Raman data at 632.8 nm, using the unmodified Knight formula ($\square$), and the same data using $C(\lambda)$=110 ($\diamond$).

in Å) to be $C(\lambda) = -67 + 0.22\lambda$. However, in all fairness, we should consider the form of $R(\lambda)$ found in other studies and take some sort of average. Baranov *et al.*[9] measured $R(\lambda)$ vs. λ yielding again a roughly linear relationship with $R_0 = -2.22$ and $R_1 = 0.00769\ \text{nm}^{-1}$ for glassy carbon samples heat treated to 3000°C with L_a=54 Å (as measured by XRD). Mernagh *et al.* also measured such a relationship for the case of 'Graphon' carbon black, but the form of $R(\lambda)$ in that case turned out to be nonlinear.[121] In fact, in that study, the absolute intensity of the I_D and I_G peaks was measured (referenced to $\nu(SO_4^{2-})$) resulting in I_D increasing with increasing λ while I_G showed an almost random behavior. From a theoretical standpoint, such a dependence is difficult to understand; we therefore average only the results of Ref. [184] and [9] to arrive at

$$\bar{C}(\lambda) = -93 + 0.32\lambda. \tag{B.4}$$

As a comparison, we estimated the Knight constant to be approximately 110 for λ=632.8 nm and used Eq. 1 to estimate L_a for the case of milled mesophase pitch-based carbon fibers (mMPCFs) over a wide T_{HT} range. In Fig. B-2 we show the L_a of mMPCFs as estimated from our formulas, L_a as estimated from the unmodified Knight formula, and L_a as determined by XRD using Scherrer's formula. From the plot, one can see the excellent agreement with the modified prediction and XRD data (except for low-T_{HT} data where the formula is expected to break down), while the

unmodified Knight formula (C=44) shows a large discrepancy.

Appendix C

London-Hoarau Theory for Diamagnetism of Pregraphitic Carbons

The formalism developed by London[103] to calculate the large diamagnetic anisotropy of several aromatic hydrocarbons was later extended by Chausse, Hoarau and Volpilhac[20, 69] to describe the diamagnetism of pregraphitic carbons that could be modeled as non-interacting 2D graphene sheets. In London's theory, the molecular orbitals Φ of the π electrons are expanded in terms of atomic orbitals ϕ_r^0, such that

$$\Phi = \sum_r C_r \phi_r^0 \exp(ie\vec{A}_r \cdot \vec{\rho}/\hbar c), \tag{C.1}$$

where $\vec{A}_r$ is the vector potential at the nuclear position of the rth atom and $\vec{\rho}$ is the electronic radius vector. Minimization of the Hückel molecular-orbital energy leads to the secular equation

$$C_r(\alpha_r - E) + \sum_s C_s \beta_{rs} = 0 \tag{C.2}$$

where

$$\alpha_r = \alpha_r^0 - \frac{1}{2}\chi_r^0 H^2 \tag{C.3}$$

$$\beta_{rs} = \beta_{rs}^0 \exp\left(\frac{ie}{2\hbar c}(\vec{A}_s - \vec{A}_r) \cdot (\vec{\rho_r} + \vec{\rho_s})\right). \tag{C.4}$$

In the above equations, α_r^0 and β_{rs}^0 are the Coulombic and resonance integrals of the Hückel theory, χ_r^0 is the magnetic susceptibility of the ϕ_r^0 orbital in the **H** direction, and $\rho_{r,s}$ is the electronic radius vector of the r, sth atom. The Coulombic integrals are taken to be homogeneous ($\alpha_r^0 = \alpha^0$, $\forall r$) and for a uniform magnetic field where the vector potential can be written as $\mathbf{A_r} = \mathbf{A} = (0, Hx, 0)$, the resonance integrals become

$$\beta_{rs} = \beta_{rs}^0 \exp[(ie/\hbar c)\eta_{rs}H], \tag{C.5}$$

where η_{rs} is the surface of the trapezoid defined by the $r - s$, bond and its projection on the x-axis is shown in Fig. 6-4. η_{rs} is related to the graphene hexagon area η=5.24 $\mathring{A}^2$ by

$$\eta_{rs} = \frac{1}{2}(n_0 + p)\eta \tag{C.6}$$

where p is the unit cell row index as shown in Fig. 6-4 and defined below, while n_0 is a constant depending on the position of the x-axis.

Now consider a M x P supercell made up of M columns and P rows of a graphene unit cell containing two atoms a and b. Application of cyclic Born-von Karman boundary conditions allows us to write the expansion coefficients of Eq. C.2 in terms of the mth column and the pth row, as

$$C_{m,p}^a = a_p \exp[2imu + ij(p-1)\pi/M], \tag{C.7}$$

$$C_{m,p}^b = b_p \exp[2imu + ijp\pi/M] \tag{C.8}$$

where $u = \pi j/M$ for $0 < j(\text{integer}) \leq M$ and the normalizable coefficients a_p, b_p are independent of m.

The secular equation (C-2) can be solved using Tchebycheff polynomials and appropriate boundary conditions[20] to yield the following orbital energies in the pres-

ence of a magnetic field:

$$E(\vartheta,u,S)_{\pm}=E^{0}(\vartheta_{0},u)_{\pm}\pm\beta^{0}\xi Q_{1}(\vartheta_{0},u)H+2S\mu_{B}H\pm\beta^{0}\xi^{2}Q_{2}(\vartheta_{0},u)H^{2}-\frac{1}{2}\chi_{0}H^{2} \tag{C.9}$$

where the discrete zero field energy levels (Eq. 6.3) are symmetric ($\pm$) about $E^{0}_{\pm}=\alpha^{0}$ and given by

$$E^{0}(\vartheta_{0},u)_{\pm}=\alpha^{0}\pm\beta^{0}(1+4\cos^{2}u+4\cos\vartheta_{0}\cos u)^{1/2} \tag{C.10}$$

for $\vartheta_{0}=k\pi/(P+1)$ and $0<k(\text{integer})\leq P$, and ϑ is defined below. In the above equations, $\xi=e\eta/2\hbar c$, $S=\frac{1}{2}$, and the London factors, Q_{1} and Q_{2} are given (for H perpendicular to the graphene planes) by

$$Q_{1}=-\frac{2\cos u\sin\vartheta_{0}}{(1+4\cos^{2}u+4\cos\vartheta\cos u)^{1/2}}\lambda_{1}, \tag{C.11}$$

$$\begin{aligned}Q_{2} &= -2\cos u(1+4\cos^{2}u+4\cos\vartheta_{0}\cos u)^{1/2}\times \\ &\left[\left(\frac{\cos\vartheta_{0}}{2}+\frac{\cos u\sin^{2}\vartheta_{0}}{1+4\cos^{2}u+4\cos\vartheta_{0}\cos u}\right)\lambda_{1}^{2}+\lambda_{2}\sin\vartheta_{0}\right]\end{aligned} \tag{C.12}$$

$$\lambda_{1}=-\frac{\tan u}{2\tan\vartheta_{0}} \tag{C.13}$$

$$\begin{aligned}(-4\sin^{3}\vartheta_{0})\lambda_{2} &= \frac{1}{\cos u}\left[\frac{10}{\sin^{2}\vartheta_{0}}-\frac{2}{3}(P^{2}+2P+15)+\frac{1}{3}(P^{2}+2P+3)\sin^{2}\vartheta_{0}\right] \\ &-\cos u\left[\frac{10}{\sin^{2}\vartheta_{0}}(4P^{2}+2P+15)+\frac{2}{3}(P^{2}+2P+3)\sin^{2}\vartheta_{0}\right] \\ &+\cos\vartheta_{0}\left[\frac{15}{2\sin^{2}\vartheta_{0}}-\frac{1}{2}(P^{2}+2P+1)-\cos^{2}\left(\frac{10}{\sin^{2}\vartheta_{0}}\frac{2}{3}(P^{2}+2P+3)\right)\right] \\ &+\frac{\cos\vartheta_{0}}{\cos^{2}u}\left[\frac{5}{2\sin^{2}\vartheta_{0}}-\frac{1}{6}(P^{2}+2P+3)(1+\sin^{2}\vartheta_{0})\right]\end{aligned} \tag{C.14}$$

where ϑ is a function of magnetic field,

$$\vartheta=\vartheta_{0}+\lambda_{1}\omega+\lambda_{2}\omega^{2} \tag{C.15}$$

and $\omega = (e/2\hbar c)\eta H$.

The above expression for the orbital energies in the presence of a magnetic field can then be used to evaluate the free energy F in the usual way and thus derive the magnetization, $\langle \mathbf{M} \rangle = -\partial F/\partial \mathbf{H}$, which can be written as

$$\langle \mathbf{M} \rangle = [\chi_s^C + \chi_s^P + \chi_I^L + \chi_{II}^L + M(2P+1)\chi_0]\mathbf{H}. \tag{C.16}$$

The Curie paramagnetic contribution χ_s^C is drastically over-counted in this theory due to the M localized orbitals located in the $p = 0$ row and χ_s^C is not considered here further. The Pauli paramagnetic component,

$$\chi_s^P = \frac{NS^2\mu_B^2}{12\mathrm{M}(2\mathrm{P}+1)k_BT} \sum_{\vartheta,\, u} [f(E_+) + f(E_-)]\,, \tag{C.17}$$

is quite small ($\leq 10^{-9}$ g^{-1} for P<90) because of the finite energy gap and symmetry between bonding and antibonding levels leading to extremely small antibonding state electron occupation (or bonding state hole occupation) that is responsible for Pauli paramagnetism. The remaining terms in Eq. C.16 are the London diamagnetic terms which lead to the diamagnetism of pregraphitic carbons. For H parallel to the graphene plane, the magnetic susceptibility is very close to the core diamagnetism, while for H perpendicular to the graphene planes, the London diamagnetism is given by

$$\chi_I^L = \frac{N(\beta^0)^2\xi^2}{12\mathrm{M}(2\mathrm{P}+1)} \sum_{\vartheta,\, u} Q_1^2(\vartheta, u)\,[f(E_+) + f(E_-)]\,, \tag{C.18}$$

$$\chi_{II}^L = \frac{-N\beta^0\xi^2}{6\mathrm{M}(2\mathrm{P}+1)} \sum_{\vartheta,\, u} Q_2(\vartheta, u)\,[\bar{n}(E_+) + \bar{n}(E_-)] \tag{C.19}$$

where $\bar{n}(E_\pm)$ is the Fermi occupation number and $f(E) = \partial\bar{n}(E)/\partial E$. By averaging over all orientations of graphene layers, the final form of the susceptibility becomes

$$\chi_{dia}(T) = \frac{1}{3}\chi_\perp + \chi_\parallel = \frac{1}{3}(\chi_I^L + \chi_{II}^L) + \chi_\parallel \tag{C.20}$$

where $\chi_\parallel = -0.3 \times 10^6 g^{-1}$.

Bibliography

[1] L.R. Dalton A.F. Garito, A.K.-Y. Jen and C. Lee, editors. *Mater. Res. Soc. Proc.*, number 328, Pittsburgh, PA, December 1994. Academic Press.

[2] B. L. Altshuler, A. G. Aronov, and D. E. Khmelnitsky. *J. Phys. C: Solid State Phys.*, 15:7367, 1982.

[3] B. I. Ambegaokar, B. I. Halperin, and J. S. Langer. *Phys. Rev.*, 34:2612, 1971.

[4] C. Ambrosch-Draxl, J. A. Majewski, P. Vogl, and G. Leising. *Phys. Rev. B*, 51:9668, 1995.

[5] P. W. Anderson. *Phys. Rev.*, 102:1008, 1958.

[6] P. W. Anderson and P. R. Weiss. *Rev. Mod. Phys.*, 25:269, 1953.

[7] F.S. Baker, A.R. Osborn, and J. Williams. *Nature*, 239:96, 1972.

[8] F.S. Baker, A.R. Osborn, and J. Williams. *J. Phys. D*, 7:2105, 1974.

[9] A. V. Baranov, A. N. Bekhterev, Ya. S. Bobovich, and V. I. Petrov. *Opt. Spect. (USSR)*, 62:612, 1987.

[10] J. L. Baudour, H. Cailleau, and W. B. Yelon. *Acta Crystallogr. Sec. B*, 33:1773, 1977.

[11] V. Bayot, L. Piraux, J.P. Michenaud, and J.P. Issi. *Phys. Rev. B*, 40:3514, 1989.

[12] G. Bergmann. *Phys. Rev. B*, 28:515, 1983.

[13] G. Bergmann. *Physics Reports*, 107:1, 1984.

[14] J. L. Bredas, R. R. Chance, and R. Silbey. *Phys. Rev. B*, 26:5843, 1982.

[15] J. L. Bredas, B. Themans, J. G. Fripiat, J. M. Andre, and R. R. Chance. *Phys. Rev. B*, 29:6761, 1984.

[16] R. Car and M. Parrinello. *Phys. Rev. Lett.*, 55:2471, 1985.

[17] M. Cardona. *Light Scattering in Solids.* Springer-Verlag, 1975.

[18] M. Cardona and G. Güntherodt. *Light Scattering in Solids II.* Springer-Verlag, 1982.

[19] G. Cedar, M. K. Aydinol, and A. F. Kohan. *Science*, 8:161, 1997.

[20] J. P. Chausse and J. Hoarau. *J. Chim. Phys.*, 66:1062, 1969.

[21] J. M. Chen and C. S. Wang. *Sol. St. Comm.*, 14:857, 1974.

[22] W. G. Clark and L. C. Tippie. *Phys. Rev. B*, 20:2914, 1979.

[23] R. Coehoorn, C. Hass, and R. A. de Groot. *Phys. Rev. B*, 35:6203, 1987.

[24] M. L. Cohen and V. Heine. *Solid State Physics*, volume 24, page 37. Academic, New York, 1970.

[25] N. B. Colthup, L. H. Daly, and S. E. Wiberley. *Introduction to Infrared and Raman Spectroscopy*, chapter 8. Academic Press, 1990.

[26] J. R. Dahn, R. Fong, and M. J. Spoon. *Phys. Rev. B*, 42:6424, 1990.

[27] J. R. Dahn, J. N. Reimers, T. Tiedje, Y. Gao, A. K. Sleigh, W. R. McKinnon, and S. Cramm. *Phys. Rev. Lett.*, 68:835, 1992.

[28] J. R. Dahn, A. K. Sleigh, H. Shi, B. M. Way, W. J. Weycanz, J. N. Reimers, Q. Zhong, and U. von Sacken. *New Materials and Perspectives.* North Holland, 1993.

[29] J. R. Dahn, T. Zheng, Y. Liu, and J. S. Xue. *Science*, 270:590, 1995.

[30] J.R. Dahn. *Phys. Rev. B*, 44:9170, 1991.

[31] W. A. de Heer, A. Châtelain, and D. Ugarte. Carbon nanotube field-emission electron source. *Science*, 270:1179, 1995. see also ibid page 1119.

[32] Y. Delugeard, J. Desuche, and J. L. Baudour. *Acta Crystallogr. Sec. B*, 32:702, 1976.

[33] S. L. di Vittorio, M. S. Dresselhaus, M. Endo, and T. Nakajima. *Phys. Rev. B*, 43:1313, 1991.

[34] P. A. M. Dirac. *Proc. Roy. Soc. (London)*, 114:710, 1927.

[35] G. L. Doll, P. C. Eklund, and J. E. Fischer. *Phys. Rev. B*, 36:4940, 1987.

[36] M. S. Dresselhaus, G. Dresselhaus, K. Sugihara, I. L. Spain, and H. A. Goldberg. *Graphite Fibers and Filaments*, volume 5 of *Springer Series in Materials Science*. Springer-Verlag, Berlin, 1988.

[37] M. S. Dresselhaus and M. Endo. *Graphite Intercalation Compounds II*. Springer-Verlag, 1992.

[38] P.A. Thrower (ed.). *Physics and Chemistry of Carbon*. Marcel-Dekkar, 1965-1997.

[39] A. L. Efros and B. I. Shklovskii. *J. Phys. C*, 8:L49, 1975.

[40] M. Endo. *Unpublished*.

[41] M. Endo, C. Kim, T. Karaki, Y. Nishimura, M. J. Matthews, S. D. M. Brown, and M. S. Dresselhaus. *submitted to J. Mat. Res.*

[42] M. Endo, J. Nakamura, A. Emori, and M. Inagaki. Lithium secondary battery using carbon fibers as a negative electrode. In *Extended Abstracts, 21st Biennial Conf. Carbon, Buffalo, N.Y.*, page 608, 1993.

[43] M. Endo, J. Nakamura, H. Touhara, and S. Morimoto. *T. IEEE Japan*, 108A:81, 1988. (in Japanese).

[44] M. Endo, Y. Nishimura, T. Takahashi, K. Takeuchi, and M. S. Dresselhaus. *J. Phys. Chem. Solids*, 57:725, 1996.

[45] J. F. Fauvarque, A. Digua, M. A. Petit, and J. Savard. *Makromol. Chem.*, 186:2415, 1985.

[46] J. L. Feldman. *Phys. Rev. B*, 25:7132, 1982.

[47] Y. Feldman, G. L. Frey, M. Homyonfer, V. Lyakhovitskaya, L. Margulis, H. Cohen, G. Hodes, J. L. Hutchison, and R. Tenne. *J. Am. Chem. Soc.*, 118:5362, 1996.

[48] Y. Feldman, E. Wasserman, D. J. Srolovitz, and R. Tenne. *Science*, 267:222, 1995.

[49] R. W. Fessenden and R. H. Schuler. *J. Chem. Phys.*, 39:2147, 1963.

[50] R. P. Feynman. *Phys. Rev.*, 56:340, 1939.

[51] D.B. Fischbach and D.W. Gilbert. *J. Mat. Sci.*, 14:1586, 1979.

[52] J. E. Fischer. *Chemical Physics of Intercalation.* Plenum Press, 1987.

[53] G. L. Frey, S. Ilani, M. Homyonfer, Y. Feldman, and R. Tenne. *PRB, In press.*

[54] G. L. Frey, R. Tenne, M. J. Matthews, M. S. Dresselhaus, and G. Dresselhaus. *Submitted to J. Mater. Res.*

[55] G. Froyer, F. Maurice, P. Bernier, and P. McAndrew. *Polymer*, 23:1103, 1982.

[56] A. W. P. Fung, M. S. Dresselhaus, and M. Endo. *Phys. Rev. B*, 48:20, 1993.

[57] A. W. P. Fung, Z. H. Wang, K. Lu, M. S. Dresselhaus, and R. W. Pekala. *J. Mater. Res.*, 8:1875, 1993.

[58] Alex Weng Pui Fung. *Localization Transport in Granular and Nanoporous Carbon Systems.* PhD thesis, M.I.T., 1994.

[59] Y. Furukawa, H. Ohtsuka, and M. Tasumi. *Synth. Met.*, 55-57:516, 1993.

[60] N. Ganguli and K. S. Krishnan. *Proc. Roy. Soc. (London)*, A117:168, 1941.

[61] P. M. Grant and I. P. Batra. *Synth. Met.*, 1:193, 1980.

[62] R. R. Haering and P. R. Wallace. *J. Phys. Chem. Solids*, 3:253, 1957.

[63] T. Hamada, M. Furuyama, T. Tomioka, and M. Endo. Preferred orientation of high performance carbon fibers. *J. Mater. Res.*, 7:2612–2620, 1992.

[64] T. Hamada, M. Furuyama, T. Tomioka, and M. Endo. Preferred orientation of pitch precursor fibers and carbon fibers prepared from isotropic pitch. *J. Mater. Res.*, 7:1178–1188, 1992. ibid., 2612-2620.

[65] A. Heim, G. Leising, and H. Kahlert. *J. of Luminescence*, 31–32:573, 1984.

[66] R. J. Hemley, J. I. Dawson, and V. Vaida. *J. Chem. Phys.*, 78:2915, 1983.

[67] A. Henderson and G. F. Imbusch. In Oxford Science Publications, editor, *Optical Spectroscopy of Inorganic Solids*, 1989.

[68] M. Hershfinkel, L. A. Gheber, V. Voltera, J. L. Hutchison, L. Margulis, and R. Tenne. *J. Am. Chem. Soc.*, 116:1914, 1994.

[69] J. Hoarau and G. Volpilhac. *Phys. Rev. B*, 14:4045, 1976.

[70] P. Hohenberg and W. Kohn. *Phys. Rev.*, 136:864B, 1964.

[71] M. Homyonfer, B. Alperson, Y. Rosenberg, L. Sapir, H. Cohen, G. Hodes, and R. Tenne. *J. Am. Chem. Soc.*, 119:2693, 1997.

[72] B. Huang, Y. Huang, Z. Wang, L. Chen, R. Xue, and F. Wang. *J. Power Sources*, 58:231, 1996.

[73] S. Iijima. *Nature (London)*, 354:56, 1991.

[74] Electrons in Disordered Structures. *Adv. Phys.*, 16:49, 1967.

[75] A. Kasuya, M. Sugano, T. Maeda, Y. Saito, K. Tohji, H. Takahashi, Y. Sasaki, M. Fukushima, Y. Nishina, and C. Horie. *Phys. Rev. B*, 57:4999, 1998.

[76] A. Kawagughi and J. Petermann. *Mol. Cryst. Liq. Cryst.*, 133:189, 1986.

[77] T. Keil. *Phys. Rev.*, 140:A601, 1965.

[78] B. T. Kelly. *Physics of Graphite*, chapter 4. Applied Science Publishers, 1981.

[79] L. D. Kispert, J. Joseph, and G. G. Miller R. H. Baughman. *J. Chem. Phys.*, 81:2119, 1984.

[80] D.S. Knight and W.B. White. *J. Mater. Res.*, 4:385, 1989.

[81] W. Kohn and L. J. Sham. *Phys. Rev.*, 140:1133A, 1965.

[82] S. Komarneni, editor. *Mater. Res. Soc. Proc.*, number 328, Pittsburgh, PA, December 1994. Academic Press.

[83] J. Korringa. *Physica*, 16:601, 1950.

[84] A. S. Kotosonov. *Sov. Phys. Solid State*, 33:1477, 1992.

[85] P. Kovacic and A. Kyriakis. *J. Am. Chem. Soc.*, 85:454, 1963.

[86] H. A. Kramers and W. Heisenberg. *Z. Phys.*, 31:681, 1925.

[87] S. Krichene, J.P. Buisson, and S. Lefrant. *Synth. Met.*, 17:589, 1987.

[88] S. Krichene, S. Lefrant, G. Froyer, F. Maurice, and Y. Pelous. *J. Phys. (Paris) Colloq.*, 44:C3–733, 1983.

[89] K. S. Krishnan. *Nature*, 133:174, 1934.

[90] H. W. Kroto, J. R. Heath, S. C. O'Brien, R. F. Curl, and R. E. Smalley. *Nature*, 318:6042, 1985.

[91] L. L. Krushinskii and P. P. Shorygin. *Opt. i Spektroskopiya*, 11:24, 1961.

[92] L. L. Krushinskii and P. P. Shorygin. *Opt. i Spektroskopiya*, 11:151, 1961.

[93] P. J. Krusic and T. A. Rettig. *J. Am. Chem. Soc.*, 92:722, 1970.

[94] P. Kuivalainen, H. Stubb, H. Isotalo, P. Yli-Lahti, and C. Holmstrom. *Phys. Rev. B*, 31:7900, 1985.

[95] J. S. Langer and T. Neal. *Phys. Rev. Lett.*, 16:984, 1966.

[96] P. A. Lee and T. V. Ramakrishnan. *Rev. Mod. Phy.*, 57:287, 1985.

[97] G. Leising, O. Leitner, F. Aldrian, and H. Kalhert. *Synthetic Metals*, 17:635, 1987.

[98] N. R. Lerner. *J. Poly. Sci.*, 12:2477, 1974.

[99] P. Lespade, R. Al-Jishi, and M. S. Dresselhaus. *Carbon*, 20:427, 1982.

[100] I. C. Lewis. *Carbon*, 20:519, 1982.

[101] I. C. Lewis and L. S. Singer. *Carbon*, 5:373, 1967.

[102] Y. Liu, S. Xue, T. Zheng, and J. R. Dahn. *Carbon*, 34:193, 1996.

[103] F. London. *J. Phys. Radium*, 8:397, 1937.

[104] C. E. Lowell. *J. Am. Ceramic Soc.*, 50:142, 1967.

[105] A. Mabuchi, K. Tokumitsu, H. Fujimoto, and T. Kasuh. *J. Electrochem. Soc.*, 142:1041, 1995.

[106] O. Madelung. *Introduction to Solid State Theory*, chapter 1. Springer-Verlag, 1978.

[107] G. D. Mahan. *Solid State Physics*, volume 29, page 76. Academic, New York, 1974.

[108] B. Marcus, L. Fayette, M. Mermouz, L. Abello, and G. Lucazeau. *J. Appl. Phys.*, 76:3463, 1994.

[109] A. Marucci, S. D. M. Brown, M. A. Pimenta, M. J. Matthews, M. S. Dresselhaus, and M. Endo. *To be submitted.*

[110] K. Matsubara, K. Kawamura, and T. Tsuzuku. *Jpn. J. Appl. Phys.*, 25:1016, 1986.

[111] Y. Matsumura, S. Wang, T. Kasuh, and T. Maeda. *Synth. Met.*, 71:1755, 1995.

[112] M. J. Matthews and T. A. Arias. *To be published.*

[113] M. J. Matthews, X. X. Bi, M. S. Dresselhaus, M. Endo, and T. Takahashi. *Appl. Phys. Lett.*, 68:1078, 1996.

[114] M. J. Matthews, M. S. Dresselhaus, G. Dresselhaus, M. Endo, Y. Nishimura, and T. Hiraoka. *Appl. Phys. Lett.*, 69:430, 1996.

[115] M. J. Matthews, M. S. Dresselhaus, M. Endo, Y. Sasabe, T. Takahashi, and K. Takeuchi. *J. Mat. Res.*, 11:3099, 1996.

[116] M. J. Matthews, M. S. Dresselhaus, N. Kobayashi, T. Enoki, M. Endo, and T. Takahashi. *Appl. Phys. Lett.*, 69:2042, 1996.

[117] J. W. McClure. *Phys. Rev.*, 104:666, 1956.

[118] J. W. McClure. Theory of 3D diamagnetism in graphite. *Phys. Rev.*, 119:606, 1960.

[119] J. W. McClure and B. B. Hickman. *Carbon*, 20:373, 1982.

[120] J. W. McClure and W. J. Spry. *Phys. Rev.*, 165:809, 1968.

[121] T. P. Mernagh, R. P. Cooney, and R. A. Johnson. *Carbon*, 22:39–42, 1984.

[122] F. Mohammad, P. D. Calvert, and N. C. Billingham. *J. Phys. D*, 29:195, 1996.

[123] N. F. Mott. *Adv. Phys.*, 16:49, 1969.

[124] N. F. Mott. *Electronic Processes in Non-crystalline Materials.* Oxford University Press, 1979.

[125] S. Mrozoski. *Carbon*, 3:305, 1965.

[126] S. Mrozowski. *Phys. Rev.*, 77:838, 1950.

[127] S. Mrozowski. *J. Low Temp. Phys.*, 35:231, 1979.

[128] S. Mrozowski. Specific heat anomalies and spin-spin interactions. *J. Low Temp. Phys.*, 35:231, 1979.

[129] S. Mrozowski. *Carbon*, 20:303, 1982.

[130] M. Nagashima, I. Tamura, Y. Ikezawa, and T. Takamura. Pronounced improvement of cathode characteristics of polypyrrole for lithium batteries by the electrodeposition on active carbon fibers. In *Electrochemical Society, Honolulu, HI*, page 99, 1993.

[131] M. Nakadaira, R. Saito, T. Kimura, G. Dresselhaus, and M. S. Dresselhaus. *J. Mater. Res.*, 12:1367, 1997.

[132] M. Nakamizo, R. Kammereck, and P. L. Walker Jr. *Carbon*, 12:259, 1974.

[133] Needed et al. 1992.

[134] R. J. Nemanich and S. A. Solin. *Phys. Rev. B*, 20:392, 1979.

[135] A. Oberlin. In P. A. Thrower, editor, *Chemistry and Physics of Carbon*, volume 22, pages 1–144. Marcel Dekker, NY, 1989. Vol. 22.

[136] A. Paucault and A. Marchand. *Annales de Chimie*, 2:469, 1957.

[137] D. K. Paul and S. S. Mitra. *Phys. Rev. Lett.*, 31:1000, 1973.

[138] M. C. Payne, M. P. Teter, D. C. Allan, T. A. Arias, and J. D. Joannopoulos. *Rev. Mod. Phys.*, 64:1045, 1992.

[139] M. Peo, S. Roth, and J. Hocker. *Chemica Scripta*, 17:133, 1981.

[140] D. G. Pettifor. *Bonding and Structure of Molecules and Solids*, chapter 3. Clarendon, 1995.

[141] J. C. Phillips. *Phys. Rev.*, 112:685, 1958.

[142] L. Pietronero and E. Tosatti. *Physics of Intercalation Compounds*, chapter 4. Springer-Verlag, 1981.

[143] M. A. Pimenta. *private communication.*

[144] G. Placzek. *Handbuch der Radiologie.* Akademische Verlagsgeselschaft, Leipzig, 1934.

[145] L. R. Radovic, editor. *Extended Abstracts of the 23rd Biennial Conference on Carbon.*

[146] A. P. Ramirez, R. C. Haddon, O. Zhou, R. M. Fleming, J. Zhang, S. M. McClure, and R. E. Smalley. Magnetic susceptibility of molecular carbon: nanotubes and fullerite. *Science*, 265:84, 1994.

[147] M. Ramsteiner and J. Wagner. *Appl. Phys. Lett.*, 51:1355, 1987.

[148] Gillian A. M. Reynolds. *Electronic Transport And Photoconductive Properties Of Resorcinal Formaldehyde Carbon Aerogels And Other Disordered Carbon Systems.* PhD thesis, M.I.T., 1994.

[149] H. M. Rietveld, E. N. Maslen, and C. J. Clews. *Acta Crystallogr. Sec. B*, 26:693, 1970.

[150] J. Robertson. *Adv. Phys.*, 35:317, 1986.

[151] E. Rzepka, C. Q. Jin, and S. Lefrant. *Synthetic Metals*, 29:E23, 1989.

[152] R. Saito, G. Dresselhaus, and M. S. Dresselhaus. *Physical Properties of Carbon Nanotubes.* Imperial College Press, London, 1998. in press.

[153] Alvin J. Salkind. A historical overview of battery innovation and technology. In *Proc. of the Syposium on the History of Battery Technology*, 1987.

[154] S. Jimenez Sandoval, D. Yang, R. F. Frindt, and J. C. Irwin. *Phys. Rev. B*, 44:3955, 1991.

[155] S. Sasaki. *J. Polymer Sci. B*, 30:293, 1992.

[156] K. Sato, M. Noguchi, A. Demachi, N. Oki, and M. Endo. *Science*, 264:556, 1994.

[157] T. Sekine, M. Izumi, T. Nakashizu, Uchinokura, and E. Matsuura. *J. Phys. Soc. Japan*, 49:1069, 1980.

[158] L. W. Shacklette, H. Eckhardt, R. R. Chance, G. G. Miller, D. M Ivory, and R. H. Baughman. *J. Chem Phys.*, 73:4098, 1980.

[159] M. P. Sharma, L. G. Johnson, and J. W. McClure. *Phys. Rev. 9*, 9:2467, 1974.

[160] T. E. Sharp and H. M Rosenstock. *J. Chem. Phys.*, 41:3453, 1964.

[161] P. Sheng and J. Klafter. *Phys. Rev. B*, 27:2583, 1983.

[162] P. Sheng, E. K. Sichel, and J. I. Gittleman. *Phys. Rev. Lett.*, 40:1197, 1978.

[163] B. I. Shklovskii and A. L. Efros. In *Electronic Properties of Doped Semiconductors*. Springer-Verlag, Berlin, 1984. Springer series in solid state sciences; vol 45.

[164] L. S. Singer and J. Kommandeur. *J. Chem. Phys.*, 34:133, 1961.

[165] K. Sinha and J. Menéndez. *Phys. Rev. B*, 41:10845, 1990.

[166] C. P. Slichter. *Principles of Magnetic Resonance*, chapter 5. Harper & Row, 1963.

[167] Z. Soos. *J. Chem. Phys.*, 44:1729, 1966.

[168] J. Soto, V. Hernandez, and J. T. Lopez Navarrete. *Synth. Met.*, 51:229, 1992.

[169] C. Sourisseau, F. Cruege, and M. Fouassier. *J. Chem. Phys.*, 150:281, 1991.

[170] I. L. Spain. *The Electronic Properties of Graphite*, volume 8 of *Chamistry and Physics of Carbon*. Marcel-Dekkar, New York, 1973.

[171] I. L. Spain. *The Electronic Transport Properties of Graphite, Carbons and Related Materials*, volume 16 of *Chamistry and Physics of Carbon.* Marcel-Dekkar, New York, 1981.

[172] T. G. Spiro. *Biological Applications of Raman Spectroscopy.* John Wiley & Sons, 1987.

[173] A. M. Stacy and D. T. Hodul. *J. Phys. Chem. Solids*, 46:405, 1985.

[174] O. Stephan, P. M. Ajayan, C. Colliex, Ph. Redlich, J. M. Lambert, P. Bernier, and P. Lefin. Doping graphitic and carbon nanotube structures with boron and nitrogen. *Science*, 266:1683, 1994.

[175] E.A. Taft and H. R. Philipp. *Phys. Rev.*, 138:A197, 1965.

[176] K. Tanaka, M. Kobashi, H. Sanekata, T. Yamabe, J. Yamauchi, and S. Yata. *Phys. Rev. B*, 44:1101, 1991.

[177] K. Tanaka, T. Koike, T. Yamabe, J. Yamauchi, Y. Deguchi, and S. Yata. *Phys. Rev. B*, 35:8368, 1987.

[178] M. P. Teter, M. C. Payne, and D. C. Allan. *Phys. Rev. B*, 40:12255, 1989.

[179] F. Tuinstra and J. L. Koenig. *J. Chem. Phys.*, 53:1126, 1970.

[180] J. L. Verble and T. J. Wieting. *Phys. Rev. Lett.*, 25:362, 1970.

[181] J. Wagner, M. Ramsteiner, Ch. Wild, and P. Koidl. *Phys. Rev. B*, 40:1817, 1989.

[182] N. Wakabayashi, H. G. Smith, and R. M. Nicklow. *Phys. Rev. B*, 12:659, 1975.

[183] P. R. Wallace. *Phys. Rev.*, 71:622, 1947.

[184] Y. Wang, D. C. Alsmeyer, and R. L. McCreery. *Chem. Mater.*, 2:557, 1990.

[185] A. Warshel and P. Dauber. *J. Chem. Phys.*, 66:5477, 1977.

[186] A. Warshel and M. Karplus. *Chem. Phys. Lett.*, 17:7, 1972.

[187] T. J. Wieting and J. L. Verble. *Phys. Rev. B*, 3:4286, 1971.

[188] R. W. G. Wyckoff. *Crystal Structures.* Interscience: New York, 1964. volume 1.

[189] Y. Yamada, T. Furuta, M. Shiraishi, M.-A. Sato, and K. Kaeriyama. *J. Mater. Sci.*, 24:3113, 1989.

[190] Y. Yamada, T. Furuta, M. Shiraishi, M.-A. Sato, and K. Kaeriyama. *J. Mater. Sci.*, 24:3113, 1989.

[191] T. Yamamoto, Y. Hayashi, and A. Yamamoto. *Bull. Chem. Soc. Japan*, 51:2091, 1978.

[192] M. T. Yin and M. L. Cohen. *Phys. Rev. B*, 26:5668, 1982.

[193] K. Yoshizawa, K. Okahara, T. Sato, K. Tanaka, and T. Yamabe. *Carbon*, 32:1517, 1994.

[194] G. Zannoni and G. Zerbi. *J. Chem. Phys.*, 82:31, 1985.

[195] T. Zheng, J. N. Reimers, and J. R. Dahn. *Phys. Rev. B*, 51:734, 1995.